MOEMS based on Magnetic/Photonic Sensitive Stimuli Polymers

Sandra de Pedro i Jordán

Doctorat en Física

Bellaterra 2014

Universitat Autònoma de Barcelona
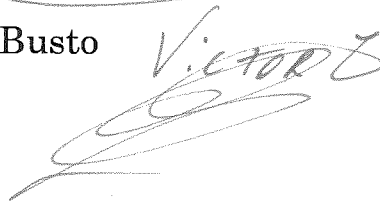
Departament de Física Òptica

Directors:

Dr. Andreu Llobera Adán

Dr. Víctor Javier Cadarso Busto

Tutor:

Dr. Jordi Mompart Pepina

3. Compendium of articles

In this section the articles in this thesis has been based are attached. Moreover, it has been divided into two subsections: i) the accepted and published articles in journals and ii) the articles under review.

3.1. Accepted and published articles in journals

1. S. de Pedro, A. Voigt, V. J. Cadarso, J. Vila-Planas, J. Brugger, S. Büttgenbach, A. Llobera, G. Gruetzner, "UV-patternable polymers with selective spectral response", *Microelectronic Engineering,* vol. 98, pp. 234-237, Oct. 2012, IF: 1.295(2011), Subject area: Material Science: Electronic, Optical and Magnetic Materials, Rank: 0.572.

2. S. de Pedro, V. J. Cadarso, X. Muñoz-Berbel, J. A. Plaza, J. Sort, J. Brugger, A. Llobera, "PDMS-based, magnetically actuated variable optical attenuators obtained by soft lithography and inkjet printing technologies", *Sensors and Actuators A: Physical*, vol. 215, pp. 30-35, Jan. 2014, IF: 2.116 (2014), Subject Area: Material Science: Electronic, Optical and Magnetic Material, Rank: 0.883.

3. S. de Pedro, V. J. Cadarso, T. Ackerman, X. Muñoz-Berbel, J. A. Plaza, J. Brugger, S. Büttgenbach, A. Llobera, "Polymeric variable optical attenuators based on magnetic sensitive stimuli materials", *Journal of Micromechanics and Microengineering*, vol. 24, pp. 14, Sept. 2014, IF: 1.597 (2014), Subject area: Material Science: Electronic, Optical and Magnetic Material, Rank: 0.726.

3. Compendium of articles

3.2. Under review articles

Moreover, I have been working on several articles which are in different status of evolution. Those articles have been also included in this thesis because of its relevance to thesis topic.

Additionally, there is a fourth paper which is in the latest revision by the authors / co-authors to submit it to *Small* journal:

1. <u>S. de Pedro</u>, X. Muñoz-Berbel, R . Rodríguez-Rodríguez, J. Sort, J. A. Plaza, E. Mendoza, J. Brugger, A. Llobera and V. J. Cadarso, "Preparation and Characterization of Patternable Magnetic Stimulus Sensitive Elastomers Obtained from Mixtures of PDMS and Ferrofluid".

Finally, there is a fifth article that is coming to an end of writing to submit to *Journal of Micromechanics and Microengineering*:

2. <u>S. de Pedro</u>, T. Ackermann., J. A. Plaza., L. Thomas, E. Alvarez, A.Vierheller, S. Büttgenbach, V. J. Cadarso and A. Llobera, "All-photoinc SU-8 variable optical attenuator".

Contents lists available at ScienceDirect

Microelectronic Engineering

journal homepage: www.elsevier.com/locate/mee

Corrigendum

Corrigendum to: "UV-patternable polymers with selective spectral response" [Microelectron. Eng. 98 (2012) 234–237]

Sandra de Pedro [a,*], Anja Voigt [b], Victor J. Cadarso [c], Jordi Vila-Planas [a], Juergen Brugger [c], Stephanus Büttgenbach [d], Andreu Llobera [a,d], Gabi Gruetzner [b]

[a] Institut de Microelectrònica de Barcelona, IMB-CNM (CSIC), Esfera UAB, Campus UAB, 08193 Bellaterra, Spain
[b] Microresist Technology GmbH, Berlin D-12555, Germany
[c] Microsystems Laboratory, EPFL, Lausanne CH-1015, Switzerland
[d] Institut für Mikrotechnik, Technische Universität Braunschweig, D-38124 Braunschweig, Germany

The correct affiliations for the authors have been shown above.
Authors apologize for the inconvenience caused to the readers.

UV-patternable polymers with selective spectral response

Sandra de Pedro [a,*], Anja Voigt [b], Victor J. Cadarso [c], Jordi Vila-Planas [a], Juergen Brugger [a,b,c,d], Stephanus Büttgenbach [d], Andreu Llobera [a,d], Gabi Gruetzner [b]

[a] CNM-IMB-CSIC Barcelona, E-08193 Barcelona, Spain
[b] Microresist Technology GmbH, Berlin D-12555, Germany
[c] Microsystems Laboratory, EPFL, Lausanne CH-1015, Switzerland
[d] Institut für Mikrotechnik, D-38124 Braunschweig, Germany

ARTICLE INFO

ABSTRACT

We present the characterization of dyed doped/modified Epocore resist (Microresist Technology, Germany) with three commercially-available dyes (Proquimac Color, Spain). After being doped with lilac, red and yellow dyes in a 1:2500 ratio (dye:Epocore, w:w), an exposure dose test was performed. The obtaining lithographic performance is similar to the non-doped Epocore. Hence, the inclusion of the dye does not affect either the absorbance in the UV range or the structurability of the polymer. In a second step, this polymer is used to define integrated absorbance filters, by using standard soft lithography techniques. Concretely, four different filter lengths have been fabricated. The highest absorbance value was found with filter length of 500 μm, with stop-bands at concrete regions of the visible spectra: −5.17 dB@592.0 nm for lilac dye, −3.30 dB@531.0 nm for red dye, and −4.40 dB@496.8 nm for yellow dye. Additionally, a non-zero passband penalty (−0.75 dB) in the red filter is observed. Moreover, bleaching of the filters was also tested by a continuous exposure to UV light. The doped polymer retains 96% of its filtering properties after a dose close to 40.000 J/cm^2.

1. Introduction

Polymeric materials or resists suitable to selectively absorb certain wavelengths are interesting for a myriad of applications, ranging from integrated absorbance filters in photonic lab on a chip [1,2] to sample identification [3].

The most commonly used integrated filters are interferometric filters [4]. These generally consist of a large number of alternated low refractive/high refractive index materials in a thin multilayered structure [5]. Their process fabrication has accuracy limitations as well as incidence angle dependence. These characteristics of the interferometric filters result in higher manufacturing costs. Alternatively, absorbance filters are based on the attenuation of the light for given range of wavelength due to the presence of an organic compound (chromophores) [6] or a bandgap material [7]. When the organic compounds work as absorbing material the spectral response depends both on the concentration/solubility dye into the matrix polymer and on the filter length, defined by the Beer–Lambert law. Comparing, the absorbance filters to interferometric filters, there is no dependence on the incidence angle and their fabrication tolerance is much higher. Hence, they can be easily implemented

and integrated. Previously presented integrated filters are mainly developed using thermocurable polymers, which lack of temporal stability. For instance, Hofmann et al. have used a lysochrome dye (Sudan) to dope poly(dimethylsiloxane) (PDMS), however diffusion of the dye molecules out the PDMS matrix was observed [8] and non-zero passband transmittance was obtained [9], resulting on a suboptimal performance of the filters.

In this paper we propose and demonstrate the fabrication of UV curable epoxy-based absorbance filters. Through standard soft-lithographic process a collection of testing structures are fabricated. The high ratio resolution 10:1 obtained is described in the following section. We design, fabricate and characterize a dye-doped Epocore filter. Its characterization consists on spectral response and a bleaching study. For the first case three filters with the same length (500 μm) but different color dye-doped (lilac, red and yellow) are studied. For the bleaching characterization a red-dye-doped Epocore filter has been used. A controlled exposure of the filter to UV light (wavelength of 365 nm) at different doses is carried out for determining the aging of the dye. The results are presented on the last section.
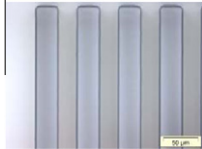
2. Material characterization

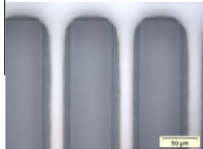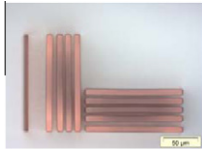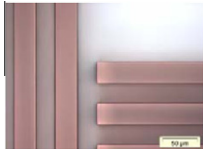In this work Epocore has been selected as base material for the development of integrated absorbance filters. Epocore (Microresist

* Corresponding author.
E-mail addresses: sandra.depedro@imb-cnm.csic.es (S. de Pedro), andreu .llobera@ imb-cnm.csic.es (A. Llobera).

Table 1

Images from the photolithographic process of the lilac-, red- and yellow-doped Epocore material on silicon. Four different doses (D_1: 500 mJ/cm2, D_2: 1000 mJ/cm2, D_3: 2000 mJ/cm2, D_4: 2500 mJ/cm2) were tested.

	D_1 = 500 mJ/cm2	D_2 = 1000 mJ/cm2	D_3 = 2000 mJ/cm2	D_4 = 2500 mJ/cm2
Lilac Epocore-modified-material	Resolution: 30 μm	Resolution: 30 μm	Resolution: 40 μm	Resolution: 50 μm
Red Epocore-modified material	Resolution: 7 μm	Resolution: 20 μm	Resolution: 30 μm	Resolution: 30 μm
Yellow Epocore-modified material	Resolution: 10 μm	Resolution: 20 μm	Resolution: 30 μm	Resolution: 40 μm

GmbH, Germany) [10] is a known polymer with outstanding structural properties, which allow obtaining ultra-thick geometries with vertical sidewalls, with low losses (<0.2 dB/cm, at λ = 850 nm) in the visible-NIR range [11]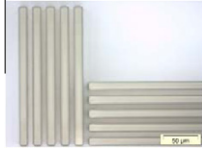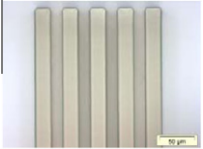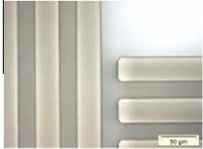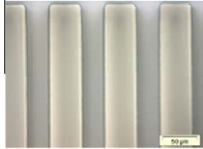. After exposure to UV irradiation, aspect ratios higher than 10:1 are obtained. In addition, non-doped Epocore shows very high transmittance values for wavelengths higher than 450 nm. Among the main applications [10] of this material we want to highlight the optical applications in micro system technology [12]. Hence it is clear that Epocore is an excellent candidate for the development of absorbance filters by doping it with colored dyes. Dye-doped Epocore is obtained by mixing 1 mg dye (lilac, red and yellow) per 25 g of Epocore (1:2500 ratio). The subsequent mixture is degassed to remove the air bubbles and it is poured on the wafer. Once the material is prepared it is possible to proceed with a standard UV process to structure it. In this work an exposure test has been performed using dye-doped Epocore 50 μm-thick layers. To achieve such thickness the mixture is spun at 1500 rpm for 60 s followed by a pre-bake (PB) (5 min at 50 °C, ramp up to 90 °C, bake 7 min at 90 °C). After that, the polymer is exposed to the UV light. Four different doses (D_1: 500 mJ/cm^2, D_2: 1000 mJ/cm^2, D_3: 2000 mJ/cm^2, D_4: 2500 mJ/cm^2) was tested with a post-exposure-bake (PEB) (5 min at 50 °C ramp up to 85 °C, bake 10 min at 85 °C and slowly cool down). Finally, the chemical development of the layers is carried out (180 s, PGMEA). The resulting structures of dyed-doped Epocore are shown in Table 1. It can be seen that the dye-doped Epocore structures are crack-free. Furthermore, the structurability of the polymer is retained with a reduction of the resolution as the dose increases. At the same time there is no sign of dye diffusion out from the defined structures. From the above results, the application of the dye-doped Epocore polymer as an integrated element into a system detection is considered. With this purpose the design, fabrication and characterization of the absorbance filters based on the dye-doped Epocore is carried out. The results are shown in the next sections.

3. Absorbance filters based on dye-doped Epocore

3.1. Design

The design for the optical testing structure is illustrated in Fig. 1. A microfluidic channel with four sections of different lengths
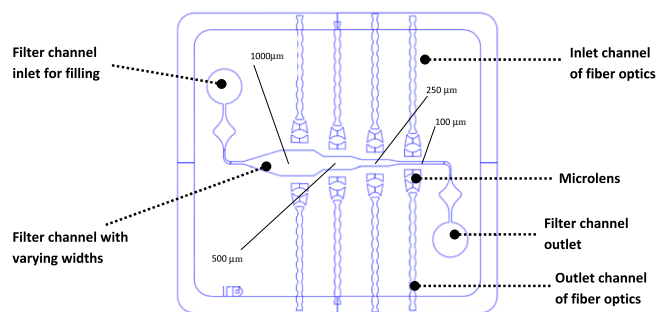
Fig. 1. Testing structure composed of a continuous filter channel with four sections of different lengths (100, 250, 500 and 1000 μm). The self-microchannels for positioning the in- and out-put optical fibers, the microlenses for focusing the outcoming light from the optical fiber, the filter channel with varying lengths, the in- and out-let filter channel for filling and collecting, respectively, the dye-doped Epocore are designed completing the structure of the filters.

(100 μm, 250 μm, 500 μm, 1000 μm) is included for the evaluation of the Beer–Lambert law. Near the 100 μm section there is an inlet. Through it the filter channel is filled with one of the dye-doped Epocore solutions. On the opposite side of the microfluidic channel there is an outlet channel for collecting the remaining Epocore. Four self-alignment microchannels are placed at each side of the filters in order to assure the accurate positioning of the in- and out-put optical fibers. Additionally, a microlens is placed at the end of the self-alignment microchannel [13]. The optical fibers are fixed in the focus of a microlens for correcting the expansion of the emerging beams.

3.2. Fabrication

The fabrication of the absorbance filters starts with the development of the SU-8 (MicroChem, Corp.,Newton, MA, USA) master [14] followed by a replication of it based on standard soft-lithography. A pre-polymer of PDMS is prepared by mixing the curing agent and the elastomer base in a 1:10 ratio (v: v) and degassing
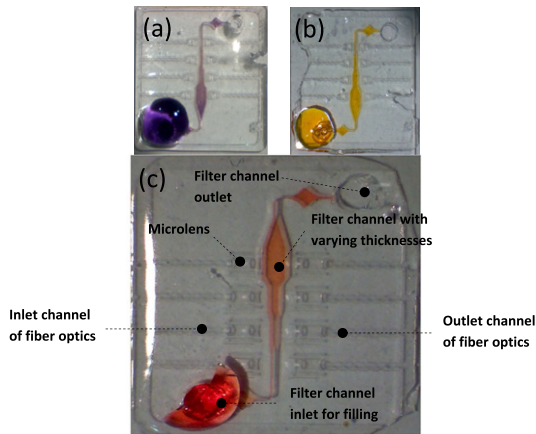
Fig. 2. Fabricated (a) lilac-, (b) yellow and (c) red-dye-doped Epocore filters. (c) The detail of the red filter: the four sections of different lengths (100, 250, 500 and 1000 µm), the self-microchannels for positioning of in- and out-put optical fibers, the microlenses for focusing the outcoming light from the optical fiber, the filter channel inlet for filling the filter channel and the filter channel outlet are labeled (For interpretation of the references to color in this figure legend, the reader is referred to the web version of this article).

Fig. 3. Spectral response for lilac-, red- and yellow-dye-doped Epocore. The non-modified Epocore is the reference measurement. The stopband for the three filters in a concrete region of the visible spectra: −5.17 dB@592.0, −3.30 dB@531.0, −4.40 dB@496.8 are plotted. Additionally, the non-zero passband for the red-filter with −0.75 dB is included in the results (For interpretation of the references to color in this figure legend, the reader is referred to the web version of this article).

in a vacuum chamber. After pouring the prepolymer over the maser, the PDMS fills all the structures by capillary. Then, it is cured for 20 min at 80 °C. Finally, the fabricated devices are peeled off from the master [15]. All the designed structures, filter channel, microlenses, self-alignment channels and the in- and outlet filter channel are well defined. On the next step, we used a bonding procedure based on a surface treatment in oxygen plasma. Both the PDMS device surface and the glass are exposed to oxygen plasma. After that, the two surfaces are fit together on an irreversibly bonded, follow by mechanically opening both fluidic inlet and outlet. So, when a drop of dye-doped Epocore is dispensed at the inlet filter channel by capillary forces, the structure is completely filled. Then, an exposure dose to UV light of 750 mJ/cm² is carried out over the dye-doped Epocore. Finally, with a PEB with a PEB (5 min at 50 °C ramp up to 85 °C, bake 10 min at 85 °C and slowly cooling down) the absorbance filter fabrication is finished (Fig. 2).

4. Optical characterization

4.1. Spectral response

For determining the optical properties of the doped Epocore its spectral response is measured. At a first step, two multimode optical fibers (with a diameter of 230 µm) (Thorlabs, Dachau, Germany) were inserted at both headed self-alignment channels of the filter length under study. Then, a broadband halogen lamp (visible-NIR range) (Halogen light source, HL-2000-FHSA, Micropack, Ocean Optics, Germany) is coupled into one optical fiber. The outcoming light is collected by the second fiber, which is directly connected to a spectrometer (USB2000+, Ocean Optics, Germany). Results on transmittance as a function of the wavelength are presented in Fig. 3. A filter channel filled with non-modified Epocore is measured and considered as reference. Theoretically, such filters should present an arbitrarily low transmittance at a given wavelength range (the so-called stop-band, where light of this wavelength are adsorbed by the dye) and a high transmittance at these wavelengths where the dye does not absorb (passband). As it can be seen, they present significant stop-bands at concrete regions of the visible spectra (−5.17 dB@592.0, −3.30 dB@531.0, −4.40 dB@496.8, for lilac-, red- and yellow-doped Epocore, respectively). Regarding the passband, yellow and lilac have the zero passband penalty, whereas red-doped

Epocore has a small, but non-zero passband (−0.75 dB). Hence, we present two successful results. First, the characterized filters show a non passband in contrast to the studies existing in the literature [5,6]. In fact the existence of non passband is an improvement towards the correct search and implementation of the material defining the spectral response of the absorbance filters. Second, the shape of the stopband in Fig. 3 is opposite to the wide stopband range filter (goes from 100 nm to 200 nm) [9] allowing block the intensity light for a specific wavelength (goes from 100 to 110 nm). In the present work the dye solubility limit into the Epocore has not been reached. Hence, it is possible to increase the filtering capabilities of the UV-patternable polymers presented in this work. Consequently, it is expected to enhance the filtering capabilities of the Epocore-doped filters, obtaining similar results as these previously presented [8].

4.2. Bleaching study

Bleaching is an extremely important factor in applications in which high-power laser or long integration times are required, as for example in fluorescence measurements. During a measurement

Fig. 4. Bleaching study preformed with the red-doped Epocore and its comparison with a non-modified-Epocore polymer layer. This study is realized with a UV lamp at 365 nm (For interpretation of the references to color in this figure legend, the reader is referred to the web version of this article).

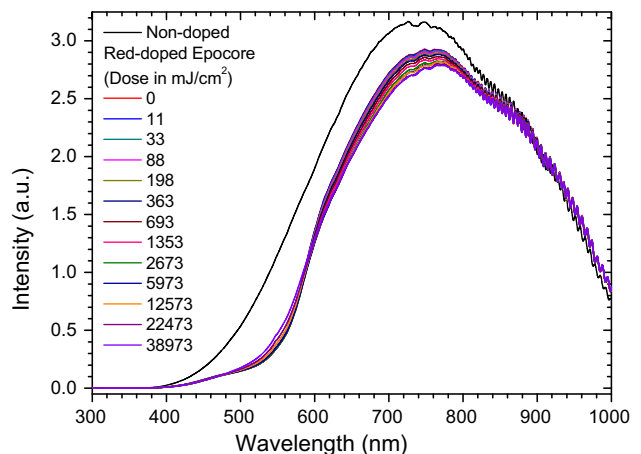the filter will be degraded by the light exposure [16]. With purpose to determine which is the degree of degradation of the dye-doped Epocore an aging study is carried out. It is performed by a controlled exposure to UV light (wavelength of 365 nm) at different doses, the results are shown in the Fig. 4. The degradation of the filters after a dose close to 40000 mJ/cm^2 is only 4%, meaning that the dye-doped Epocore still retains 96% of its filtering capability. This high photostability assures the possibility to use the proposed filters in the before mentioned applications as well as in outdoor measurements.

5. Conclusions

In this work we present the excellent structural and optical stability of the dye-doped Epocore material. We demonstrate the high ratio resolution 10:1 obtained by the fabrication of a collection of test structures by soft-lithographic process. Although the resolution decreases with the does, the structurability of the polymer remains unaltered. Moreover, there is no dye diffusion from the crosslinked polymeric matrix. Performance of the filters is demonstrated through the spectral response and the bleaching study. Three filters have studied and the transmittance values obtained prove the existence of a stopband at very concrete wavelengths into the visible range: −5.17 dB@592.0, −3.30 dB@531.0, −4.40 dB@496.8, for lilac-, red- and yellow-dye-doped Epocore respectively. Additionally, a non-passband behavior is observed for the red filter. The transmittance value is −0.75 dB. Furthermore, the bandwidth of these filters goes from 100 to 110 nm being lower than the presented values of Hofmann et al. [8]. From the spectral response we can conclude that the dye-doped Epocore polymer is a suitable material for improving selective passbands and stopbands filters. Finally, the bleaching study is carried out. After of an exposure close to 40.000 mJ/cm^2 over the red filter the degradation of the dye-doped Epocore material is only 4%. These results represent a significant step towards use dye-doped Epocore in fluorescence applications, high power or long integration times.

References

[1] A. Kristensen, S. Balslev, B. Bilenberg, M. Gersborg-Hansen, D. Nilsson, Proc. SPIE 5591 (2004) 64–71.
[2] E. Verporter, N.F. de Rooij, Proc. IEEE 91 (2003) 930–953.
[3] Y.H. Kim, K.S. Shin, J.Y. Kang, E.G. Yang, K.K. Paek, D.S. Seo, B.K. Ju, J. Micromech. Microeng. 15 (2006) 1152–1158.
[4] M. Dandin, P. Abshire, E. Smela, Lab Chip 7 (2007) 955–977.
[5] H.A. Macleod, Thin Film Optical Filters, Institute of Physics Publishing, London, 2001.
[6] M.L. Chabinyc, D.T. Chiu, J.C. McDonald, A.D. Stroock, J.F. Christian, A.M. Karger, G.M. Whitesides, Anal. Chem. 73 (2001) 4491–4498.
[7] A.H. Mahan, R. Biswas, L.M. Gedvilas, D.L. Williamson, B.C. Pan, J. Appl. Phys. 96 (2004) 3818–3826.
[8] O. Hofmann, X. Wang, A. Cornwell, S. Beecher, A. Raja, D.C. Bradley, Lab Chip 6 (2006) 981–987.
[9] A. Llobera, S. Demming, H.N. Joensson, J. Vila-Planas, H. Andersson-Svahn, S. Büttgenbach, Lab Chip 10 (2010) 1987–1992.
[10] Product information about EpoCore and EpoClad can be found at www.microresist.de.
[11] V.J. Cadarso, K. Pfeiffer, U. Ostrzinski, J.B. Bureau, G.A. Racine, A. Voigt, G. Gruetzner, J. Brugger, J. Micromech. Microeng. 21 (2011) 017003 (6pp).
[12] A. Llobera, V. Seidemann, J.A. Plaza, V.J. Cadarso, S. Büttgenbach, J. MicroElectroMech. Syst. 16 (1) (2007) 111–121.
[13] A. Llobera, R. Wilke, S. Buttgenbach, Lab Chip 4 (2004) 24–27.
[14] Product information be found at www.microchem.com.
[15] A. Llobera, S. Demming, R. Wilke, S. Büttgenbach, Lab Chip 7 (2007) 1560–1566.
[16] D. Satsoura, B. Leber, D.W. Andrews, C. Fradin, ChemPhysChem 8 (2007) 834–848.

PDMS-based, magnetically actuated variable optical attenuators obtained by soft lithography and inkjet printing technologies

S. de Pedro [a,*], V.J. Cadarso [b], X. Muñoz-Berbel [a], J.A. Plaza [a], J. Sort [c], J. Brugger [b], S. Büttgenbach [d], A. Llobera [a,d]

[a] CNM-IMB-CSIC, Esfera UAB, Campus UAB, Bellaterra, Spain
[b] Microsystems Laboratory, EPFL, Lausanne, Switzerland
[c] ICREA and Physics Department, UAB, Barcelona, Spain
[d] Institut für Mikrotechnik, Technische Universität Braunschweig, Germany

ARTICLE INFO

ABSTRACT

This paper reports and compares the implementation of magnetic variable optical attenuators (M-VOA) by two fabrication strategies. In the first case, a two-layer structure containing a non-doped polydimethylsiloxane (PDMS) layer on a magnetic PDMS (M-PDMS) layer is fabricated by soft lithography (SLT). M-PDMS is obtained by doping PDMS with different ferrofluid (FF) volumes. The second technology consists of selectively dispense FF microdroplets using the inkjet printing technique (IJP) on a non-doped, non-cured PDMS structure, previously defined by SLT. In this second case, FF volumes are encapsulated inside the polymer matrix. The optical and mechanical properties of structures fabricated using both strategies and containing similar ferrofluid amounts are compared.

1. Introduction

Micro-Electro-Mechanical Systems (MEMS) were developed in the 1970s, as a direct result derived from the advances in the semiconductor integrated circuits (IC) technologies that allowed implementation of miniaturized sensors and actuators. Semiconductor technologies for MEMS generally involve bulk and/or surface micromachining [1]. Besides its huge implantation in a large number of application fields (ranging from microfluidics to telecommunications) MEMS still present some limitations: Mechanically, they are fragile and, if not designed properly, may suffer from high internal stresses. Operationally, they present high cross sensitivity to electromagnetic interferences (EMIs), usually require further data manipulation and their application in harsh or explosive environments is highly restricted, since overheating or spikes may occur on such electrical-based devices. The use of light as interrogation/actuation mechanism overcome some of these drawbacks: light is immune to EMI, shortcuts or spikes

cannot occur on optically based devices, the electronics required for any optical system may be reduced to a cheap light source (LED) and a photodetector (PD) and they can be positioned far from the measurement area and be connected to the device by ways of optic fibers. Moreover, several light properties can be used which cannot be addressed by its electric counterparts, as could be changes in intensity [2,3], wavelength [4] or phase [5]. Mergence of the above-mentioned advantages with the micromachining techniques is achieved with the Micro-Opto-Electro-Mechanical Systems (MOEMS).

In recent years, a myriad of MOEMS have been reported with a large variety of applications, including optical switches [6], filters [7], tunable lasers [8], variable optical attenuators (VOA) [9], validating this approach. Among them, integrated VOAs are very attractive components that allow a dynamic control of the optical power coupled to a photonic integrated circuit (PIC). This has located VOAs as one of the most relevant MOEMS in telecommunications. This interest is associated to the evolution of the VOA systems during the last years, in parallel to the large expansion on telecommunications in the late 1990s and early 2000s. To date, the actuation principle of VOAs is either with comb-drive electrodes [9] or piezoelectrics [10]. Moreover it can be actuated remotely [11] reducing the complexity of the VOA structure and producing large

* Corresponding author at: Department of Micro and Nano Systems, CNM-IMB-CSIC Barcelona, Spain. Tel.: +34 93 5947700; fax: +34 93 580 1496.
E-mail address: sandra.depedro@imb-cnm.csic.es (S. de Pedro).

displacements (from tens to hundreds of μm) [12]. Surprisingly, magnetic VOAs, even though they can provide with outstanding performance (non contact actuation, large applied forces), are seldomly presented in the literature [13]. Related to the field of application, VOAs have also progressively been used in fields outside telecommunications, such as the control of coupled power in a photonic lab on a chip system [14].

An additional tendency that has recently been observed is the progressive migration from silicon to polymer technologies. This is mainly associated to the development of polymers with very interesting optical and mechanical properties. Generally speaking, polymer technologies are prone to replace in the near future silicon technology in several fields, considering the substantial decrease of the complexity (i.e. the cost per system) and the optimal mechanical properties (Young's modulus as low as 300 kPa have been reported). Over the last few years, poly(dimethylsiloxane) (PDMS) has positioned itself as a privileged polymer for defining waveguides [15], tunable microlenses [16] and photonic lab on a chip systems [14]. This may probably be due to its attractive properties, as could be the very low Young's modulus (300–800 kPa), the biocompatibility, the high transmittance (>99%) from the visible to the near infra-red wavelengths, the low cost and the technological simplicity. Despite such advantages, PDMS is mainly used for microfluidics, and only very few examples of PDMS–MOEMS have been reported [14].

Another advantage in polymer technology is that doping elements (DE) can be included in a polymeric matrix without affecting the structural properties and providing a new functionality to the polymer, which depends on the nature of the doping itself [17]. This ability, relatively easy to implement in polymer technology, requires complex and critical steps with silicon technology. A large amount of DE have been reported, whose selection depends on the required functionalization to be added to the polymer. Here, materials such as aluminum [18], carbon fibers, graphite [19] for conductivity enhancement, nickel for magnetic, mechanical and optical modulation [20] or magnetite particles (MP) [21] have successfully been included into polymeric matrices.

Generally, DE has to be homogeneously dispersed into the polymeric matrix so as to have a uniform performance. Unfortunately, DE dispersed (not dissolved) into a polymer tend to form aggregates [22] leading to a non-uniform DE distribution. In turn, this results in undesirable modifications of the mechanical properties of the polymer (e.g. stress concentration), uneven response and/or loss of transparency [23], thus limiting their applicability in MOEMS [21]. Aggregation effects can be minimized, to a certain extent, if the particles size is reduced toward the sub-10 nm range [24]. Nonetheless, even in this state, aggregation effects can occur because of interparticle interactions. In the case of nanometer-sized magnetic DE, dispersion can be enhanced using advanced coating strategies of the surface of the magnetic nanoparticles [25] leading in a stable colloidal and homogeneous suspension which is commonly referred to as magnetic ferrofluid (FF) [26,27].

In this paper we report a magnetic-VOA (M-VOA) based on two different strategies to optimize the actuation. In the first approach, a two-layer structure comprising a non-doped PDMS over a magnetic PDMS (M-PDMS) is fabricated by soft lithography (SLT). Here, M-PDMS is obtained by doping PDMS with different amounts of FF. Secondly, a given amount of FF droplets are selectively dispensed by making use of the inkjet printing technique (IJP) on a non-cured PDMS structure previously defined by SLT. In this case, different FF volumes are dispensed on specific actuation areas, close to the free end waveguide cantilever. Comparative mechanical and optical properties as a function of the applied magnetic field will be discussed.

2. Materials and methods

2.1. Reagents

PDMS (Sylgard Silicon Elastomer 184, Dow Coring Corp) prepolymer solution was prepared by mixing the elastomer and the curing agent (Sylgard Curing Agent 184, Dow Coring Corp) in 10:1 ratio (v:v), respectively. FF was purchased from Liquids Research Limited. The FF presents a uniform size distribution and low Fe_3O_4 particle agglomeration (<20 nm) dispersed into isoparaffin with 10 nm as the mean particle diameter and a saturation of 400 G. M-PDMS was obtained by adding the FF suspension to previously prepared prepolymer solution.

2.2. Design

The proposed M-VOA design is illustrated in Fig. 1a. It is composed by a self-alignment system 135 μm × 4750 μm × 250 μm [width (W)_ length (L)_thickness (T)] for self-aligning and clamping of the fiber optics. The waveguide cantilever with size (500 μm × 4000 μm × 250 μm; W_L_T), has the function to confine the light emerging from the fiber optics. Considering the design here presented, light will be confined on the waveguide only if the incidence angle is larger than the critical angle, which, for the case of a PDMS–Air interface, can be calculated to be $\theta_c = 45.17°$. This is the case of most modes when using a fiber optics with low numerical aperture (NA = 0.22 in this case). Then, the waveguide cantilever should present low propagation losses. Nevertheless, it must also be considered the high hydrophobic character of PDMS. During operation and handling, particles or dust may attach to the cantilever, causing a frustration of the TIR conditions and therefore dramatically increase the losses of the proposed VOA. To tackle this issue, two sets of parallel air mirrors have been defined at both sides of the waveguide. Such micro-optical elements were previously published by our group [28] and therefore they will only be briefly explained here. With the aim of having TIR conditions at the inner part of the cantilever that remain unaffected by particle adsorption at the surface, air structures (voids) are placed along and at both sides of the waveguide core. Here, if an internal air wall is defined, the previously described critical angle is again valid. In this context, two continuous air mirrors will provide TIR conditions throughout the cantilever, but this configuration will hamper its mechanical stability. Therefore, a compromise has to be reached between the optical and mechanical properties if this architecture wants to be used. In our case, we have implemented several small mirrors with dimensions (100 μm × 300 μm × 125 μm; W_L_T) distanced 300 μm each.

Finally, a cylindrical microlens (500 μm × 250 μm × 250 μm; W_L_T) is positioned at the free end of the waveguide cantilever. Thus, when the light traveling through the waveguide cantilever reaches the cylindrical microlens the light is focalized at the collecting fiber optics placed on a second self-alignment. Two reservoirs (4450 μm × 4000 μm × 125 μm; W_L_T), can also be observed in the design, being both of them interconnected via a microchannel (180 μm × 3600 μm × 125 μm; W_L_T) which surrounds the waveguide cantilever. These reservoirs have the function of storing either M-PDMS (SLT technology) or non-doped PMDS and FF drops (SLT + IJP technology). Using open microfluidics, such polymers will fill the microchannel by capillary.

2.3. M-VOA's fabrication

The M-VOA fabrication is schematized in Fig. 2. It is based on a standard two-level master soft lithography process. The details of this process can be found elsewhere [29] and only the major aspects are described here. A 50 μm-thick SU-8 (SU-8 50, MicroChem
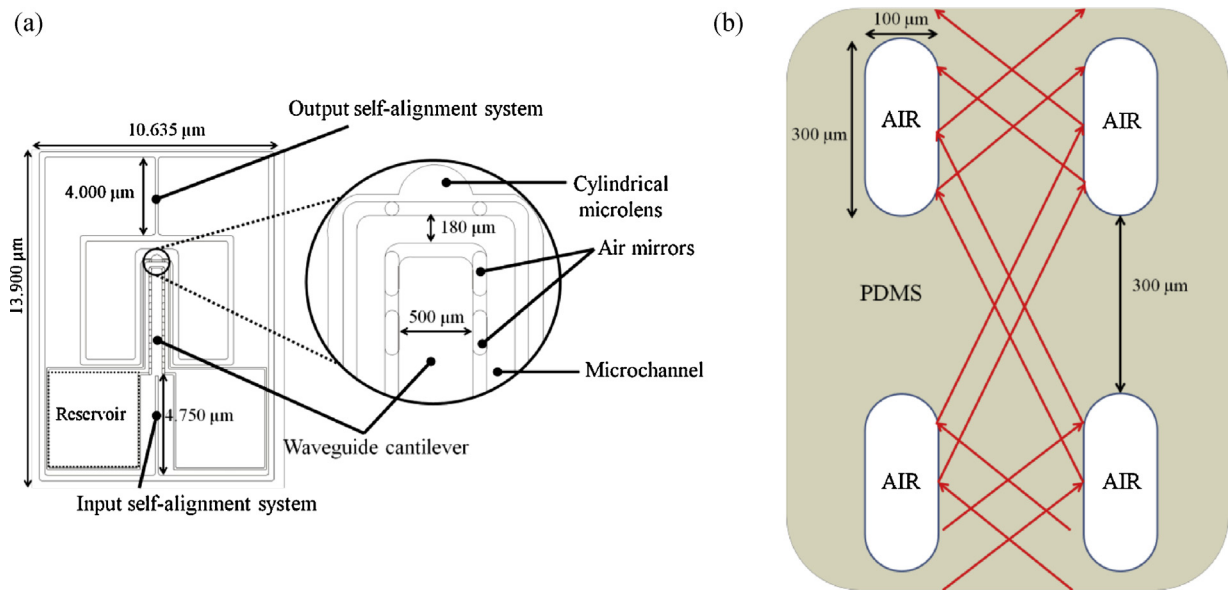
Fig. 1. (a) Top view of the M-VOAs design. Reservoirs, microchannel, self-alignment system and waveguide cantilever are observed. Moreover the detail shows the air mirrors at both sides of the waveguide cantilever, the microchannel and the cylindrical microlens at the end of the waveguide cantilever. (b) Schema of light confinement at the waveguides with the help of air mirrors. Incidence angles higher than 45.17° undergo total internal reflection (TIR) at the PDMS–air interface and therefore reflected toward the waveguide.
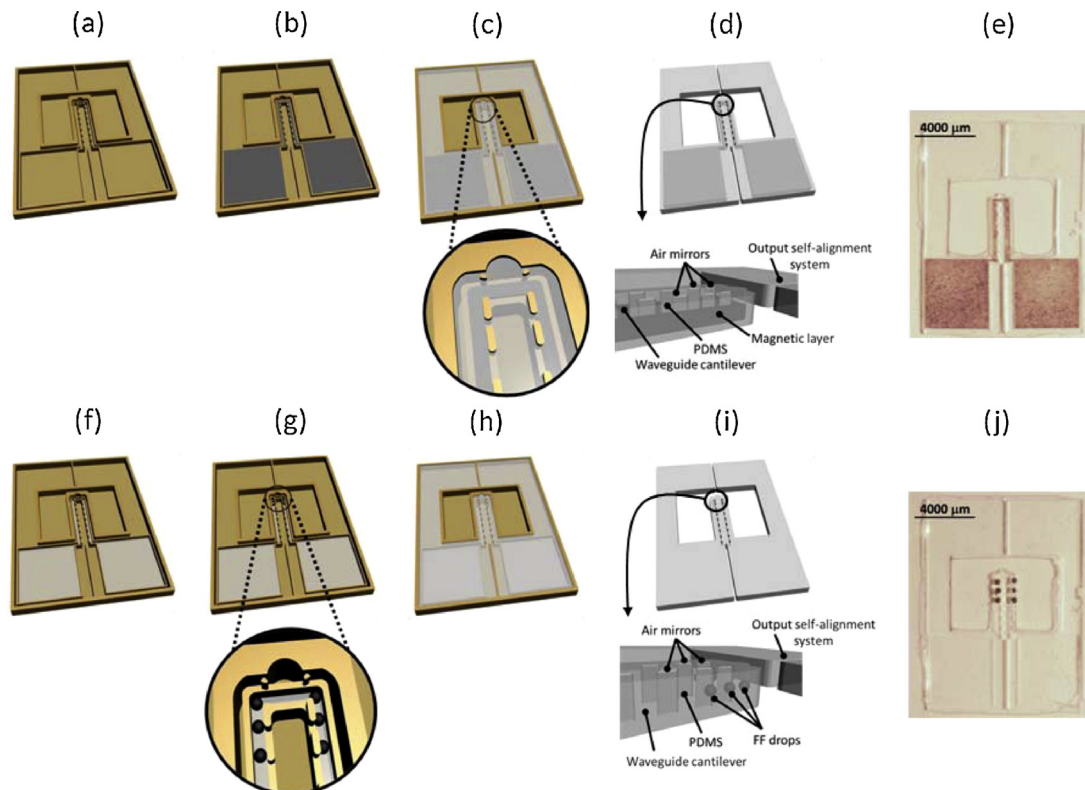
Fig. 2. Schema for the M-VOASLT and M-VOASLT+IJP fabrication processes. M-VOASLT fabrication process starts by (a) defining a two level SU-8 master. (b) First level master's reservoirs are poured with M-PDMS, (c) second level master with the non-doped PDMS pre-polymer. On the detail, both PDMS (M-PDMS and non-doped PDMS) layers can be observed. After the curing process (d) the M-VOASLT is peeled off from the master. Detail on (d) shows optical elements properly defined and perfect bonding between both polymeric layers. At this point, (e) the M-VOASLT system is finished. For M-VOASLT+IJP fabrication process is as follows: it begins with (a) the same the SU-8 master used for the SLT technology fabrication. After this (f) first level master's is poured with non-doped PDMS pre-polymer, then (g) FF drops are dispensed at the end of the free end waveguide cantilever (detail of (g)) over the non-doped PDMS pre-polymer layer. Then (h) a second layer of non-doped PDMS pre-polymer fills the remaining regions by capillarity. When the curing process is finished, the M-VOASLT+IJP (i) is peeled off from the master, an encapsulation of the FF drops in the PDMS system with all the optical elements defined is obtained (detailed image of (i)). (j) A real image corresponding with the final M-VOASLT+IJP fabricated system is shown.

Corporation, Newton, MA) layer is deposited over a 700 μm-thick soda-lime glass, followed by the soft bake (SB). Then, the first photolithographic mask defines both reservoirs and the microchannel, which are crosslinked during the post exposure bake (PEB). A second layer of 250 μm-thick SU-8 is deposited over the previous 50 μm-thick SU-8 by two consecutive depositions of 125 μm-thick SU-8 (SU-8 50, MicroChem Corporation, Newton, MA). Longer SB is required before using the second photolithographic mask, which defines the optical structures (waveguide cantilever, air gaps, cylindrical microlens, input and output self-alignment systems). After the PEB, the master is developed in propylene glycol methyl ether acetate (PGMEA, MicroChem Corporation, Newton, MA). The finished master is schematized in Fig. 2a. Next, M-VOAs are produced by using either conventional SLT or a combination of SLT and IJP. IJP is a method for generating a jet or droplets for its printing on a substrate. The system used in this work basically consists of passing a liquid through a nozzle, which is actuated piezoelectrically. Controlling the voltage, the pulselength and the frequency of the piezoelectric some microdrops can be generated achieving volumes around 1.65×10^{-4} μl per microdrop.

M-PDMS is obtained by manually mixing 0.016, 0.025 or 0.033 μl of FF into PDMS prepolymer solution. The first level of the master is filled with M-PDMS avoiding overflow (Fig. 2b). After a short curing step (5 min at 80 °C), the second level of the master is filled with non-doped PDMS prepolymer and cured for 20 min at 80 °C (Fig. 2c). Fabricated M-VOASLT is peeled off from the master (Fig. 2d). Although both levels were perfectly bonded in a single M-VOA structure, the elements of both levels are composed of different PDMS, M-PDMS and non-doped PDMS, respectively (detail in Fig. 2c and d). The bonding between both layers of different composition is achieved by optimization of the curing time process. Thus, the curing time step of the M-PDMS is lower than the time needed for the full polymerization of this elastomer. When the layer of non-doped PDMS prepolymer is deposited on the M-PDMS and a suitable curing time is applied, a complete polymerization and bonding between both layers is achieved. Fig. 2e illustrates a real image of the M-VOASLT obtained in this case. As shown, all designed elements are perfectly defined in the final M-VOA.

In the case of M-VOA obtained by a combination of SLT and IJP (M-VOASLT+IJP), the first level of the master is filled with non-doped PDMS prepolymer (Fig. 2f) and partially cured for 5 min at 80 °C. Next, FF drops are dispensed by IJP in the microchannel area close to the end of the waveguide cantilever (Fig. 2g). The volumes of FF dispensed are 0.018, 0.026 or 0.030 μl, depending on the case. Then, the second level is filled with another non-doped PDMS prepolymer layer and cured for 20 min at 80 °C (Fig. 2h). Finally, the fabricated M-VOASLT is peeled off the master (Fig. 2i). With this strategy, FF droplets remain trapped on a single M-VOA structure (detail Fig. 2i). The real image, of the M-VOASLT+IJP with the elements designed on the previous section is shown in Fig. 2h).

2.4. Setup

For the mechanical characterization, the M-VOA is placed on a micropositioning platform over a magnet. This magnet is located on a stage which is able to move vertically thereby changing the applied magnetic field to the waveguide cantilever. The waveguide cantilever deflection at each magnetic field is measured by following the procedure detailed below. Firstly, the 633 nm wavelength laser beam (Laser source, 633 nm, 10 mW, model 1137P, JDS Uniphase) is focused at the free end waveguide cantilever without an external magnetic field ($B=0$) and with an external magnetic field ($B \neq 0$), collecting the reflected beam on a screen. In the first case ($B=0$), the distance from the waveguide cantilever end and the spot is taken as reference (Δy_0). When $B \neq 0$, cantilever bending causes a variation of the spot position (Δy). Thus, the relative
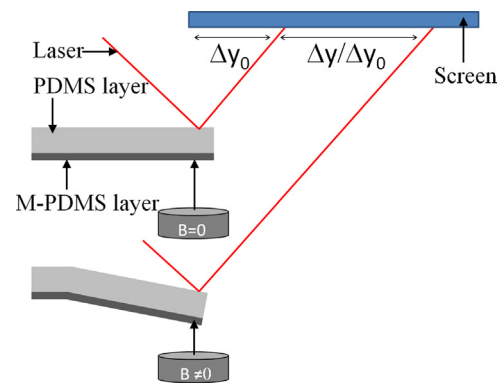

Fig. 3. Sketch of the setup used for the mechanical characterization which shows the laser beam focused on the free waveguide cantilever end, the reflected beams on the screen, the magnet and the M-VOASLT's waveguide cantilever.

deflection as $\Delta y/\Delta y_0$ as a function of the magnetic field is determined (Fig. 3).

Concerning the optical characterization, M-VOAs are placed on a support with a magnet (as before). A 125 μm multimode fiber optic located at the input self-alignment system couples the light from the 635 nm wavelength laser (Laser source, 635 nm, 2.5 mW, Model S1FC, Thorlabs GMBH) to the waveguide cantilever. The cylindrical microlens at the end of the cantilever focuses the propagating light to the fiber optics located at the output self-alignment system, already connected to a power meter (Newport Power Meter, Model 1930F-SL). Both M-VOAs are externally actuated by a magnetic field. When $B=0$ the intensity collected is $I0$, whereas for $B \neq 0$ the intensity corresponds to If. In this way, the relative optical losses (ROL = $10 \log(If/I0)$) are determined as a function of the magnetic field, Fig. 4.

3. Results and discussion

3.1. Mechanical characterization

For the mechanical characterization of the M-VOAs, the deflection of the cantilever is measured by using the setup described in the previous section. Fig. 5 shows the variation of the deflection with the applied magnetic field for M-VOASLT and M-VOASLT+IJP containing similar FF amount.

In all cases, deflection increases with the applied magnetic field until saturation around 0.29–0.57 kG. However, the deflection magnitude at saturation depends on two factors: (i) the FF amount and (ii) the fabrication method. As expected, larger deflection magnitudes are obtained when increasing the FF volume in M-VOASLT and M-VOASLT+IJP. On the contrary, when comparing M-VOA with similar FF volumes, larger deflection magnitudes are
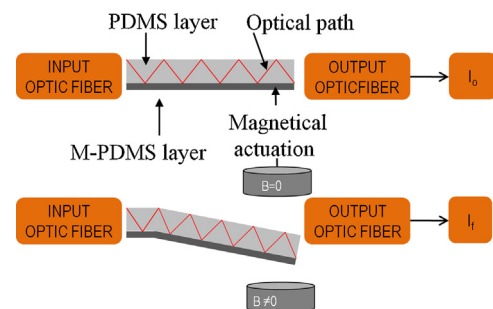

Fig. 4. Sketch of the setup used for the optical characterization which shows the input/output optic fiber, the optical path followed by the light guided inside the waveguide cantilever and its behavior for $B=0$ and $B \neq 0$.
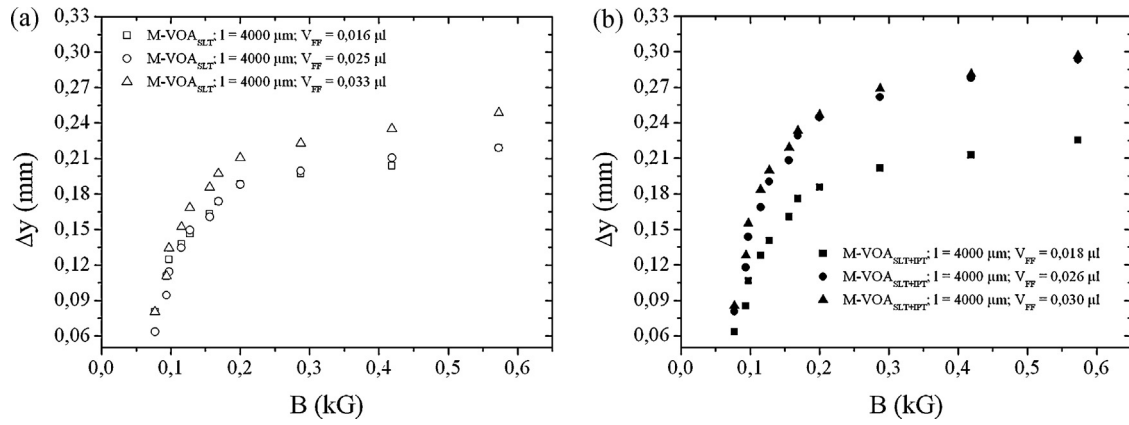
Fig. 5. Deflection (Δy) as a function of applied magnetic field (B) with a waveguide cantilever length of $l = 4000$ μm and for (a) magnetic variable optical attenuator fabricated by soft lithography (M-VOASLT) with different FF volumes (V_{FF}) of 0.016 μl, 0.025 μl and 0.033 μl and for (b) magnetic variable optical attenuator fabricated by soft lithography and inkjet printing (M-VOASLT+IJP) with V_{FF} of 0.018 μl, 0.026 μl and 0.030 μl.

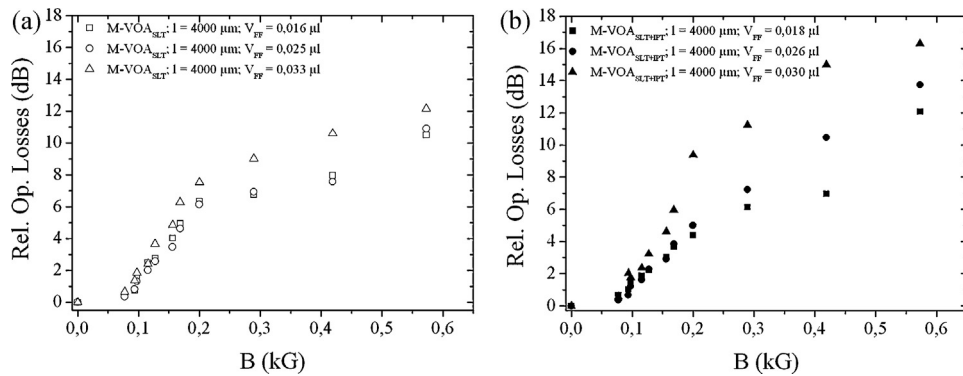**Fig. 6.** Relative optical losses as a function of applied magnetic field (B) with a waveguide cantilever length of $l = 4000$ μm and for (a) magnetic variable optical attenuator fabricated by soft lithography (M-VOASLT) with different FF volumes (V_{FF}) of 0.016 μl, 0.025 μl and 0.033 μl and for (b) magnetic variable optical attenuator fabricated by soft lithography and inkjet printing (M-VOASLT+IJP) with V_{FF} of 0.018 μl, 0.026 μl and 0.030 μl.

always obtained by M-VOASLT+IJP (see Table 1). This result may be due to the different distribution of FF in both structures. That is, whereas for M-VOASLT, FF is homogeneously distributed along the cantilever waveguide, in the case of M-VOASLT+IJP, it is more concentrated at the free end of the cantilever waveguide, becoming more sensitive to applied magnetic field.

3.2. Optical characterization

Optical characterization is performed as indicated in previous sections. The variation of the relative optical losses with the applied magnetic field of both M-VOASLT and M-VOASLT+IJP structures containing similar FF volumes are represented in Fig. 6. Firstly, it can be observed how the SLT + IJP technology provides with VOAs with much lower losses. This is associated to the fact that by using SLT + IJP, the FF is located at the regions where does not interact with the optical light beam. Conversely, with SLT, the M-PDMS is located just beneath the non-doped PDMS. Light

propagating inside the cantilever is also coupled to the M-PDMS because of the very similar refractive index. Here, light enters in a high absorbent/scattering area. Therefore, it becomes logical why the SLT experiences higher losses at any applied magnetic field as compared to the SLT + IJP counterpart. For both strategies, the relative optical losses increase with the applied magnetic field until reaching saturation. Again, larger relative optical losses are recorded when increasing the FF volume in the M-VOA structure. Additionally, M-VOASLT+IJP structures also show larger relative optical losses when compared with M-VOASLT of similar FF volume (Table 2), which means a higher sensitivity.

Finally, the dynamic range associated with the M-VOASLT was measured to be 6.8 dB, whereas for the M-VOASLT+IJP, this magnitude increased until 8.9 dB (identical in the whole visible spectra measured, which is in agreement with the PDMS transparency at such wavelengths, as well as with the highly multimodal behavior of the waveguide cantilever). In both cases, the response time was 200 ms. According to these figures, we consider that such systems

Table 1
Maximum deflection (Δy_{max}) for M-VOASLT and M-VOASLT+IJP for different FF volumes (V_{FF}).

V_{FF} (μl)		Δy_{max} (mm)	
M-VOA$_{SLT}$	M-VOA$_{SLT+IJP}$	M-VOA$_{SLT}$	M-VOA$_{SLT+IJP}$
0.016	0.018	0.138	0.162
0.025	0.026	0.156	0.203
0.033	0.030	0.168	0.211

Table 2
Relative optical losses for M-VOASLT and M-VOASLT+IJP for different FF volumes (V_{FF}).

V_{FF} (μl)		Rel. op. losses (dB)	
M-VOA$_{SLT}$	M-VOA$_{SLT+IJP}$	M-VOA$_{SLT}$	M-VOA$_{SLT+IJP}$
0.016	0.018	10.0	11.4
0.025	0.026	10.5	13.4
0.033	0.030	11.5	15.7

are extremely promising in applications where bandwidth prevails over response time. An example would be in photonic lab on a chip, where VOAS are currently used to avoid damage of a cell culture due to excessive irradiation.

4. Conclusions

Two different fabrication strategies based on either conventional SLT or the combination of SLT and IJP are used for the fabrication of M-VOA using PDMS as constituent material. PDMS doped with FF (M-PDMS) and trapped FF microdroplets provide the magnetic properties of M-VOASLT and M-VOASLT+IJP. M-VOASLT+IJP always shows larger deflection magnitudes and relative optical losses when compared with M-VOASLT with a similar FF volume. The FF distribution, much more concentrated to the free end of the waveguide cantilever, seems to be the cause of the enhanced sensitivity recorded by M-VOASLT+IJP.

Acknowledgments

References

[1] M.J. Madou, Fundamentals of Microfabrication, second ed., CRC Press, Boca Raton, 2002.
[2] E. Abbaspour, R.-S. Huang, C.Y. Kwok, Novel optical accelerometer, IEEE Electron Device Lett. 16 (1995) 166–168.
[3] S.J. Lee, D.W. Cho, Development of a micro-opto-mechanical accelerometer based on intensity modulation, Microsyst. Technol. 10 (2004) 147–154.
[4] T.K. Gangopadhyay, Prospects for fibre Bragg gratings and Fabry–Pebrot interferometers in fibre-optic vibration sensing, Sens. Actuators A: Phys. 113 (2004) 20–38.
[5] F.A. Castro, S.R. Carneiro, et al., 2-mode optical fiber accelerometer, Opt. Lett. 17 (1992) 1474–1745.
[6] C. Marxer, et al., Vertical mirrors fabricated by reactive ion etching for optical switching appplications, in: Proceedings of 10th Workshop on MEMS, 1997, pp. 1–6.
[7] T. Hashimoto, et al., Hybrid integration of spot-size converted laser diode on planar lightwave circuit platform by passive alignment technique, IEEE Photon. Tech. Lett. 8 (1996) 1504–1506.
[8] B. Pezeshki, New approaches to laser tunning, Opt. Photon. News (2001) 34–38.
[9] C. Marxer, P. Griss, N.F. de Rooij, A variable optical attenuator based on silicon micromechanics, IEEE Photon. Tech. Lett. 11 (1999) 233–235.
[10] K.H. Koh, C. Lee, T. Kobayashi, A piezoelectric-driven three-dimensional MEMS VOA using attenuation mechanism with combination of rotational and translational effects, J. Microelectromech. Syst. 19 (2010) 1370–1379.
[11] M. Khoo, C. Liu, Micro magnetic silicone elastomer membrane actuator, Sens. Actuators A: Phys. 89 (2001) 259.
[12] F. Pirmoradi, L. Cheng, M. Chiao, A magnetic poly(dimethylsiloxane) composite membrane incorporated with uniformly dispersed, coated iron oxide nanoparticles, J. Micromech. Microeng. 2 (2010) 7.
[13] S.H. Hung, et al., An electro-magnetic micromachined actuator monolithically integrated with a vertical shutter for variable optical attenuation, J. Micromech. Microeng. 18 (2008) 1–8.
[14] A. Llobera, G. Villanueva, et al., Polymeric MOEMS variable optical attenuator, IEEE Photon. Tech. Lett. 18 (2006) 2425–2427.
[15] D.A. Chang-Yen, R.K. Eich, B.K. Gale, A monolithic PDMS waveguide system fabricated using soft-lithograpy techniques, J. Lightwave Technol. 23 (2005) 2088–2093.
[16] A. Llobera, R. Wilke, S. Büttgenbach, Optimization of poly(dimethylsiloxane) hollow prisms for optical sensing, Lab Chip 5 (2005) 506–511.
[17] S. de Pedro, V.J. Cadarso, X. Muñoz-Berbel, J.A. Plaza, J. Sort, J. Brugger, S. Büttgenbach, A. Llobera, Magentically-actuated variable optical attenuators using ferrofluid-doped elastomer implemented by combination of soft lithography and inkjet printing technologies, in: Conference Proceedings IEEE MEMS 2013, Taiwan, 2013.
[18] E. Back, Magnetite gives new recyclable dense polymers for the automotive industry Plastics Reborn in 21st Century Vehicles, in: Conference Proceedings, Rapra Technical Ltd, 1999.
[19] J.A. King, et al., Electrically and thermally conductive nylon 6.6, Polym. Compos. 20 (1999) 643–654.
[20] K.L. Tsai, et al., Magnetic, mechanical, and optical characterization of a magnetic nanoparticle-embedded polymer for microactuation, J. Micromech. Microeng. 20 (2011) 65.
[21] M. Suter, et al., A photopatternable superparamagnetic nanocomposite: material characterization and fabrication of microstructures, Sens. Actuators B: Chem. 156 (2011) 433.
[22] M. Suter, et al., Superparamagnetic photosensitive polymer nanocomposite for microactuator, in: Solid-State Sensors, Actuators and Microsystems Conference, 2009. Transducers 2009. International, 2009, p. 869.
[23] F. Pirmoradi, L. Cheng, M. Chiao, A magnetic poly(dimethylsiloxane) composite membrane incorporated with uniformly dispersed, coated iron oxide nanoparticles, J. Micromech. Microeng. 20 (2010) 1.
[24] Q.A. Panjhurst, J. Connolly, S.K. Jones, J. Dobson, Applications of magnetic nanoparticles in biomedicine, J. Phys. D: Appl. Phys. 36 (2003) 167–181.
[25] A.-H. Liu, E.L. Salabas, F. Achüth, Magnetic nanoparticles: synthesis, protection, functionalization and application, Angew. Chem. 46 (2007) 1222–1244.
[26] A.-H. Lu, E.L. Salabas, F. Schüth, Magnetic nanoparticles: synthesis, protection, functionalization and application, Angew. Chem. 46 (2007) 1222.
[27] A.K. Gupta, M. Gupta, Synthesis and surface engineering of iron oxide nanoparticles for biomedical applications, Biomaterials 26 (2005) 3995.
[28] A. llobera, et al., Enhancement of the response of poly(dimethylsiloxane) hollow prisms through air mirrors for absorbance-based sensing, Talanta 75 (2008) 473–479.
[29] A. Llobera, et al., Poly(dimethylsiloxane) waveguide cantilevers for optomechanical sensing, IEEE Photon. Tech. Lett. 21 (2009) 7981.

Polymeric variable optical attenuators based on magnetic sensitive stimuli materials

S de Pedro[1], V J Cadarso[2,3], T N Ackermann[1], X Muñoz-Berbel[1], J A Plaza[1], J Brugger[2], S Büttgenbach[4] and A Llobera[1,4]

[1] Instituto de Microelectrónica de Barcelona, IMB-CNM (CSIC), Esfera UAB, Campus UAB, 08193 Bellaterra, Spain
[2] Microsystems Laboratory, École Polytechnique Fédérale de Lausanne (EPFL), 1015 Lausanne, Switzerland
[3] Laboratory for Micro- and Nanotechnology, Paul Scherrer Institut (PSI), 5234 Villigen, Switzerland
[4] Institut für Mikrotechnik, Technische Universität Braunschweig, 38106 Braunschweig, Germany

E-mail: andreu.llobera@imb-cnm.csic.es

Abstract

Magnetically-actuable, polymer-based variable optical attenuators (VOA) are presented in this paper. The design comprises a cantilever which also plays the role of a waveguide and the input/output alignment elements for simple alignment, yet still rendering an efficient coupling. Magnetic properties have been conferred to these micro-opto-electromechanical systems (MOEMS) by implementing two different strategies: in the first case, a magnetic sensitive stimuli material (M-SSM) is obtained by a combination of polydimethylsiloxane (PDMS) and ferrofluid (FF) in ratios between 14.9 wt % and 29.9 wt %. An M-SSM strip under the waveguide-cantilever, defined with soft lithography (SLT), provides the required actuation capability. In the second case, specific volumes of FF are dispensed at the end of the cantilever tip (outside the waveguide) by means of inkjet printing (IJP), obtaining the required magnetic response while holding the optical transparency of the waveguide-cantilever. In the absence of a magnetic field, the waveguide-cantilever is aligned with the output fiber optics and thus the intrinsic optical losses can be obtained. Numerical simulations, validated experimentally, have shown that, for any cantilever length, the VOAs defined by IJP present lower intrinsic optical losses than their SLT counterparts. Under an applied magnetic field (B_{app}), both VOA configurations experience a misalignment between the waveguide-cantilever and the output fiber optics. Thus, the proposed VOAs modulate the output power as a function of the cantilever displacement, which is proportional to B_{app}. The experimental results for the three different waveguide-cantilever lengths and six different FF concentrations (three per technology) show maximum deflections of 220 μm at 29.9 wt % of FF for VOA_{SLT} and 250 μm at 22.3 wt % FF for VOA_{IJP}, at 0.57 kG for both. These deflections provide maximum actuation losses of 16.1 dB and 18.9 dB for the VOA_{SLT} and VOA_{IJP}, respectively.

Keywords: PDMS, ferrofluid, magnetic actuation, VOA, MOEMS

(Some figures may appear in colour only in the online journal)

1. Introduction

Since the first MEMS were developed during the mid-1970s [1], the commercial and research interest in such systems has experienced a dramatic growth, with its subsequent implementation in a large number of application fields. Among them,

RF-MEMS [2], power MEMS [3], or optical MEMS (also known as micro-opto-electro-mechanical systems, MOEMS [4]) can be highlighted.

This development cannot be fully understood without the concomitant development of new materials and technologies. Initially, silicon was the most common material used

in MEMS. Nevertheless, in an attempt to reduce the cost and increase mechanical robustness, other materials started to be used. Among them were polymers exhibiting attractive physicochemical properties [5]. For example, polymeric materials such as polydimethylsiloxane (PDMS), poly(methyl methacrylate) (PMMA), or polystytrene (PS) have a lower Young's modulus (Y) than silicon (Y_{PDMS} = 800 KPa, Y_{PMMA} = 2.4 MPa, Y_{PS} = 3.5 GPa and Y_{Si} = 169 GPa, respectively). The advantages of using materials with a lower Y are two-folded. On the one hand, polymer structures may have larger deformations for the same applied stimulus compared to an equivalent silicon counterpart. On the other hand, the decrease in Y brings a relaxation of the design and fabrication constraints and thus the possibility of defining MEMS with similar mechanical properties as silicon MEMS, but using a simpler technology (i.e. wider/thicker structures).

MEMS sensitive to a given external stimulus requires an active material within its geometry. Generally, silicon and polymers are non-active materials. Therefore this property has to be externally conferred. Here, the main limitation regarding silicon is that it can only be surface-functionalized. Conversely, bulk functionalization can be obtained using polymers with the so-called sensitive stimuli materials (SSMs [6]). They respond to an external stimuli such as a change in temperature, pH, solvent, electric or/and magnetic field. Among them, the advantages of a magnetic stimulus are either in actuation (contactless, response time), fabrication (no percolation level required) and long-term stability (porosity not critical). Thus, a magnetic SSM (M-SSM), understood as being the combination of an active magnetic material (filler) and a polymer (host matrix), is one of the most interesting functional materials for MEMS applications.

Regarding the host matrix, it has previously been discussed that PDMS has a very low Y (800 KPa [7]). Furthermore, this material has a high transmittance in the UV-NIR wavelength range, making it interesting for MOEMS [8]. Additionally, it has other unique properties such as biocompatibility, low cost and fabrication simplicity [9, 10], which makes PDMS one of the most promising host matrices for M-SSMs.

The performance of MEMS based on M-SSMs strongly depends not only in the host matrix, but also on the physicochemical properties of the filler. Among the different fillers with magnetic properties available, it has been shown that ferrofluids (FFs) can be homogeneously dispersed in PDMS matrices [11]. Among the different FFs, magnetite-based ones present either a superparamagnetic or single-domain state, even though they also show lower permeability and saturation magnetization compared to other soft materials [12]. Examples of FF-based M-SSMs and their implementation can be found at [13], where a 7 mm-diameter and 35 μm-thick PDMS membrane loaded with 40 wt % of FF is reported. This magnetic membrane achieved a deflection of 620 μm for a magnetic actuation of 4.1 kG. In another published work, Filipcsei and Zrinyi studied changes in the geometry in response to a magnetic field applied to a magnetic sphere with 20 wt % of FF in the polymer. In this case a variation of 890 μm ± 0.05 μm in its diameter was observed for 4.0 kG [14].

Another important aspect when implementing MEMS sensitive to a given stimulus is the detection method for such an actuation. Here, different strategies may be used, even though the compatibility between the actuation and the detection must be assured. In this context, MEMS detection is mostly piezoelectric [15] or capacitive [16], whereas several actuation principles can be found in the literature (magnetic, thermal, etc). Although effective, such electrical detection presents significant drawbacks, the most important one being the crosstalk due to electromagnetic interference (EMI). This issue can be tackled by using the above mentioned MOEMS approach [17], assuring the decoupling between the detection and the actuation. An example of such compatibility can be found in a variable optical attenuator (VOA). Initially, this MOEMS was of key importance in wavelength demultiplexing (WDM) networks to unify powers across the spectrum while minimizing crosstalk and keeping the signal-to-noise ratio (SNR) above a specific threshold [18]. Already in 2008 there had been a huge progress in this specific MOEMS, as reported by Lee in his review [19]. Most of them were relying on fragile surface micromachined silicon beams and made use of electrostatic actuation. In this context, Li *et al* made a significant improvement by merging a thermally-controlled micro-shutter which was assembled via a scratch drive actuator (SDA [20]). Still, the final application for this VOA-MOEMS was mostly restricted to WDM. Nevertheless, other applications where optical power control is required, such as optical membranes in chemical sensors [21], could also benefit from VOA-MOEMS technology. There in, key aspects in WDM such as the wavelength of the polarization-dependent loss (WDL and PDL, respectively) becomes less important compared to mechanical robustness, a broad working wavelength range, biocompatibility, and low cost. Focusing on these applications, polymer technology was used for defining a VOA-MOEMS in which thermal actuation was merged with photonic actuation [22]. Although effective, this MOEMS-VOA presents early ageing of the thermal actuator. Surprisingly, even though optical readout and magnetic actuation are fully compatible mechanisms and they have been combined, either in optical systems for tuning the refractive index [23] or attenuation [24], their joint implementation in a MOEMS has seldom been reported [25]. Finally, it is important to mention that MOEMS using an M-SSM obtained by mixing PDMS with different FF loads has also rarely been demonstrated [26]. Therefore, its applicability for VOAs (or for MEMS/MOEMS in general) will also be validated here.

In this work, we present two MOEMS-VOA based on PDMS, M-SSMs and FFs (hereafter only mentioned as VOA for simplicity). They have an identical design, but they have been fabricated using two different techniques: in the first case, soft lithography (SLT [27]) has been used for defining a VOA with two polymer layers (non-doped PDMS and an M-SSM). The purpose of the non-doped PDMS layer is to confine the light with low losses due to the high transmittance of the PDMS, whereas the function of the M-SSM layer is to provide the VOA with the capability to be magnetic actuated. The second proposed VOA is obtained by using an inkjet printing technique (IJP). The IJP allows a given amount of

FF droplets to be dispensed (~165 pL per droplet) onto a non-cured PDMS structure previously defined by SLT. The FF droplets are trapped with a second, non-doped PDMS layer resulting in a VOA with the FF located in specific actuation areas. The performance of both VOA technologies has been evaluated and compared both mechanically and optically. This is the first time, to the best of our knowledge, that PDMS-based VOAs are reported as being aimed towards biochemical applications.

2. Materials and methods

2.1. Reagents

The negative-tone epoxy-based polymer SU-8 50 and its developer propylene glycol methyl ether acetate (PGMEA), both from MicroChem, Corp, USA were used as received following the recipes previously developed by our group [28]. PDMS (a Sylgard base Elastomer and curing agent) was acquired at Dow Corning Corp., USA. The FF was purchased from Liquids Research Ltd, UK. In accordance with its datasheet, the FF presents a uniform size distribution and low Fe_3O_4 particle agglomeration (< 20 nm) dispersed into isoparaffin with 10 nm as the mean particle diameter and a saturation of 0.4 kG.

2.2. Design and simulation

For coherence during comparison, all the VOAs presented in this work have the same overall design, as illustrated in figure 1(*a*). This requires two photolithographic mask levels, and includes several micro-optical elements. The VOAs are fabricated using two different strategies resulting in two distinct distributions of the FF. In the first one, labeled VOA_{SLT}, the FF is first mixed with non-doped PDMS to obtain an M-SSM, which is then poured in a U-shaped stripe along the waveguide-cantilever's length (see figure 1(*b*)). In the second strategy, named VOA_{IJP}, the FF droplets are locally placed over the U-shaped stripe filled with non-doped PDMS (see figure 1(*c*)).

From an optical point of view, the VOA comprises a self-alignment element which clamps and aligns the input fiber optics with the waveguide-cantilever (having a cross section of 500 (width) $\times$ 250 μm (thickness) and lengths of $l_1 = 4000 \mu$m, $l_2 = 5000 \mu$m and $l_3 = 6000 \mu$m. It is known that the optical losses in the M-SSM increase with the FF concentration [29]. Hence, two sets of air mirrors [30] are distributed along the cantilever axis obtaining a Total Internal Reflection (TIR) waveguide to either reduce (for VOA_{SLT}) or completely prevent (for VOA_{IJP}) the interaction between the regions containing the FF (both the M-SSM and droplets) and the optical path, as also shown in figures 1(*b*)) and 1(*c*). These mirrors were designed inside the cantilever considering the real part of the refractive indices (RI) of the materials involved (PDMS, $n_{PDMS} = 1.41$ and air, $n_{air} = 1.00$). Finally, at the free end of the waveguide-cantilever, a cylindrical microlens is defined, which focuses the guided light to a second fiber optic, located at the output self-alignment element.

From a magnetic point of view, the design includes two reservoirs to be used in an open microfluidics approach. They are connected with a U-shaped microchannel that circumvents the waveguide-cantilever at its bottom section. For the SLT approach, the M-SSM will be dispensed at the reservoirs, filling the microchannel and forming a magnetic polymeric stripe on polymerization. A second non-doped PDMS confers the required waveguiding capability to the VOA. Figure 1(*d*)) shows a transversal view for the VOA_{SLT} where the first M-SSM layer and the second non-doped PDMS layer are observed. For the IJP, the VOA is obtained using the non-doped PDMS and FF droplets. The latter material will only be dispensed at the cantilever tip and located at the top of the first level of the non-doped PDMS and at the area outside the optical axis of the VOA, as shown in figure 1(*e*), thus preventing the FF-light interaction. In both approaches, an external magnetic field causes a misalignment between the waveguide-cantilever and the output fiber optics, resulting in a modulation of the actuation losses as a function of the magnetic field.

It is also important to consider the contribution of both the M-SSM and the FF to the VOA stiffness (mainly defined with the non-doped PDMS). This contribution depends on both the geometrical parameters and the material properties (Young modulus) of the cantilever. To this effect, the following considerations were taken: in the case of the SLT configuration, preliminary measurements show that changing the FF concentration from 14.9% to 29.9% while synthetizing the M-SSM causes an increase of 50% in the Young's modulus. This is in agreement with previously reported results [31]. To minimize such an effect, the width of the magnetic stripes (again, obtained with an M-SSM) was reduced to 25% of the cantilever's width and they were only located in the lower half of the cantilever's cross section (this allows efficient magnetic actuation while preserving its filling simplicity and ease of fabrication). By using this configuration, the contribution of the stripes to the cantilever's stiffness was reduced to a maximum value of 12.5%. When related to the IJP approach, the FF droplets were isolated, making its effective width much smaller compared to that of the cantilever. In addition, the minimization of its contribution is assured by locating them in the center of the cantilever's cross-section. Combining all these aspects, it can be assumed that in IJP configuration, the FF contribution to the Young's modulus can be considered negligible.

Optical simulations of the proposed VOA approaches were done using Trace Pro software (Lambda Research, Littleton, MA, USA). Figure 2 shows the ray-tracing results for both VOAs (with an identical length of 4000 μm) with no applied magnetic field (straight cantilever). The simulations were performed with a 3D-model mimicking the real VOAs. To this effect, the light was numerically coupled to the waveguide-cantilever using the specifications of both the input (core diameter of 105 μm, numerical aperture of 0.22) and output (core diameter of 200 μm, numerical aperture of 0.39) fiber optics. For an accurate simulation of the VOAs, the FF was also included. Here, according to the datasheet, the real part of the RI of the FF was $n_{FF} = 1.63$ and is absorbent to all wavelengths in the visible range. The real part of the RIs of

	VOA$_1$	VOA$_2$	VOA$_3$
a (µm)	13410	14410	15310
b (µm)	10135	10135	10135
l (µm)	4000	5000	6000
c (µm)	180	180	180
e (µm)	300	300	300
f (µm)	500	500	500
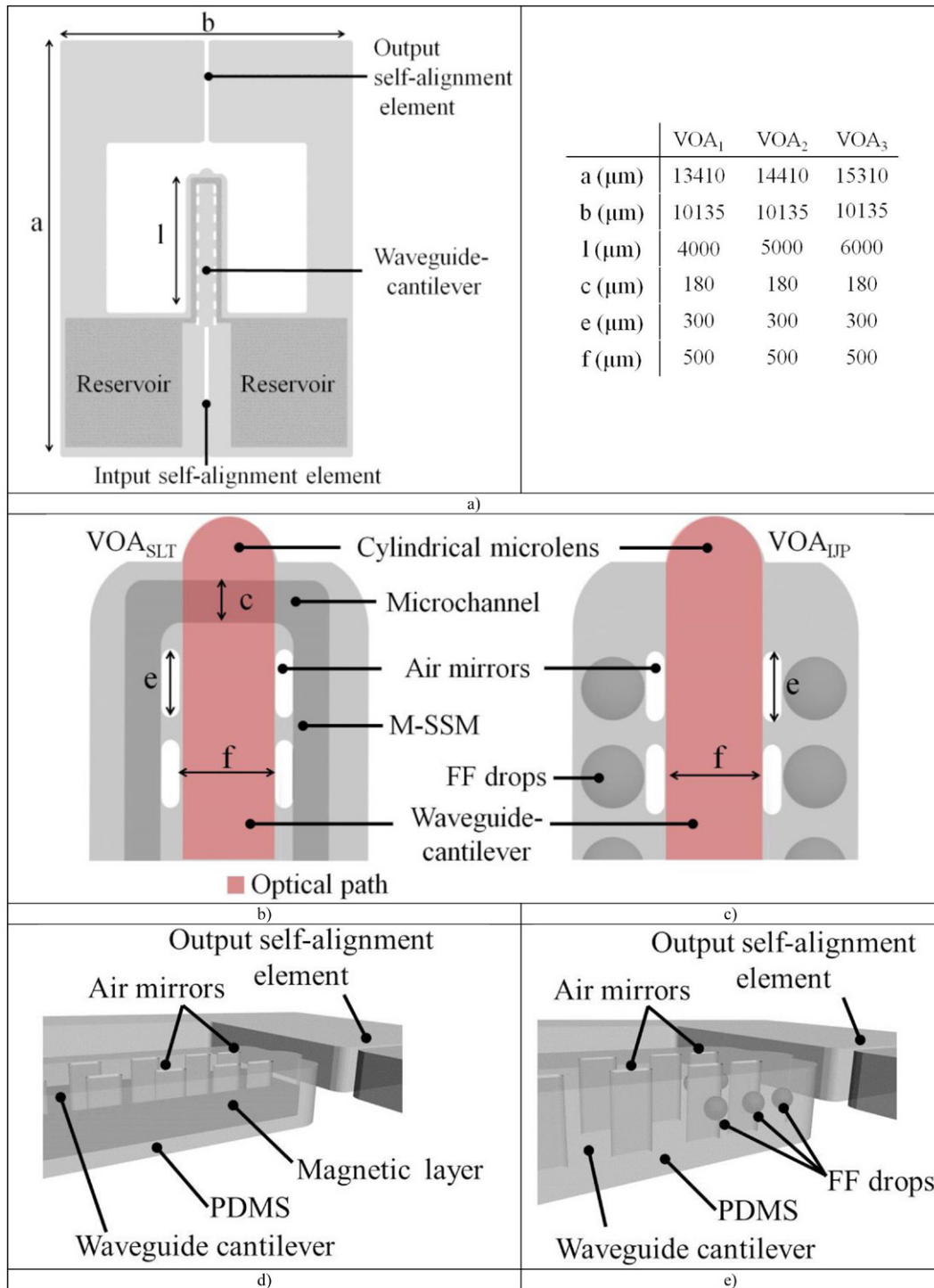
Figure 1. (*a*) Top view of the VOA based on the M-SSM, showing its components: Reservoirs, input/output self-alignment elements and waveguide-cantilever, as well as their dimensions. (*b*) and (*c*) Show a detailed schema of both the VOAs obtained for SLT and IJP, respectively. The common elements are the cylindrical microlens, the waveguide-cantilever and the air mirrors (the optical path is in both cases shown in red). (*b*) Also shows the U-shaped microchannel where the M-SSMs are defined, whereas (*c*) presents the position of the FF in the area located between the air mirrors and the lateral waveguide-cantilever facets. (*d*) A transversal view of where the M-SSM layer on the bottom waveguide cantilever non-doped layer for the VOA$_{SLT}$ is observed. (*e*) The same transversal view of the VOA$_{IJP}$, where the FF drops are localized at the cantilever tip on the non-doped layer.

the M-SSM with different weight fractions was calculated using the Bruggemann effective media approximation [32], assuming spherical inclusions of FF in the PDMS host-material. Thus, for M-SSM with 14.9%, 22.8% and 29.9% weight FF fractions, the RIs are 1.44, 1.46 and 1.47, respectively.

Figures 2(*a*) and (*b*) shows the ray tracing results (red lines) along the waveguide-cantilever in VOAs with similar FF weight fractions (14.9% and 14.8% for VOA$_{SLT}$ and VOA$_{IJP}$, respectively). Most of the coupled light remains confined between the two sets of air mirrors. At the cantilever's free end,
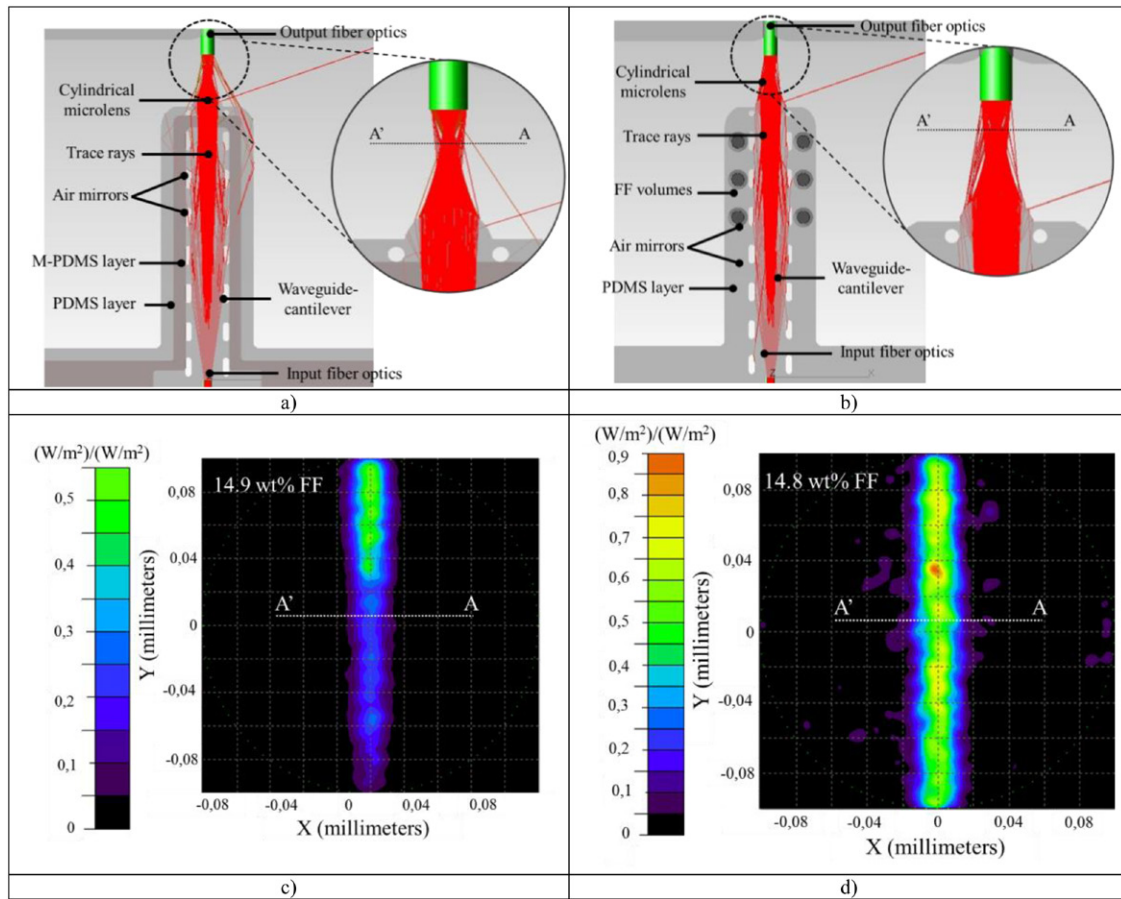
Figure 2. Ray-tracing simulation for both VOAs, with a $4000\,\mu$m-long waveguide-cantilever and without magnetic actuation (B_{app} = 0). The light is guided along the air-mirror-based waveguide and focused by the lens for (*a*) VOA$_{SLT}$ (14.9 wt% of FF) and (*b*) VOA$_{IJP}$ (14.8 wt% of FF) at the output fiber optics. The corresponding irradiance maps for (*c*) VOA$_{SLT}$ (14.9 wt% of FF) and (*d*) VOA$_{IJP}$ (14.8 wt% of FF), where the light profile cross-section at the focal point of the cylindrical lens is shown. The cylindrical lens forms in both cases a light sheet, while focusing along the horizontal but not the vertical axis.

the confined light is focused on the output fiber optics with the help of the cylindrical lens. The irradiance maps in figures 2(*c*) and (*d*), corresponding to VOA$_{SLT}$ and VOA$_{IJP}$, respectively, show the light profile cross-section at the focal point of the cylindrical lens. As can be seen, the light is focused along the horizontal but not the vertical axis, producing a light sheet incident on the output optical fiber. As also indicated by the irradiance maps, in the VOA$_{SLT}$ (see figure 2(*c*)) considerably less light reaches the bottom part of the output fiber optics, whereas with the VOA$_{IJP}$ (see figure 2(*d*)), the light sheet intensity presents a more uniform profile. The main reason for this distinct behavior is the distribution of the magnetic material inside the cantilever in the different configurations. The U-shaped microchannel that orthogonally intersects the optical axis was designed to be $50\,\mu$m in height (as compared to the total thickness of the VOA, being $250\,\mu$m). In the VOA$_{SLT}$, this microchannel is filled with an M-SSM, forming a stripe which has a higher extinction coefficient than non-doped PDMS. As a result, there is a spatially defined region on this VOA where light absorption occurs. Conversely, in the VOA$_{IJP}$, the microchannel is filled with the non-doped PDMS and the FF droplets are placed between the air mirrors and the cantilever lateral facets (outside the optical axis). Thus, there

is no interaction between the confined light and the M-SSM. Finally, from these simulations, the intrinsic optical losses were numerically obtained, which will be compared with the experimental results in the characterization section.

2.3. Fabrication

The fabrication steps required for defining both VOAs are based on replica molding [27] using a two-level master. Even though this technique is broadly known, for completeness, some key points are reproduced here. Details of the fabrication can be found elsewhere [28].

2.3.1. VOA$_{SLT}$. The fabrication process starts by spinning a $50\,\mu$m-thick SU-8 layer over a $700\,\mu$m-thick soda-lime glass. Then, the wafer is soft baked (SB) on a hot plate for 2 h at 95 ℃. After that, the wafer is exposed to UV light using the first mask for defining both reservoirs and the U-shaped microchannel, followed by a post-exposure bake (PEB) for 20 min at 95 ℃. Then, a second layer of SU-8 is spin coated. An SB for 2 h at 95 ℃ precedes a third spinning step with identical conditions and the last SB is for 3 h at 95 ℃. Subsequently, the wafer is again exposed to UV light using the
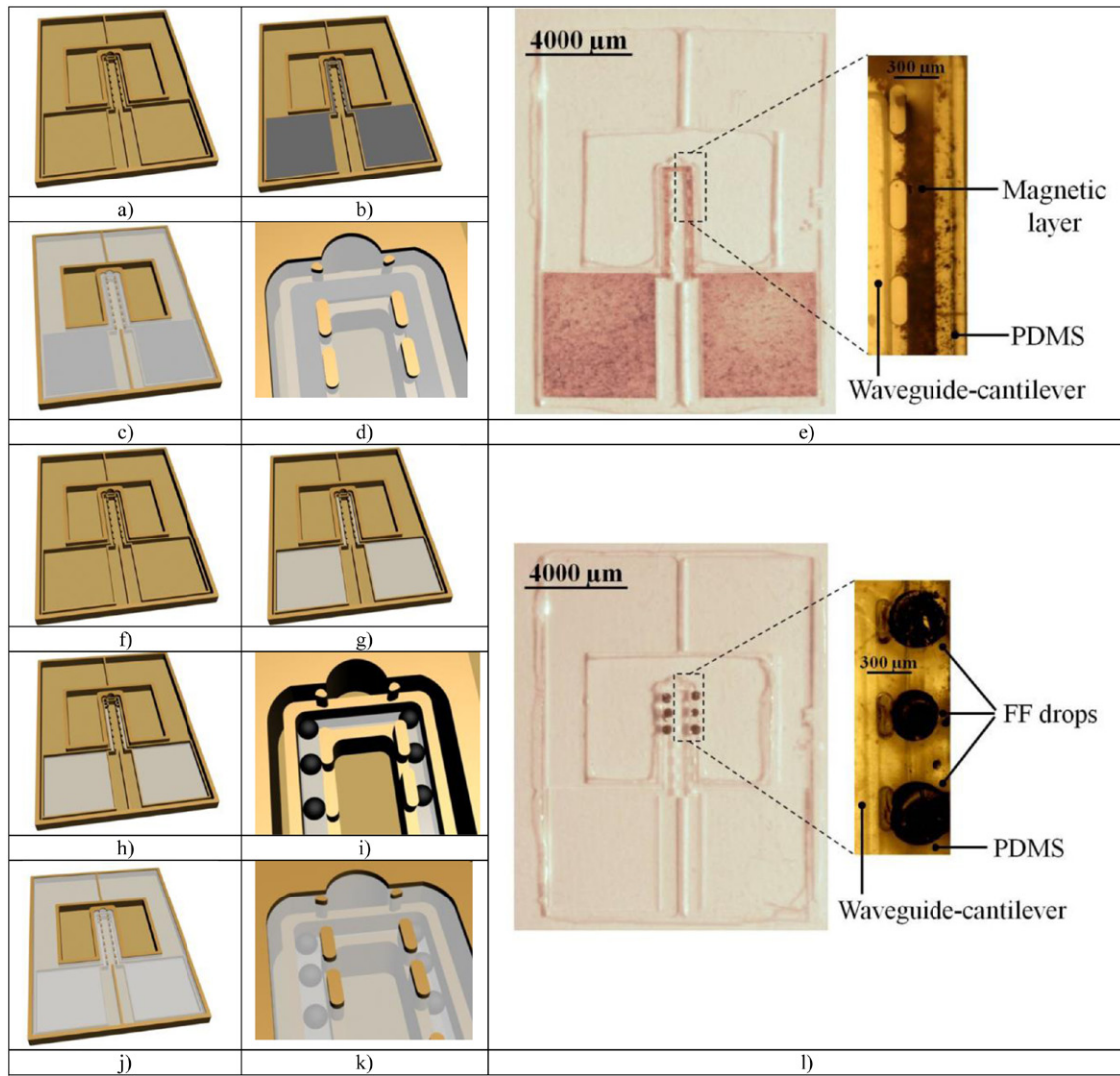
Figure 3. Scheme of the fabrication process starting with the definition of (*a*) the SU-8 master, followed by the VOA implementation. For the VOA$_{SLT}$, the M-SSM pre-polymer is poured into the master (*b*). Then, the non-doped PDMS pre-polymer is also poured into the master, forming a bilayer (*c*). (*d*) Shows a detail of the two layers in the master, and (*e*) a picture of the VOA$_{SLT}$ after being peeled off from the master, with a detail of the two pre-polymer layers. For the VOA$_{IJP}$ the fabrication starts with (*f*) the same master as for the VOA$_{SLT}$, (*g*) the non-doped PDMS polymer fills the first layer of the master, followed by (*h*) defining the FF droplets by IJP (*i*) specifically in the area close to the end of the waveguide-cantilever. (*j*) A second layer of non-doped PDMS pre-polymer is poured to entrap the FF droplets (*k*). The fabricated VOA$_{IJP}$ is peeled off from the master, an image of which is presented in (*l*) with a detail of the trapped FF droplets at the end of the waveguide-cantilevers.

second mask, which defines the opto-mechanical structures. The PEB for 15 min at 95 °C and the development of the structure using PGMEA finishes the fabrication of the master, as shown in figure 3(*a*).

The PDMS pre-polymer solution is prepared by mixing the elastomer and the curing agent in 10:1 ratio (v:v). To obtain the M-SSM, different weight percentages of FF (14.9 wt%, 22.8 wt% and 29.9 wt%) are added to the pre-polymer mixture, which is manually stirred until homogeneous dispersion is achieved. This subsequent mixture is degassed to remove the air bubbles and is used via standard SLT [28].

The M-SSM pre-polymer is poured into one reservoir. Then the U-microchannel is filled by capillarity. Overflow is avoided due the hydrophobic behavior of the master and the careful dispensing of the M-SSM. The material is added

until the second reservoir is completely filled (see figure 3(*b*)), followed by a pre-curing step for 5 min at 80 °C. After that, the second level of the master is filled with a non-doped PDMS pre-polymer, figure 3(*c*) and cured for 20 min at 80 °C. Figure 3(*d*) shows a detailed image where the M-SSM and non-doped PDMS layers in the master can be observed. Once polymerized, the fabricated structures are peeled off from the master. A picture of the final VOA$_{SLT}$ is shown in figure 3(*e*). The inset provides a detailed view, showing the magnetic stripe and the air mirrors.

2.3.2. VOA$_{IJP}$. The VOA$_{IJP}$ fabrication also uses the SLT master, as shown in figure 3(*f*). However, in this case, the first level of the master is filled with the non-doped PDMS pre-polymer (see figure 3(*g*)) and it is partially cured for 5 min at
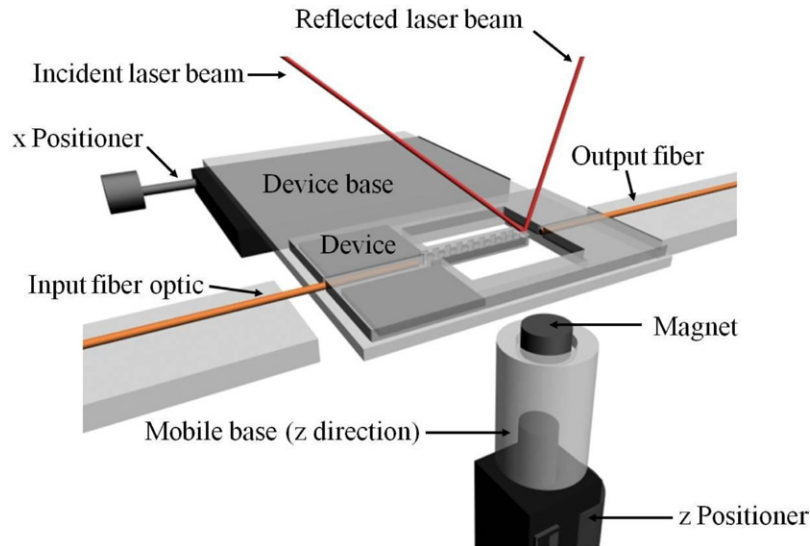
Figure 4. Experimental setup, including the necessary elements for mechanical (x positioner and the laser focalized at the end of the waveguide-cantilever) and optical characterization (input/output fiber optics and laser beam).

80 °C. After that, the FF droplets are dispensed by IJP with total FF volumes of $0.01\,\mu l$, $0.13\,\mu l$ and $0.15\,\mu l$. These volumes are divided between six spots in each structure with a total number of 600, 822 and 900 FF drops corresponding to 14.8 wt%, 20.4 wt% and 22.3 wt% of FF, respectively. The droplets are located in the area outside the optical axis and are close both to the lateral facets and the waveguide-cantilever end, figure 3(*h*). This area was selected as it provides the highest sensitivity against magnetic actuation (see figure 3(*i*)). Then, the second level is filled again with a non-doped PDMS pre-polymer layer (see figure 3(*j*)) and cured for 20 min at 80 °C. There by, with this strategy, the FF droplets remain trapped in the PDMS host matrix, figure 3(*k*). Finally, the fabricated VOA_{IJP} is peeled off the master. Figure 3(*l*) shows an image of these structures, where a detail of the FF droplets can be observed at the end of the waveguide-cantilever.

2.4. Characterization

2.4.1. Mechanical characterization. TEM: Structural homogeneity was determined using images from transmission electron microscopy (TEM), which were obtained using the system JEOL 2011, Jeol Ltd, USA. The distribution and size of the Fe_3O_4 nanoparticles included in the M-SSE were analyzed. From these images, 10 fields, each containing between 20-100 MNP depending on the sample, were analyzed using image software (ImageJ, USA).

Deflection: This section includes the measurement of deflection for both the VOA_{SLT} and VOA_{IJP} considering the different FF volumes. To perform such a characterization, the VOAs are placed over a NdFeB magnet (figure 4), with dimensions of 10 mm in diameter and 5 mm thick. This magnet is located on a positioning stage able to move vertically, thereby changing the applied magnetic field (B_{app}) as a function of the distance between the VOA and the magnet (d). B_{app} is measured with a Gaussmeter probe (475 DSP, Lake

Shore Cryotronics, Inc., USA). To measure the deflection as a function of B_{app}, a configuration similar to an atomic force microscope (AFM) is used. A laser beam (laser source, 633 nm, 10 mW, model 1137P, JDS Uniphase, USA) is focused on the free end waveguide-cantilever both with and without an applied magnetic field. With $B_{app} \neq 0$, the spot of the reflected beam has a measurable variation in its position due to a vertical displacement of the cantilever. In this case, to assure that the laser is focused on the free end of the waveguide-cantilever, an x-micropositioner is located underneath the VOA. Under these conditions vertical deflections (Δy_{max}) can be measured as a function of B_{app} for the three cantilever lengths and for the different FF concentrations.

2.4.2. Optical properties. The optical losses as a function of the B_{app} are also measured. Both the VOA_{SLT} and VOA_{IJP} are placed on the experimental setup, as shown in figure 4. A second connectorized laser (Laser source, 635 nm, 2.5 mW, Model S1FC, Thorlabs GmbH, USA) is used to couple the light into a multimode fiber optic with a core diameter of $105\,\mu m$ (Thorlabs GmbH, USA), located in the input self-alignment system, inherently aligned with the waveguide-cantilever. The output fiber optics with a core diameter of $200\,\mu m$ (Thorlabs GmbH, USA) is placed in the output self-alignment system, connected to a power meter (Newport Power Meter, Model 1930F-SL, Irvine, USA). With no applied magnetic field ($B_{app} = 0$), there is no misalignment between the waveguide-cantilever and the collecting fiber optics and therefore, the intrinsic optical losses can be measured. These losses not only include insertion losses, but also attenuation due to scattering at the waveguide and Fresnel reflections that occurs at each interface. Even though these losses can be considered as significant (as will be discussed in section 3.2), they do not depend on the actuation and therefore they are considered as background.

As the actuation is applied (i.e. as the applied magnetic field increases), a progressive deflection of the waveguide-cantilever
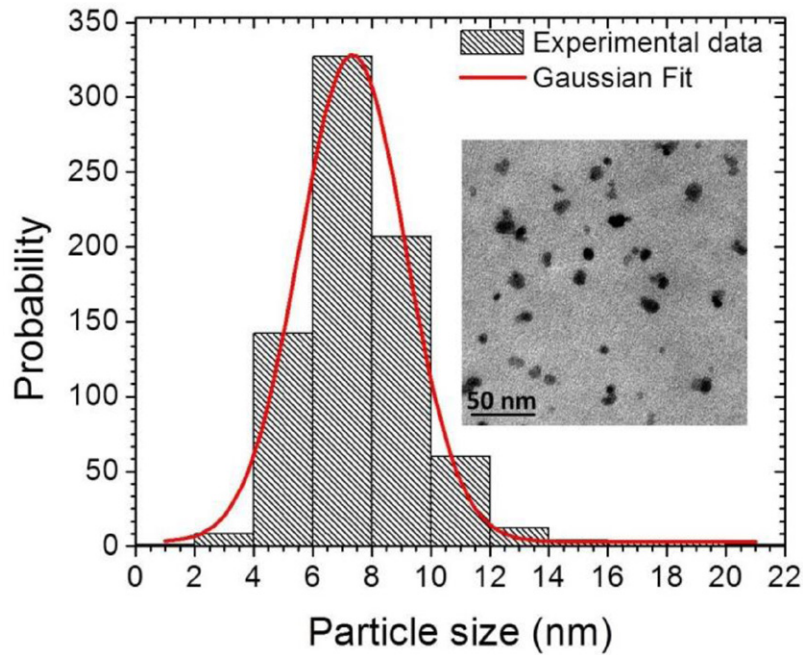
Figure 5. Nanoparticle size distribution using TEM image analysis and the Gaussian fitting for the highest FF concentration. The inset corresponds to the TEM images after polymerization, where the black scale bar corresponds to 50 nm.

is observed. This results in an increase in the coupling losses between the waveguide-cantilever and the output fiber optics (hereafter labeled actuation losses). This latter magnitude, dependent on B_{app}, is the optical parameter which will be studied in the proposed VOAs.

3. Results and discussion

3.1. Mechanical characterization

Structural material properties: Slab samples with the highest FF concentration are used for the image analysis to calculate and compare the average particle diameter. A histogram illustrating nanoparticle size distribution is presented in figure 5, together with a representative TEM image (inset). The Gaussian fit on the TEM results shows a single peak with both samples, which can be associated with a single particle size with a mean size of 7 ± 4 nm. From this can be seen the absence of aggregates, as well as the homogenous distribution of the MNPs on the polymeric matrix, as already presented by other authors [31]

The first step in this subsection is to validate the actuation principle of the proposed VOAs fabricated using the SLT and IJP strategies. To this effect, two microsystems with identical lengths ($l = 5000 \mu$m) and similar FF contents (14.9 wt% and 14.8 wt% for the SLT and IJP, respectively) were placed on the experimental setup and lateral pictures were taken. It can be seen how, for both technologies, there is no deflection in the absence of an applied magnetic field, $B_{app} = 0$ kG (figures 6(*a*) and 6(*c*)) for the SLT and IJP, respectively), confirming that the fabrication presented here provides with stress-free VOAs. When $B_{app} = 0.9$ kG, both the VOAs (see figures 6(*b*) and 6(*d*)) for the SLT and IJP, respectively, show the expected vertical displacement, validating its magnetic actuation.

Once the VOA working principle has been demonstrated, the next step is to obtain quantitative data regarding its actuation. To this effect, the setup described in section 2.4.1 is used to measure the deflection, Δy, as a function of B_{app} for VOA$_{SLT}$ (figure 7(*a*)) and VOA$_{IJP}$ (figure 7(*b*)). The inset in figure 7 (*a*) also shows the measured B_{app} as a function of d. The deflections are measured for all the VOAs under study, namely the three FF concentrations and the three waveguide-cantilever lengths for each fabrication strategy, providing a total of 18 measured microsystems. In both the SLT and IJP, the deflection increases with B_{app} until a quasi-saturation regime is reached (which has been measured to be between 0.29–0.57 kG, depending on the specific VOA strategy, length and wt% FF). As expected, larger deflections are obtained when increasing the wt% of FF in both the VOAs. Furthermore, when the SLT and IJP technologies are compared, larger deflections are obtained for VOA$_{IJP}$ containing a similar FF concentration. These results can be associated with the different FF distributions between both strategies. For VOA$_{SLT}$, the FF is homogeneously dispersed in the M-SSM, which in turn is distributed along the waveguide-cantilever's length. For VOA$_{IJP}$, the FF droplets are dispensed at the free end of the cantilever, making the latter structure more sensitive to B_{app}. Thus, with fewer loads and a strategic positioning of FF, a higher response at a specific B_{app} can be obtained.

3.2. Optical characterization

To determine the intrinsic optical losses, VOAs with the same length ($l = 4000 \mu$m) are measured with no applied magnetic field, $B_{app} = 0$ kG. Both the numerical and experimental values are summarized in table 1. Previous results have shown that the extinction coefficient of the M-SSM increases with the FF concentration. Thus, the light propagating at the bottom
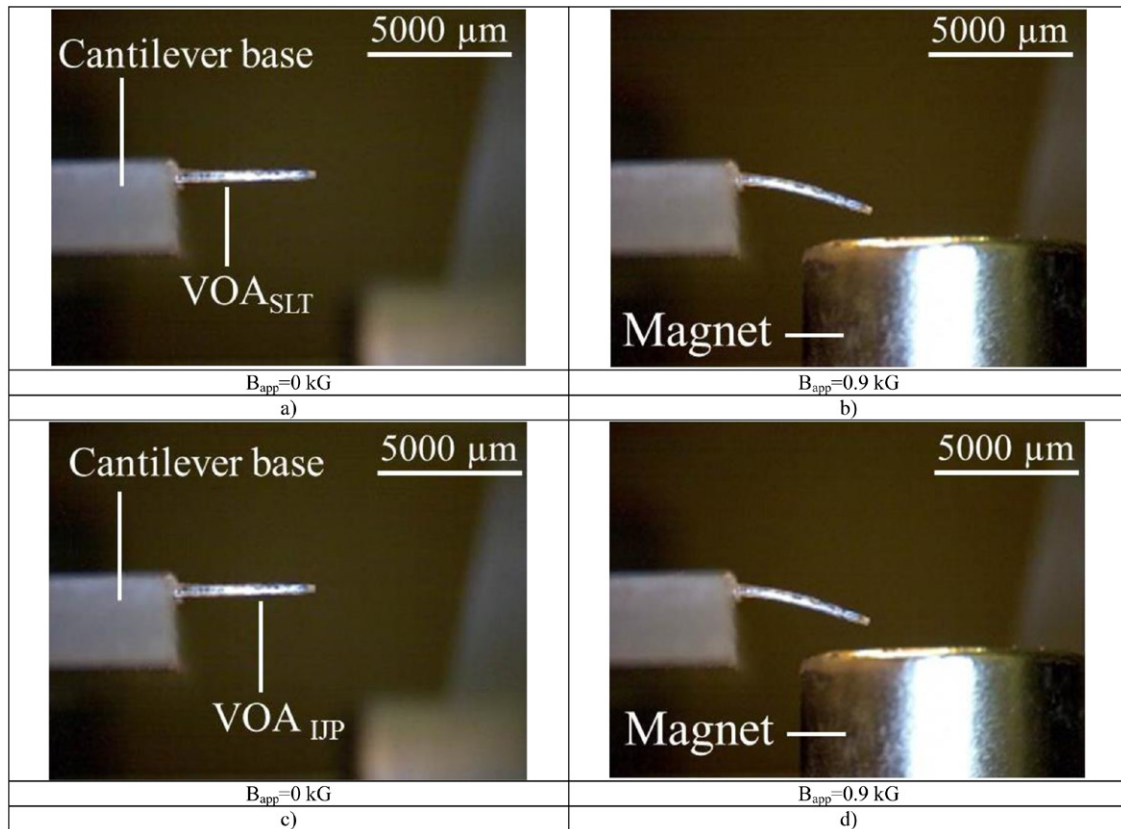
Figure 6. Images with a waveguide-cantilever length of l = 5000 μm for VOA$_{SLT}$ for a 14.9 wt% of FF with (*a*) B$_{app}$ = 0 kG and (*b*) B$_{app}$ = 0.9 kG. VOA$_{IJP}$ at 14.8 wt% of FF with (*c*) B$_{app}$ = 0 kG and (*d*) B$_{app}$ = 0.9 kG.

part of the waveguide-cantilever is coupled to the M-SSM stripe, where it is partially absorbed. As a result, for VOA$_{SLT}$ the intrinsic optical losses increase with the FF concentration. Conversely, for the VOA$_{IJP}$ both the numerical and experimental intrinsic optical losses are independent of the FF concentration. These results are expected, since in this structure the FF is positioned outside the optical axis and therefore there is no light M-SSM interaction. In this latter configuration, lower intrinsic losses are obtained, thus improving the performance of the proposed VOAs.

It is also important to mention that there is a small, but noticeable difference between the numerically and experimentally obtained intrinsic optical losses in both the SLT and IJP strategies. This difference may be associated with fabrication defects, scattering centers (dust) at the waveguide-cantilever and/or the suboptimal positioning of the output fiber optics. However, the experimental values of the intrinsic optical losses follow the behavior predicted by the numerical results, thus validating the use of IJP proposed in this work.

When comparing these results with previously reported works, it can be seen how Chang–Yen *et al* obtained intrinsic optical losses close to 17 dB [33]. Moreover, in the work presented by Cadarso *et al* [34] the intrinsic losses were measured to be 5.1 dB for a cantilever-based PDMS MOEMS with a geometry of 500 × 250 × 2400 μm (width × height × length, respectively). In our case, in the worst configuration corresponding to the highest FF concentration for VOA$_{SLT}$ with 29.9 wt% FF, this magnitude has been measured to be below

10 dB. Conversely, for the case of 22.2 wt% and VOA$_{IJP}$, the value is 5.1 dB. This value corresponds to a VOA geometry of 500 × 250 × 4000 μm (width × height × length, respectively). In both cases, the insertion losses were between 1 and 1.2 dB. Thus, the configuration proposed here provides clear advantages in terms of optical performance.

Once the intrinsic optical losses are measured, the actuation losses as a function of B$_{app}$ for all the VOA configurations are obtained. The results are presented in figures 8(*a*)) and (*b*), respectively. In agreement with the mechanical characterization, the actuation losses also increase with B$_{app}$, reaching values close to saturation. As a rule, for any given technology, the higher the FF concentration, the higher the actuation losses. Comparing both technologies, it can be seen that VOA$_{IJP}$ always presents higher actuation losses for a similar FF concentration (being 16.1 dB and 18.9 dB for the VOA$_{SLT}$ and VOA$_{IJP}$, respectively). Hence, it can be concluded that with the IJP technique, MOEMS with higher actuation losses can be obtained if the FF is located at the cantilever tip.

3.3. Comparison between the VOA$_{SLT}$ and VOA$_{IJP}$ configurations

In order to have a valid mechanical and optical comparison mechanism between both fabrication strategies, it becomes necessary to define two parameters which take into account the slightly different wt% of the FF in each fabricated VOA. Here, for a mechanical comparison, we have defined β as

a)

b)
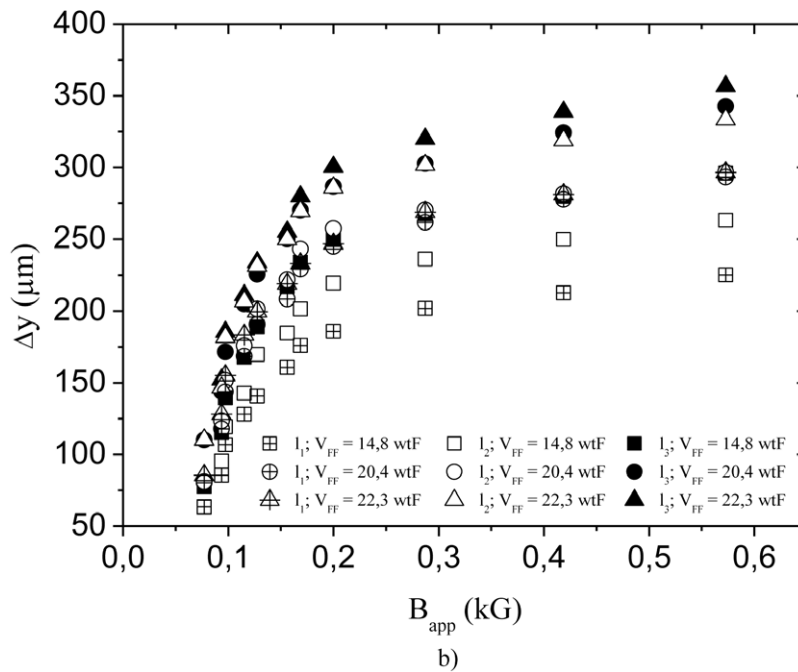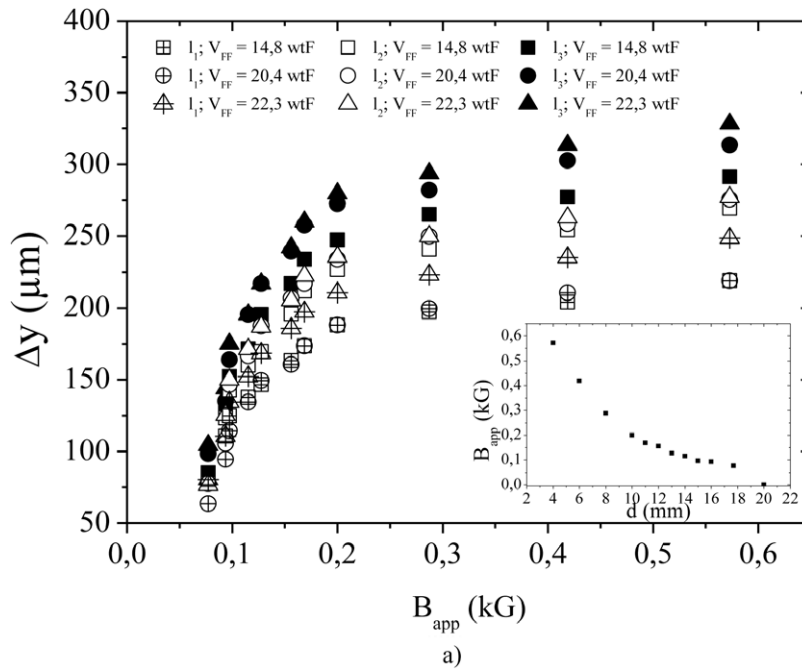
Figure 7. (*a*) Deflections for VOA$_{SLT}$ and (*b*) VOA$_{IJP}$ as a function of the applied magnetic field (B$_{app}$), for three different lengths l$_1$ = 4000 μm, l$_2$ = 5000 μm and l$_3$ = 6000 μm. The weight percentages of the FF are 14.9 wt%, 22.8 wt% and 29.9 wt% for the case of VOA$_{SLT}$ and 14.8 wt%, 20.4 wt% and 22.3 wt% for the VOA$_{IJP}$. Experimental errors are below 5% (error bars not shown for ease of reading).

Table 1. The numerical and experimental data for the intrinsic optical losses at different wt% for VOA$_{SLT}$ and VOA$_{IJP}$ for l = 4000 μm.

Wt%FF VOA$_{SLT}$	Intrinsic optical losses VOA$_{SLT}$ (dB)		Intrinsic optical losses VOA$_{IJP}$ (dB)		Wt% FF VOA$_{IJP}$
	Simulated	Experimental	Simulated	Experimental	
14.9	7.5	9.0 ± *0.1*	4.6	5.1 ± *0.1*	14.8
22.8	7.7	9.1 ± *0.2*	4.6	5.4 ± *0.1*	20.4
29.9	8.0	9.8 ± *0.2*	4.6	5.1 ± *0.1*	22.3
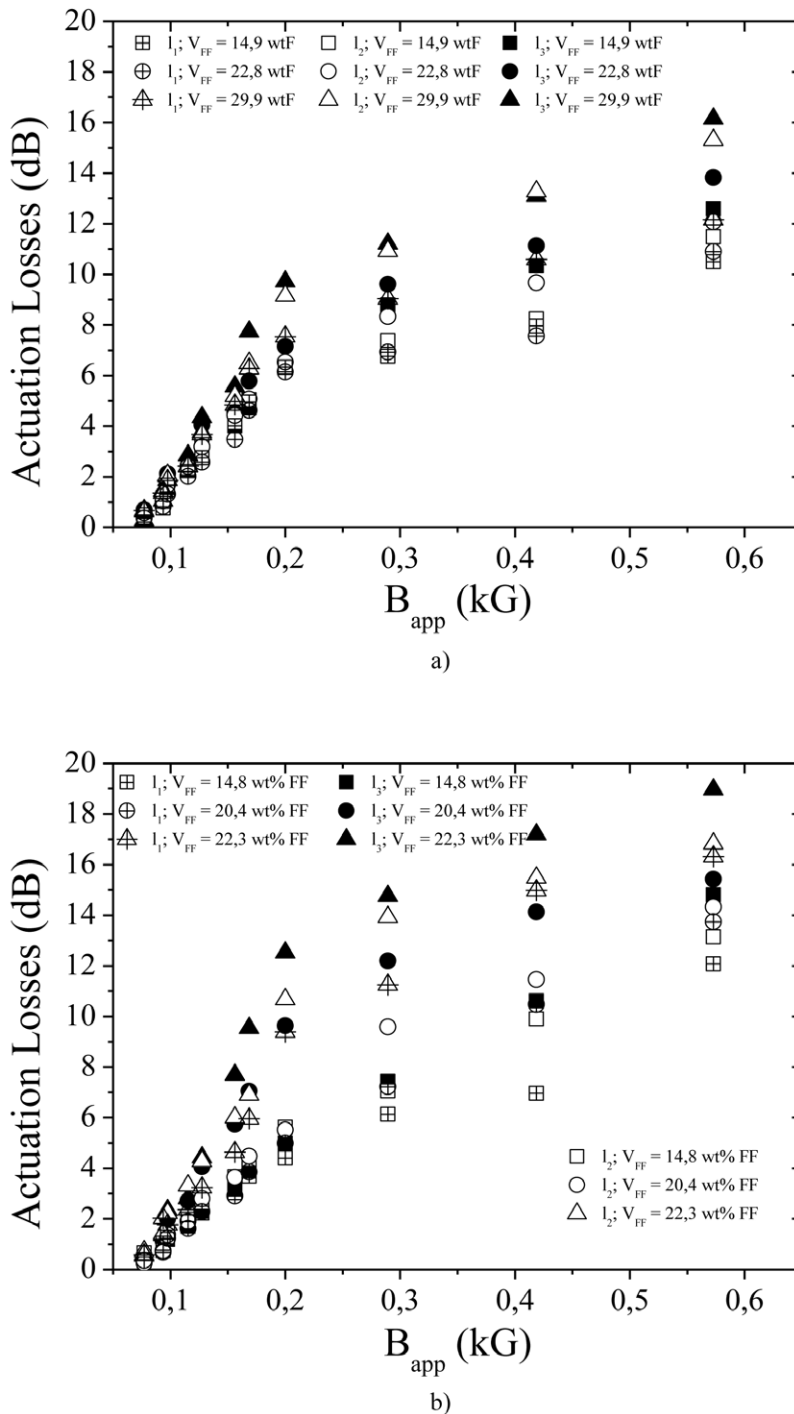
Figure 8. (*a*) Actuation losses for the VOA$_{SLT}$ and (*b*) VOA$_{IJP}$ as a function of the applied magnetic field (B$_{app}$) and the VOA, for three different lengths l$_1$ = 4000 μm, l$_2$ = 5000 μm and l$_3$ = 6000 μm. The weight percentages of the FF are 14.9 wt%, 22.8 wt% and 29.9 wt% for the VOA$_{SLT}$ and 14.8 wt%, 20.4 wt% and 22.3 wt% for the VOA$_{IJP}$. Experimental errors are below 5% (error bars not shown for ease of reading).

the ratio between the maximum deflection (Δy$_{max}$) and the wt% of FF. Maximum deflection is the difference between the deflection corresponding to B$_{app}$ = 0 and B$_{app}$ = 0.57 kG. These measurements are taken from figure 7. Analogously, the ratio between the maximum actuation losses measured in figure 8 and the wt% of FF, named η, is also used. The results of these parameters are shown in figure 9. As can be seen, for all waveguide-cantilever lengths, the VOA$_{IJP}$ approach has

both a higher β and η compared to the VOA$_{SLT}$. One plausible explanation for this behavior might be associated with the mechanical properties of the M-SSM. As previously discussed, even when considering that the contribution of the M-SSM to the overall Y of the cantilever is at the highest 12.5% it is also important to identify that, as the quantity of FF increases in the PDMS matrix, the Y of the M-SSM increases, obtaining a more rigid VOA$_{SLT}$ which exhibits a smaller deflection on a

Figure 9. β and η as a function of the waveguide-cantilever lengths (4000 μm, 5000 μm, and 6000 μm) for 29.9 wt% of FF and for 22.3 wt% of FF in the case of VOA$_{SLT}$ and VOA$_{IJP}$, respectively. Experimental errors are below 5% (error bars not shown for ease of reading).

Table 2. Summary of the experimental data obtained from the mechanical and optical characterization: Maximum deflection (Δy_{max}), actuation losses for both VOA$_{SLT}$ and VOA$_{IJP}$ with different ferrofluid concentration.

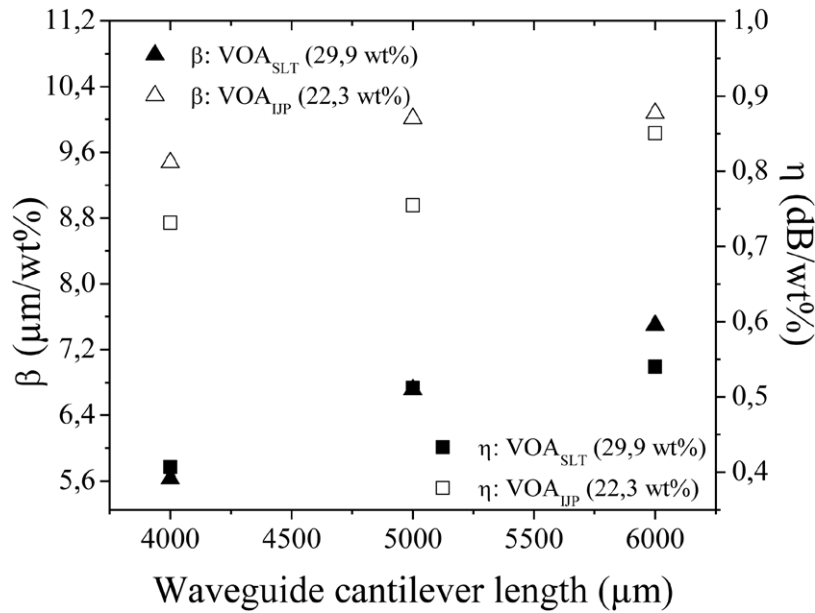|	VOA$_{SLT}$			VOA$_{IJP}$			
Wt%FF	14.9	22.8	29.9	14.8	20.4	22.3	1 (μm)
Δy_{max} (μm)	140	160	170	160	210	210	4000
	190	200	210	190	220	220	5000
	210	220	220	220	230	250	6000
Actuation	10.5	10.9	12.1	12.1	13.7	16.3	4000
Losses (dB)	11.5	12.1	12.5	13.1	14.3	16.8	5000
	12.6	13.8	16.1	14.8	15.4	18.9	6000

given magnetic actuation [35]. Conversely, in the IJP strategy, small FF volumes are localized in precise positions at the end of the free waveguide-cantilever, whereby it can be assumed that the Y does not vary significantly.

Table 2 summarizes the results presented in this work. It can be observed how the performance of the VOA presented here is improved when, instead of defining a microchannel filled with M-SSM, the FF droplets are trapped at the end of the waveguide-cantilever in a clean PDMS matrix. This increase in mechanical behavior also assures higher actuation losses.

When comparing the results obtained here with those reported previously, it can be seen that Yang *et al* [24] presented actuation losses close to 6 dB. This magnitude increased until 7 dB in [36] and to the best of our knowledge, only those obtained in [37] allowed 40 dB, but using a highly fragile, electromagnetic-based flapping mirror. Thus, the MOEMS-VOA presented here are good candidates for light power control in (bio)chemical and biological applications. This is confirmed by the fact that PDMS, the main constituent of the MOEMS-VOA has a high transmittance in

the UV-NIR range, is mechanically robust and is a biocompatible material.

4. Conclusions

The magnetically-actuated MOEMS-VOA obtained by using two different technologies (soft lithography, SLT and ink-jet printing, IJP) have been presented and compared in this work. Polydimethylsiloxane (PDMS) has been selected as the polymeric host matrix which traps the magnetic filler in the form of a ferrofluid (FF). Both configurations have a common geometry consisting of a waveguide-cantilever and two alignment channels for positioning both the input and the output fiber optics. For SLT, different weight fractions of FF (14.9 wt %, 22.8 wt % and 29.9 wt %) have been incorporated into the PDMS. The TEM measurements confirm a homogeneous magnetic sensitive stimuli material (M-SSM), which has been used for defining magnetic stripes on the bottom side of the waveguide-cantilever included in the VOA$_{SLT}$. By using IJP, a total amount of FF corresponding to 14.8 wt%, 20.4 wt% and 22.3 wt% of FF has been trapped between two non-doped PDMS layers at the waveguide-cantilever tip (outside the optical path), resulting in the VOA$_{IJP}$. Without actuation, the intrinsic optical losses have been measured to be between 9.0 ± 0.1 dB and 9.8 ± 0.2 dB for the VOA$_{SLT}$, whereas for the VOA$_{IJP}$ these figures are between 5.1 ± 0.1 dB and 5.4 ± 0.1 dB. This is in agreement with the fact that only in the VOA$_{SLT}$ does light interact with the M-SSM. In both strategies, deflection increases with B$_{app}$ until a quasi-saturation regime is reached (0.29–0.57 kG). When comparing VOAs with a similar wt% of FF, larger deflections and higher actuation losses are always obtained for VOA$_{IJP}$ than for VOA$_{SLT}$. Due to the small differences in the FF concentrations between both the technologies, two different parameters, labelled β and

η, have been defined. For the three lengths studied and the two different FF concentrations (22.8 wt% of FF and 20.4 wt% of FF for the SLT and IJP strategies, respectively), it has been demonstrated that VOA$_{IJP}$ presents lower intrinsic optical losses, as well as a higher β and η, than the VOA$_{SLT}$. Thus, the here labelled IJP technology has been demonstrated to be a valid technique for improving performance, not only with the VOAs presented here, but in general for MOEMS (or even MEMS) using M-SSMs.

Acknowledgments

References

[1] Padgaonkar A J, Krieger K W and King A I 1975 Measurement of angular acceleration of a rigid body using linear accelerometers *J. Appl. Mech.* **42** 552–6

[2] Brown E R 1998 RF-MEMS switches for reconfigurable integrated circuits *IEEE Trans. Microw. Theory Tech.* **46** 1868–80

[3] Mitcheson P D, Green T C, Yeatman E M and Holmes A S 2004 Architectures for vibration-driven micropower generators *J. Microelectromech. Syst.* **13** 429–40

[4] Guan T, Keulemans G, Ceyssens F and Puers R 2013 MOEMS uniaxial accelerometer based on EpoClad/EpoCore photoresists with built-in fiber clamp *Sensors Actuators* A **193** 95–102

[5] Liu C 2007 Recent developments in polymer MEMS *Adv. Mater.* **19** 3783–90

[6] Liu F and Urban M W 2010 Recent advances and challenges in designing stimuli-responsive polymers *Prog. Polym. Sci.* **35** 3–23

[7] Kristensen A, Boisen A, Fuard D, Tzvetkova-Chevolleau T, Decossas S, Tracqui P and Schiavone P 2008 Optimization of poly-di-methyl-siloxane (PDMS) substrates for studying cellular adhesion and motility *Microelectron. Eng.* **85** 1289–93

[8] Llobera A, Cadarso V J, Zinoviev K, Dominguez C, Buttgenbach S, Vila J, Plaza J A and Biittgenbach S 2009 Poly(Dimethylsiloxane) waveguide cantilevers for Optomechanical sensing *IEEE Photon. Technol. Lett.* **21** 79–81

[9] Bélanger M C and Marois Y 2001 Hemocompatibility, biocompatibility, inflammatory and in vivo studies of primary reference materials low-density polyethylene and polydimethylsiloxane: a review *J. Biomed. Mater. Res.* **58** 467–77

[10] Jackson W C, Tran H D, O'Brien M J, Rabinovich E and Lopez G P 2001 Rapid prototyping of active microfluidic components based on magnetically modified elastomeric materials *J. Vac. Sci. Technol.* B **19** 596

[11] Odenbach S 2003 Ferrofluids—magnetically controlled suspensions *Colloids Surf. A Physicochem. Eng. Asp.* **217** 171–8

[12] Pankhurst Q A, Connolly J, Jones S K and Dobson J 2003 Applications of magnetic nanoparticles in biomedicine *J. Phys. D: Appl. Phys.* **36** R167–81

[13] Pirmoradi F, Cheng L and Chiao M 2010 A magnetic poly(dimethylesiloxane) composite membrane incorporated with uniformly dispersed, coated iron oxide nanoparticles *J. Micromech. Microeng.* **20** 015032

[14] Filipcsei G and Zrínyi M 2010 Magnetodeformation effects and the swelling of ferrogels in a uniform magnetic field *J. Phys.: Condens. Matter* **22** 276001

[15] Koh K H, Lee C and Kobayashi T 2010 A piezoelectric-driven 3D MEMS VOA using attenuation mechanism with combination of rotational and translational effects *J. Microelectromech. Syst.* **19** 1370–9

[16] Suster M, Guo J, Chaimanonart N, Ko W H and Young D J 2006 A high-performance MEMS capacitive strain sensing system *J. Microelectromech. Syst.* **15** 1069–77

[17] Llobera A, Seidemann V, Plaza J A, Cadarso V J and Buttgenbach S 2007 SU-8 Optical accelerometers *J. Microelectromech. Syst.* **16** 111–121

[18] Lee C 2006 MOEMS variable optical attenuator with improved dynamic characteristics based on robust design *IEEE Photon. Technol. Lett.* **18** 773–5

[19] Lee C and Yeh J A 2008 Development and evolution of MOEMS technology in variable optical attenuators *J. Micro Nanolithogr. MEMS MOEMS* **7** 021003

[20] Li L J, Zawadzka J and Uttamchandani D 2004 Integrated self-assembling and holding technique applied to a 3D MEMS variable optical attenuator *J. Microelectromech. Syst.* **13** 83–90

[21] Puyol M, Salinas I, Garcés I, Villuendas F, Llobera A, Domínguez C and Alonso J 2002 Improved integrated waveguide absorbance optodes for ion-selective sensing *Anal. Chem.* **74** 3354–61

[22] Llobera A, Villanueva G, Cadarso V J, Battgenbach S and Plaza J A 2006 Polymeric MOEMS variable optical attenuator *IEEE Photon. Technol. Lett.* **18** 2425–7

[23] Miao Y, Zhang K, Liu B, Lin W, Zhang H, Lu Y and Yao J 2013 Ferrofluid-infiltrated microstructured optical fiber long-period grating *IEEE Photon. Technol. Lett.* 306–9

[24] Yang X, Liu Y, Zheng Y, Li S, Yuan L, Yuan T and Tong C 2013 A capillary optical fiber modulator derivates from magnetic fluid *Opt. Commun.* **304** 83–6

[25] Ozturk A, Ocakli H I, Ozber N, Urey H, Kavaki I H and Alaca B E 2008 A magnetically actuated resonant mass sensor with integrated optical readout *Photon. Technol. Lett.* **20** 1905–7

[26] de Pedro S, Cadarso V J, Munoz-Berbel X, Plaza J A, Sort J, Brugger J, Buttgenbach S and Llobera A 2013 Magnetically-actuated variable optical attenuators using ferrofluid-doped elastomer implemented by combination of soft lithography and inkjet printing technologies *Proc. IEEE 26th Int. Conf. on Micro Electro Mechanical Systems (MEMS)* (*Taipei, Jan. 2013*) pp 548–51

[27] Xia Y and Whitesides G M 1998 Soft lithography *Angew. Chem. Int. Edn* **37** 550–75

[28] Vila-Planas J, Fernández-Rosas E, Ibarlucea B, Demming S, Nogués C, Plaza J A, Domínguez C, Büttgenbach S and Llobera A 2011 Cell analysis using a multiple internal reflection photonic lab-on-a-chip *Nat. Protoc.* **6** 1642–55

[29] Camp P and Patey G 2000 Structure and scattering in colloidal ferrofluids *Phys. Rev.* E **62** 5403–8

[30] Llobera A, Wilke R and Büttgenbach S 2008 Enhancement of the response of poly(dimethylsiloxane) hollow prisms through air mirrors for absorbance-based sensing *Talanta* **75** 473–9

[31] Evans B A, Fiser B L, Prins W J, Rapp D J, Shields A R, Glass D R and Superfine R 2012 A highly tunable silicone-based magnetic elastomer with nanoscale homogeneity *J. Magn. Magn. Mater.* **324** 501–7

[32] Bosch S, Ferré-Borrull J, Leinfellner N and Canillas A 2000 Effective dielectric function of mixtures of three or more materials: a numerical procedure for computations *Surf. Sci.* **453** 9–17

[33] Chang-Yen D A, Eich R K and Gale B K 2005 A monolithic PDMS waveguide system fabricated using soft-lithography techniques *J. Light. Technol.* **23** 2088–93

[34] Cadarso V J, Plaza J A, Zinoviev K, Dominguez C, de Pedro S, Buttgenbach S and Llobera A 2009 Cantilever-based poly(dimethylsiloxane) microoptoelectromechanical systems *Proc. IEEE Sensors* (*Christchurch, Oct. 2009*) pp 413–7

[35] Denver H, Heiman T, Martin E, Gupta A and Borca-Tasciuc D A 2009 Fabrication of polydimethylsiloxane composites with nickel nanoparticlesand nanowire fillers and study of their mechanical and magnetic properites *J. Appl. Phys.* **106** 064909

[36] Choi H.Y, Han W and Cho Y H 2010 Low-power high-speed electromagnetic flapping shutters using trapezoidal shutter blades suspended by H-Type torsional springs *J. Microelectromech. Syst.* **19** 1422–9

[37] Hung S H, Hsieh H T and John Su G D 2008 An electro-magnetic micromachined actuator monolithically integrated with a vertical shutter for variable optical attenuation *J. Micromech. Microeng.* **18** 075003

Preparation and Characterization of Patternable Magnetic Stimulus Sensitive Elastomers Obtained from Mixtures of PDMS and Ferrofluid

S. de Pedro[a], X. Muñoz-Berbel[a], R. Rodríguez-Rodríguez[b], J. Sort[c], J. A. Plaza[a], E. Mendoza[d], J. Brugger[e], A. Llobera[a] and V.J. Cadarso[e,f]

[a.]Institut de Microelectrònica de Barcelona IMB-CNM (CSIC), Esfera UAB, Campus UAB, 08193 Bellaterra, Spain.

[b.]Department of Pharmacology, University of Sevilla, Profesor Garcia Gonzalez 2, 41012 Sevilla, Spain

[c.]Institució Catalana de Recerca i Estudis Avançats (ICREA) and Departament de Física, Universitat Autònoma de Barcelona, 08193 Bellaterra, Spain.

[d.]Grup de Nanomaterials Aplicats, Centre de Recerca en Nanoenginyeria, UPC, 08023 Barcelona, Spain.

[e.]Microsystems Laboratory, École Polytechnique Fédérale de Lausanne (EPFL), 1015 Lausanne, Switzerland.

[f.]Laboratory for Micro- and Nanotechnology, Paul Scherrer Institut (PSI), 5232 Villigen, Switzerland.

E-mail: Sandra.depedro@imb-cnm.csic.es

Abstract

Multi-functional materials incorporating many properties from different constituents are very attractive in several fields. We present a structural, optical, magnetic and mechanical characterization of several magnetic stimulus sensitive elastomers (M-SSEs) obtained by using polydimethylsiloxane (PDMS) and isoparafin-based ferrofluid (FF) containing Fe_3O_4 nanoparticles. Different FF concentrations up to a maximum of 24,6% have been used. The structural properties of the material demonstrate a homogenous distribution of the magnetic nanoparticles with a particle size of 8 nm ± 4 nm which does not vary with the FF concentration. The absorption coefficient (α) increases with the FF concentration. At the maximum concentration, the material is completely opaque with a α of 184,4 cm^{-1}. The M-SSE exhibits superparamagnetic behaviour with a maximum magnetization of 3,6 emu/g. Furthermore, the M-SSEs have been microstructured by soft lithography, obtaining cantilevers. These cantilevers have been used for measuring the Young's modulus for M-SSE (Y_{M-SSE}) ranging from 190 kPa to 1000 kPa with the FF concentration. The deflection in function of applied magnetic field has been also measured.

Keywords: PDMS; ferrofluid; magnetic actuators, magnetic sensitive elastomer, optical response,

1. Introduction

Last decades, material engineering has been focused on the development of mimic nature in designing multi-functional materials [1]. Such materials may have properties which change in response to external/internal variations of the environmental conditions (i.e. stimuli) [2]. Here, this type of materials is referred as functional materials can be sensitive to a large variety of stimuli, like changes in pH [3], temperature [4], electric fields [5] and/or magnetic fields [6]. As a result of these stimuli, a change in the material properties, which may be mechanical, optical, electrical or chemical properties, can be observed. These materials are known as sensitive stimuli materials (SSMs). Among the myriad of possible applications fields, they have been demonstrated to be a very promising strategy for biomedical applications. Specifically, drug delivery [7], biosensing/diagnostics [8], smarts films/matrices for tissue engineering [9] or the in situ construction of networks [10] are some of the reported examples for such materials.

An additional advantage of SSM for biomedical applications is the possibility to be used inside a living organism. In this context, the SSM should fulfil strict requirements in terms of biocompatibility, small size and operation reversibly (on/off transition). When including such material on a device, aspects such as accurate location in the biological area, controlled release (in case of drug delivery) at the precise required location or rapidly actuation/control over the event are only some examples of factors that also must be taken into account [11],[12].

Clearly, biocompatibility is the most important aspect that has to be taken into consideration with implantable bio-materials / bio-devices. Biocompatibility can be understood in many different ways. Firstly, from the point of view of chemical properties, materials with very low reactivity are preferred due to their inherent stability [12]. Secondly, the mechanical properties such as the Young's modulus (Y) are of interest because materials with a low Y may adapt more closely to the shape where the material/device has to be implanted, and offer less mechanical resistance in response to a stimulus. When considering doping (as will afterwards be discussed), working with materials in bulk allows the inclusion of additives while keeping them encapsulated inside the host material. Thus, if the material is mechanically and chemically stable, any possible ageing or degradation of the doping agent, which may provide with potentially toxic subproducts, is prevented. Finally, overall size in a device suitable to be implanted is a key aspect and therefore microfabrication techniques are preferred [13].

In that sense, for each application, the most appropriate SSM and its actuation principle has to be identified, designed, and implemented. Generally, such materials consist on a non-actuable matrix and an additive (doping agent) that confers to the material the required functionality. Ceramics, metals and polymers have been the most used materials for the development of SSMs [14]. Nevertheless, polymers have gaining attention since they offer outstanding advantages such as large responses (e.g. shrinkage, expansion, etc.) against an specific stimulus [15], light weight and low cost [16] while holding the microfabrication requirement. Here, the polymer plays the role of host matrix and is specifically selected depending on the given application (Young's modulus, biocompatibility, etc), whereas the additive is chosen considering the actuation principle (optical, electrical, magnetic, etc). Thereby, the resulting material has a combination of matrix and additives properties.

Among the different SSMs, those suitable to change their shape under external magnetic field stimulus [17] are preferred for in vivo applications because of their contactless actuation as well as its noninvasive, so is suitable for applications in biological processes [6], [18]. In this context, a combination of a polymeric matrix and magnetic additives provides with the so-called magnetic SSM (M-SSM) [19], [20], [7], [21], [22]. In all cases, the M-SSM response is directly related to the Y of the polymeric matrix and thus, polymers with low Y provide with higher performance against the same stimulus. Thereby, elastomers (and specially polydimethilsiloxane, PDMS) have become of interest for defining magnetic stimulus-sensitive elastomers (M-SSE), since it fulfils requirements such as biocompatibility [23], low Y, long thermo-chemical and structural stability [24], fabrication simplicity [25] and low cost [26] as well as other physical properties such as [27] high transmittance in the UV-NIR range [28].

The use of magnetic nanoparticles (MNPs) as additive in PDMS matrices for obtaining M-SSE has previously been reported [29], [30]. These materials show large tunability of their shape and mechanical behaviour as a function of the dispersion, distribution, morphology and loading of the MNPs [31]. M-SSEs with neither remanence or coercivity to an applied magnetic field (B_{app}) have been presented using MNPs with superparamagnetic behavior [32]. Such material can be found, for instance, in the work of F. N. Pirmoradi *et al.*, where they report a drug delivery device which is magnetic actuated for controlling drug release. In this example, M-SSE is obtained by mixing solid magnetic additives with the host matrix. This strategy is prone to form aggregates to reduce the energy associated with the high surface area to volume ratio of the nanosized particles [32] not only when included in PDMS, but more generally in any polymer matrix. Aggregates induce heterogeneities and an induce uneven functionality on the material, which results in poor performance, as could be unequal mechanical properties of the M-SSE [33]. Moreover, aggregates may drastically modify the optical properties of the polymeric matrix, increase the surface roughness, change the surface properties and hinder the bonding process [31], making the use of such material a challenge.

Homogenization of the additive within polymeric matrix is then necessary, and an alternative, successful strategy is the replacement of the commonly-used powder form of M-SSEs by MNPs homogeneously dispersed in carrier liquids [34]. Such stable colloidal form is generally known as ferrofluid (FF) and generally requires capping of the MNPs with a coating of the same polarity as carrier liquid [35]. Iron is one of the most used elements, which can lead to the formation of magnetite (Fe_3O_4) with diameter ranging between 3 nm and 15 nm and presenting either in superparamagnetic or single-domain state [36]. Because of its non-toxicity and non-carcinogenic properties as well as their resistance to oxidation , magnetite nanoparticles have broadly been used in biological applications, including cellular therapy [37], cellular targeting [38], tissue repair [39], drug delivery [40], magnetic resonance imagining (MRI) [41] and hyperthermia [42].

Even being an extremely promising material, the physical and biological properties (especially biocompatibility) of FF-based M-SSE have seldomly been jointly reported. In this work, we aim to tackle this issue by characterizing M-SSEs obtained using PDMS as host matrix and isoparafin-based FF containing Fe_3O_4 nanoparticles as additive. Different properties of M-SSE as a function of FF concentration are here presented. Firstly, the internal structure of

the M-SSE, i.e., the size particle, the aggregates-free formation and the homogeneous distribution has been studied by transmission electron microscopy (TEM). Then, the M-SSE has been both magnetic and optically characterized in bulk and mechanically characterized using cantilevers fabricated with soft lithography. Finally, the biocompatibility study of the M-SSE has been carried out. As a final example of application, the M-SSE has been used for defining biocompatible magnetic cantilevers.

2. Experimentals

2.1. Reagents

The negative-tone epoxy-based polymer SU-8 50 and its developer propylene glycol methyl ether acetate (PGMEA) (both from MicroChem, Corp., USA) were used following known recipes [28]. PDMS elastomer (Sylgard Silicon Elastomer 184, Dow Corning Corp., USA) was prepared in accordance to the datasheet. FF was used as provided the manufacturer (Liquids Research Limited, North Wales). The FF presents a uniform size distribution and low Fe_3O_4 particle agglomeration (< 20 nm) dispersed into isoparafin with 10 nm as the mean particle diameter and a saturation of 400 G.

2.2. Synthesis of magnetic sensitive stimuli elastomer (M-SSE)

M-SSE is synthesized by mixing PDMS and FF. First, the PDMS pre-polymer is obtained in a 1:10 (v:v) curing agent/base elastomer as available from the manufacturer. Just afterwards, different FF volumes are included (0 %, 1,7 %; 3,5 %; 9,8 %; 15,4 %; 20,3 % and 24,6 % in volume) and manually stirred until homogeneous dispersion is achieved. This mixture is then degassed to remove air bubbles. The resulting M-SSEs are labelled as S_i (i = 0, 1,..., 6; corresponding to the increasing FF concentrations).

2.3. Design and fabrication

The structural homogeneity, biocompatibility, optical transmittance and magnetization were studied in bulk using slab samples. M-SSEs Young's modulus was obtained by implementing cantilevers (as shown in Figure 1a and 1b) with dimensions 500 µm (width, w), 4400 µm (length, l) and 250 µm (thickness, h). The final geometry (Figure 1c and 1d) consisted of a cantilever having a rectangular seismic mass (with dimensions w, l, h, in µm being of 1600, 2500, 250) at the tip to enhance the response against the external magnetic field

The cantilevers and slab samples are fabricated by soft-lithography technology [43]. The process starts using a soda-lime wafer with a thickness of 700 µm, onto which a 250 µm SU-8 50 layer is spun. After 3h baking at 95ºC, the wafer is exposed to UV light with a dose of 350 mJ/cm^2 with the appropriate mask. The post exposure bake (PEB) for 20 minutes at 95ºC and the development using PGMEA finishes the master fabrication. M-SSE pre-polymer obtained as above detailed is poured onto the SU-8 master, avoiding overflow. A second degasification is done so as to remove air bubbles that may be trapped in the microstructures. Then, devices are baked for completing polymerization. Just afterwards, the cantilevers and samples are peeled off from the master.
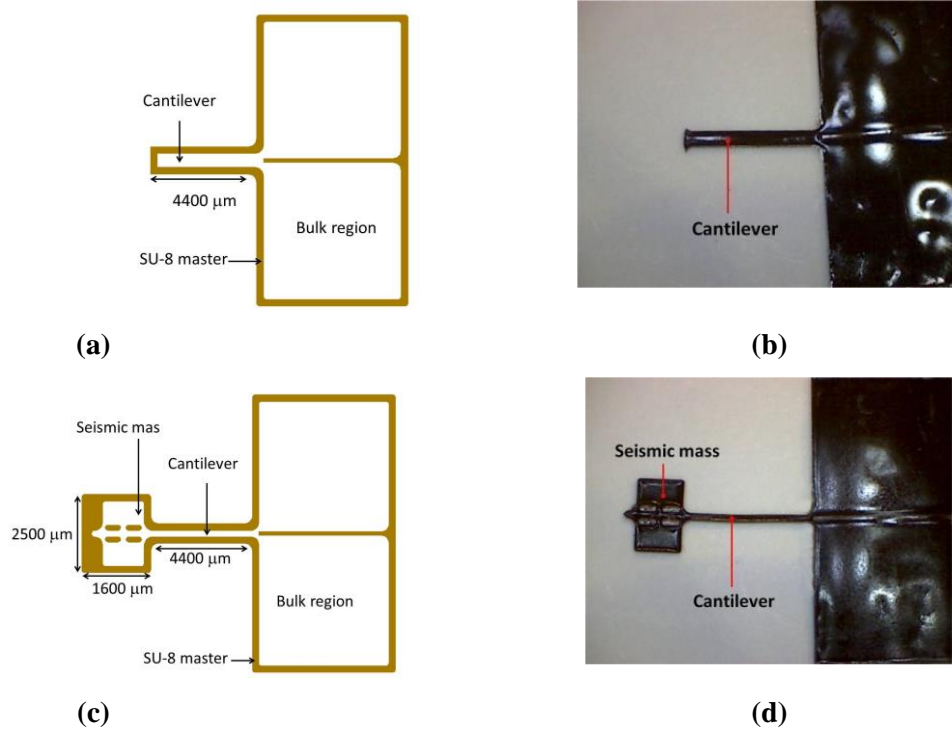
Figure 1. Design (a) and fabricated (b) M-SSE cantilevers for mechanical characterization. In (c) and (d), a seismic mass is included in the cantilever tip to enhance response when actuated magnetically.

2.4. Characterization

2.4.1. TEM

Structural homogeneity was determined using images from transmission electron microscopy (TEM), which were obtained by the system JEOL 2011, Jeol Ltd., USA. The distribution and size of the Fe_3O_4 nanoparticles included in the M-SSE was analyzed. From these images, 10 fields containing each of them between 20-100 MNP, depending on the sample, have been analysed by image software (ImageJ, USA).

2.4.2. Biocompatibility properties

Cytotoxicity was determined using vascular smooth muscle cells (VSMC) cultured from rat aorta by using the colorimetric 3-(4,5-dimethylthiazol-2-yl)-2,5-diphenyltetrazolium bromide (MTT) assay [44]. The ability of viable cells to transform the MTT salt into formazan dyes allows its optical characterization at 540 nm in a microplate spectrophotometer reader (BioTek® Synergy HT, USA). Cell viability is expressed as percentage in relation to controls (non-treated cells). Samples from S_0 to S_6 have been studied for three different sample volumes: $a = 20$ mm^3; $b = 30$ mm^3 and $c = 40$ mm^3.

2.4.3. Optical properties

The optical transmittance as a function of the FF concentration has been studied by coupling a broadband light source (HL-2000, Ocean Optics, USA) directly connected to multimode fiber optic (Thorlabs, Dachau, Germany) with a core diameter of 125 µm. Light emerging from this fibre which is placed orthogonally to each slab sample

(with an identical optical path of 250 μm in all cases). A second fiber optics with a core diameter of 230 μm is used to collect light emerging from the M-SSE, which is directly connected to a spectrometer (HR 4000, Ocean Optics, USA). 10 consecutive scans (each of which requiring an integration time of 100 ms) were done for statistical reasons.

2.4.4. Magnetic properties

In order to determine the magnetic properties of the M-SSEs, a vibrating sample magnetometer (VSM, Oxford Instruments, UK) has been used for obtaining the magnetization of the slab samples S_1 to S_6 at 300K.

2.4.5. Mechanical properties

The Young's modulus of M-SSE (Y_{M-SSE}) for different FF concentrations has been determined by experimentally recording the deflection of cantilevers without seismic mass under the action of the gravity by using a confocal microscope (PLμ 2300 Optical Imaging Profiler, Sensofar, Spain) with software (PLμ Confocal Imaging Profiler, Sensofar, Spain). Samples with the lowest FF concentration (S_0 to S_2) presented very small contrast, which resulted in high experimental errors. Here, 2,5 mg of blue dye (Conasol blue 25, Proquimac Color, Spain) was used to enhance contrast and to reduce the experimental errors in the confocal measurements.

2.4.6. M-SSE magnetic cantilevers

Magnetic cantilevers were fabricated using samples S_1 to S_6 (S_0 was not studied since it corresponds to clean PDMS, and PDMS-cantilevers have already been published by our group [45]). These structures have been magnetically characterized by placing them on a positioning stage over a permanent magnet (0,45 T nominal value). This magnet is also located on a vertical stage; thereby it is possible to change the B_{app} to the cantilever by changing the distance between them. The deflection is captured by placing a CCD camera (Imaging Pixelfly, 205 X2 1475, Germany) in plane, orthogonal to the cantilever length.

3. Results and Discussion

3.1. Patterning

One of the most important issues when using PDMS in combination with an additive is to verify that the presence of this last component is not affecting polymerization . If this point is of relevance when defining slab samples (where sticky surfaces may occur), it becomes crucial when using such materials by soft lithography to define microdevices. Incomplete polymerization may lead to fragile devices with a large variation of their properties (especially Young's modulus).

In our case, samples S_0 to S_5 required exactly the same polymerization time (20 minutes), demonstrating that the additive was not affecting the formation of the 3D polymeric matrix. Conversely, S_6 was fully polymerized after 35 min. This result suggests that the additive concentration limit was reached with S_6 and therefore higher concentrations were not considered.

3.2. Structural material properties

Slab samples with low (S$_2$) and high (S$_6$) FF concentration have been used for the image analysis to calculate and compare the average particle diameter. Histograms illustrating nanoparticle size distribution (D_{TEM}) are presented in Figure 3 a) and b), together with representative TEM images (insets in both figures). Gaussian fit on TEM results shows a single peak in both samples, which can be associated with a single particle size with mean size of (8 ± 4) nm and (7 ± 4) nm for S$_2$ and S$_6$ samples, respectively. From these figures, it can be seen the absence of aggregates as well as the homogenous distribution of MNPs on the polymeric matrix independently on the additive concentration. In addition, it has been demonstrated that the PDMS matrix can host much larger FF volumes than these previously reported [46], [47] without a noticeable increase of the aggregate size and number. In turn, this higher FF concentration will assure a higher actuation to a magnetic stimulus, as it will be discussed in the following sections.

(a)   (b)
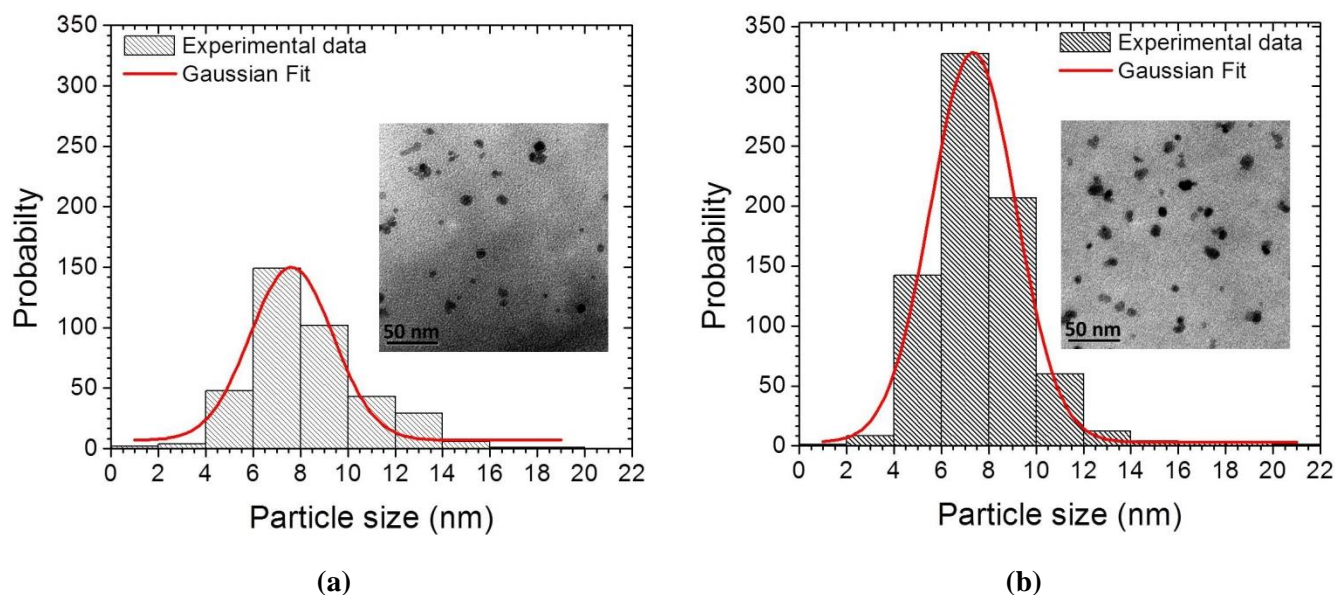
Figure 3. Nanoparticle size distribution by TEM image analysis (D_{TEM}) and the Gaussian fitting for (a) 3,5 % (S$_2$) and (b) 24,6% (S$_6$) M-SSE. Captions on each figure correspond to TEM images of both materials after polymerization, where the black scale bar corresponds to 50 nm.

3.3. Biocompatibility

In Figure 4, the cell viability percentage of the 18 samples under study is represented according to the FF concentration and the volume of each sample. Samples containing between 1.7 % FF and 20.3 % FF showed 100 % viability independently on the sample volume. Most concentrated samples (24.6 % FF) only showed significant differences (percentage of cell viability below 100 %) in the case of volume c (the highest volume analysed). According to these data, FF cytotoxicity is very low and most of the prepared materials can be used in biological application without additional modification
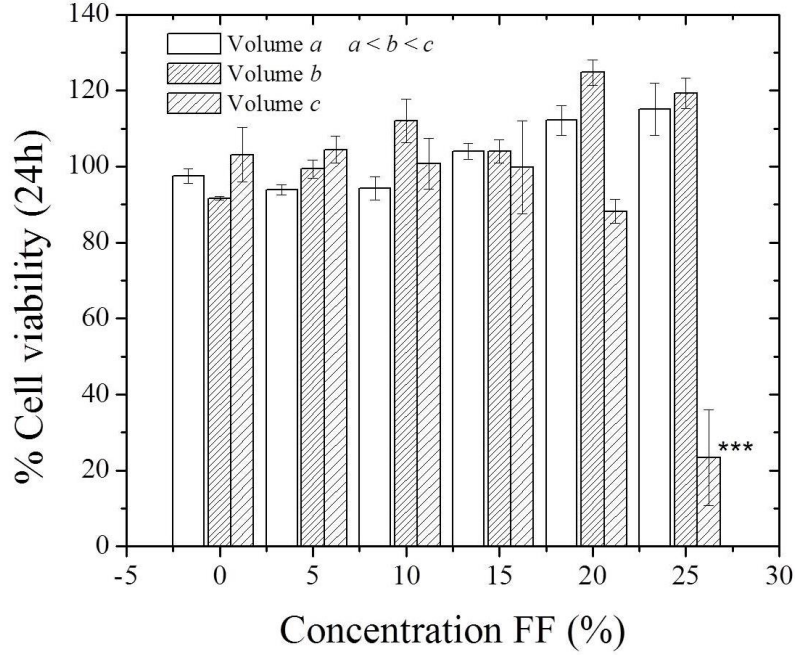
Figure 4: Cell viability as a function of FF concentration for each M-SSE slab sample (from S_0 to S_6) with ifferent geometries (w, l, h, in mm): $a = 2, 5, 2$; $b = 3, 5, 2$ and $c = 4, 5, 2$ are studied.

3.4. Magnetization

Figure 5 shows the specific magnetization (σ, emu/g units) as a function of the $B_{app}(=\mu_0 H)$ of slab samples S_1 to S_6. None of them show either coercivity or remanence at room temperature. These results are indicative of their superparamagnetic behaviour. This fact is in agreement with the superparamagnetic nature of the 10nm to 15 nm Fe_3O_4 nanoparticles at room temperature [31]. On the same figure, the values of specific magnetization ($\sigma(1.1T)$, emu/g units) of each sample are included.
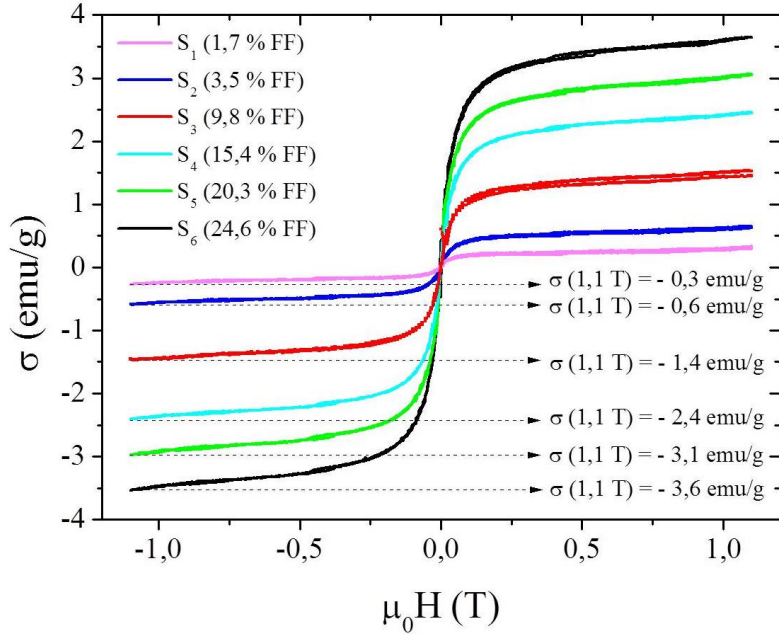
Figure 5. Magnetic loops for samples S_1 to S_6 at room temperature for different FF concentration in function of the B_{app}.

According to superparamagnetic theory [48], the magnetic particle size can be calculated from the true magnetic moment of each particle (μ) using the Langevin equation, Eq.1, which has been used for fitting the magnetization curves shown in Figure 5 a). From the calculated μ, values of particle size can be obtained using Eq. 2 (D_L).

$$M = M_S\left(\coth\left(\frac{\mu H}{k_B T}\right) - \frac{k_B T}{\mu H}\right) \qquad (1)$$

$$D_L = \sqrt[3]{\frac{6\mu}{M_S \pi}} \qquad (2)$$

Where k_B is the Boltzmann constant, T is the absolute temperature, M is the magnetization and M_S is the saturation magnetization (both magnetizations have emu/cm^3 units) and H is defined as B_{app}/μ_0.

Figure 6 shows D_L results as a function of FF concentration.

Figure 6. Particle size obtained from Langevin equation (D_L) for samples S_1 to S_6.

D_L values obtained from Eq. 2 are compared with values obtained from TEM pictures (D_{TEM}) for samples S_2 and S_6, see Table 2. Since the magnetic measurements do not take into account the presence of the surfactant layer [49] at the surface of the MNPs, the average values of particle size obtained from Eq. 2 are smaller than those obtained from TEM (D_{TEM}).

Thus, the particle size can be recalculated as follows

$$D_L + 2a_0 = D'_L \qquad (3)$$
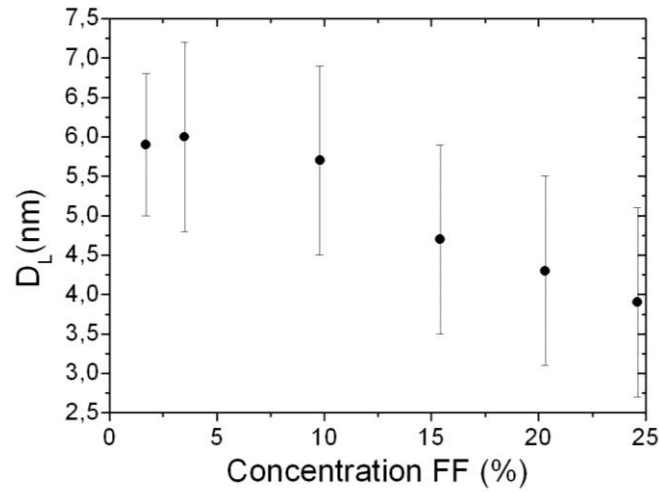
where a_0 is the thickness of a unit cell that corresponds to 0,83 nm for magnetite [50], [51] and D_L is the particle size obtained from Eq. 2. If this issue is considered, a good agreement is obtained then between the D'_L value from Eq. 3 and the TEM observations (Table 1). On the basis of such results, it can be confirmed that no aggregates are formed, even with the samples with the highest FF concentration.

Table 1. Summary for values of nanoparticle size obtaining form Eq. 2 (D_L),values form TEM study ($D_{TEM+Gaussian}$) and Eq. 3 (D'_L) for both slab samples S_2 and S_6.

Sample	D'_L (nm)	$D_{TEM+Gaussian}$ (nm)	D_L (nm)
S_2	8 ± 1	8 ± 4	6 ± 1
S_6	6 ± 1	7 ± 4	4 ± 1

3.5. Mechanical Properties

Maximum deflection (y_{max}) of the cantilevers without seismic mass has been measured. This allows obtaining the Y_{M-SSE} values using Eq. 4.

$$Y_{M-SSE} = \frac{3\rho g l^4}{2 y_{max} h^2} \qquad (4)$$

10

where ρ is the M-SSE density, g the gravitational field and, as previously described, l and h are the length and thickness of the cantilever, respectively.

Figure 7 shows the experimental $Y_{M\text{-}SSE}$ values for samples from S_1 to S_6. An increasing tendency is observed until it reaches 20,3 % volume FF. Such tendency is compared against a theoretical model [52] where the Y of a composite for the case of rigid particles in an elastic matrix ($Y_{M\text{-}SSE}$) is defined as a function of the Y corresponding to the unfilled-polymeric matrix (Y_{PDMS}), and the volume additive factor (v_f):

$$Y_{M-SSE} = \frac{Y_{PDMS}}{1 - 3v_f}$$ (5)

The theoretical analysis using this model [53] is also presented in Figure 7, showing a similar tendency as the experimental data for additive concentration below 20,3%. For S_6 the value experimental value of $Y_{M\text{-}SSE}$ does not follow the tendency predicted by the theoretical analysis. The reason for this fact can be associated to the incomplete polymerization of PDMS due to the FF oversaturation. This assumption is endorsed by the fact that, during patterning, this sample required longer baking times for curing.
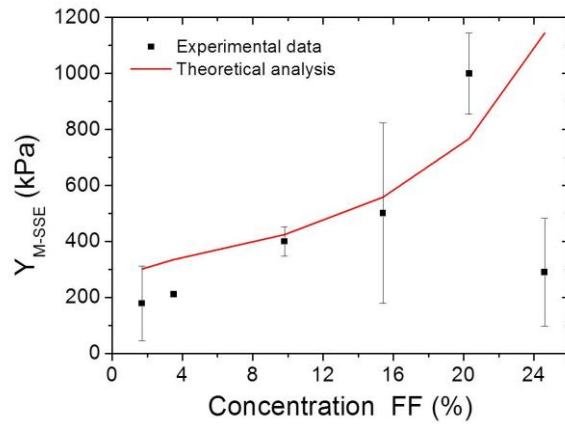
Figure 7. Experimental results of the Young's modulus for M-SSE ($Y_{M\text{-}SSE}$) in function of the FF concentrations into the PDMS. Samples S_1 to S_6 have been studied obtaining an increasing tendency until it reaches the maximum corresponding to 24,6% which shows a drop in the value of $Y_{M\text{-}SSE}$.

3.6. Optical Properties

The optical properties of any polymeric matrix may strongly vary when an additive is included. When combining FF and PDMS, not only the particle size, distribution, shape or capping of the MNP [54], but also the optical and chemical properties of the carrier fluid may potentially change the spectral response of the M-SSE. The high optical transmittance of PDMS makes it the suitable material to define photonic lab on a chip systems [55]. With regard to this application, having the possibility to include biocompatible magnetically-actuable elements (as could be

valves) is of high interest. Before such integration can be even considered, it becomes necessary to determine the effect of the FF concentration on the PDMS transmittance.

Figure 8 a) shows the transmittance for slab samples S_0 to S_6 in a wavelength range between 400 nm and 900 nm. The transmittance decreases as the FF concentration increases. Samples S_1 and S_2 have a decrease in transmittance below 50% (3 dB) and therefore, for small enough optical path, these M-SSE may still valid for developing photonic lab on a chip systems with magnetic actuation. Conversely, samples with larger FF concentration (S_3 to S_6) can be considered opaque in the working rage (decreased in transmittance higher than 73%, corresponding to 1.4 dB) and, even though they will have a higher displacement upon magnetic actuation, they cannot be considered as valid materials to be used with photonic/optic readout. This argument is validated

From the previous measurements, the molar absorption coefficient (ε) can be calculated from the Beer-Lambert law: A=$\varepsilon c L$, which relates the absorbance (*A*) of M-SSE, the path length (*l*), and the FF concentration (*c*) of M-SSE (from S_1 to S_6). The measurements were made at $\lambda = 635$ nm, the absorbance was obtained from transmittance data (Figure 8a)) and the concentration corresponds to 1,7 %, 3,5 %, 9,8 %, 15,4 %, 20,3 % and 24,6 % in volume but expressed in the appropriate units (molar). Values corresponding to ε in function of concentration of FF are presented in Figure 8 b).

| (a) | (b) |
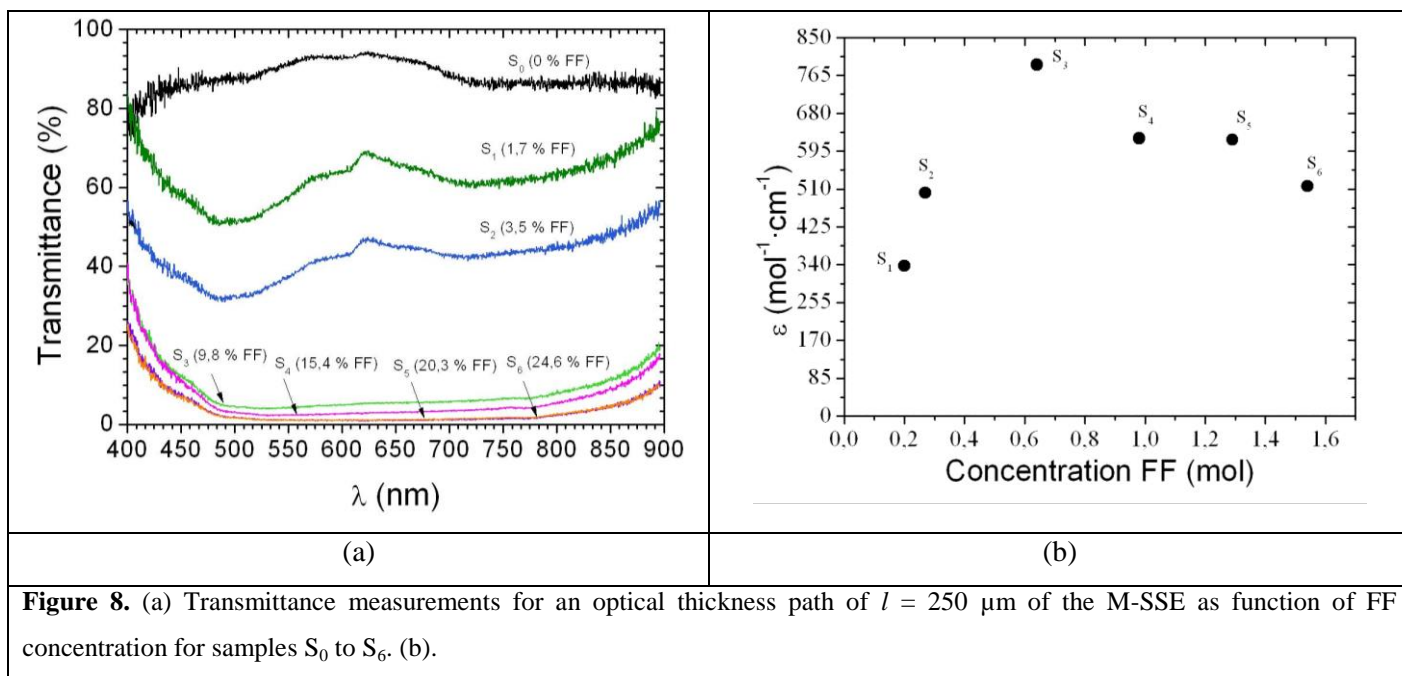
Figure 8. (a) Transmittance measurements for an optical thickness path of *l* = 250 µm of the M-SSE as function of FF concentration for samples S_0 to S_6. (b).

3.7. Characterization of M-SSE magnetic cantilevers

Once the M-SSE has been characterized, the next step is to implement devices that take advantage of the added functionality. As an example, six different cantilevers with seismic mass, one for each FF concentration, were fabricated and their deflection as a function of the external magnetic field was measured. Figure 9 a) shows the

resulting deflection when the magnetic actuation is applied. As it can be observed, the deflection for a given FF concentration is directly proportional to the magnetic field. In addition, cantilever sensitivity increases, for a fixed B_{app}, with the FF concentration (it can be seen how, for $B_{app} = 0,29$ T, cantilevers fabricated with S_1 and S_6 have a deflection of 710 µm and 9290 µm, respectively). Only cantilevers obtained with S_1 and S_2 could be measured for $B_{app} > 0,29$ T. Cantilevers obtained with S_3 to S_6 had a deflection that was beyond the measuring range of our experimental setup (the cantilever and the magnet were physically in contact), and therefore we consider them as saturated.

From this data, we can define two main parameters: the dynamic deflection range (D_{max}, being the difference between the deflection with no applied magnetic field and the deflection for $B_{app} = 0,29$ T) and the minimum magnetic field necessary to have a measurable cantilever deflection (B_{min}). Figure 9 b) shows D_{max} and B_{min} as a function of the FF concentration. From these results, two expectable, yet key features are obtained. Firstly, D_{max} increase with the FF concentration. Above S_4, the tendency follows a saturation curve, which can be understood from the fact that the cantilever is anchored to a bulk region and therefore, maximum displacement is limited by both this and for the viscoelastic properties of PDMS. Secondly, the required magnetic field so as to cause a measurable displacement also decreases with the FF concentration.

Sample	D_{Min} (µm)	B_{Min} (T)
S_0	0	0
S_1	610	0.27
S_2	610	0.25
S_3	610	0.22
S_4	610	0.20
S_5	610	0.20
S_6	660	0.19
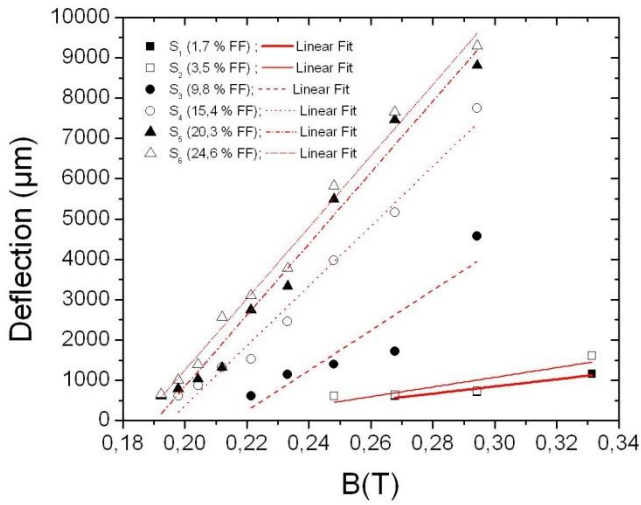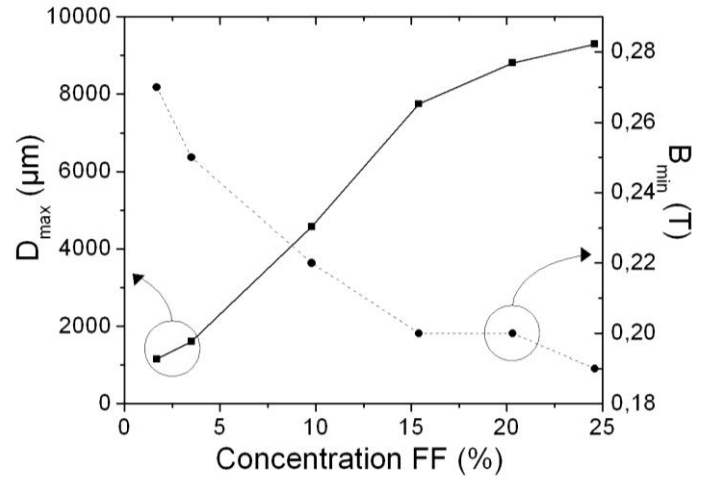
Figure 9. (a) Cantilevers deflections obtained with M-SSEs S_1 of o S_6 as a function of magnetic actuation. (b) Maximum deflection (D_{max}) and minimum applied magnetic field (B_{app}) to have a measurable cantilever deflection (B_{min}) as a function of the FF concentration for M-SSE S_1 to S_6.

To summarize, the different studied properties of the here discussed M-SSE and its application to magnetic cantilevers are shown in Table 2. In this context, the selection of the given FF concentration will depend on the specific type of measurement to be done: Low FF content materials are suitable for photonic and biological applications (higher optical transmittance and biocompatibility). Conversely, larger response to magnetic stimulus is obtained with samples S_4 and S_5, making these materials optimal for magnetic valves or micro flow controllers. Finally, S_6 has shown a dramatic decrease of its Y, probably because the amount of FF (and its liquid carrier) is hampering the PDMS polymerization and therefore determining the saturation limit using FF as additive in PDMS.

Table 2: summary of the parameters studied in the characterization of M-SSE

Sample	% mass FF	Y (kPa)	Curing time (min)	Mean value T (%)	Range T (%)	Ms (emu/g)	Magneto/Mechanical			Biocompatibility
							D_{max}(mm)	B_{min}(T)	ΔB_d(t)	
S_0	0	200	20	88.1±0.4	(73-95)±1	0	0	0	0	
S_1	4.65	179±133	20	62.7±3.4	(50-83)±3	0.3±0.2	1.2±1	0.27±0.15	(0.27-0.33)±0.15	
S_2	6.46	212±7	20	42.75±0.6	(31-57)±1	0.6±0.005	1.6±1	0.25±0.15	(0.25-0.33)±0.15	
S_3	14.87	400±52	20	8.5±2.6	(4-38)±3	1.5±0.01	4.6±1	0.22±0.15	(0.25-0.29)±015	
S_4	22.88	501±322	25	6.4±0.2	(2-41)±0.5	2.5±0.005	7.7±1	0.20±0.15	(0.20-0.29)±0.15	
S_5	29.91	1000±144	25	3.5±0.1	(0.8-26)±1	3.1±0.006	8.8±1	0.20±0.15	(0.20-0.29)±0.16	
S_6	35.77	291±192	30-40	3.4±0.8	(0.9-25)±2	3.6±0.005	9.3±1	0.19±0.16	(0.19-0.29)±0.16	

4. Conclusions

Several M-SSEs were prepared by incorporating different concentrations of FF based on Fe_3O_4 nanoparticles into a PDMS matrix. Test microstructures have been fabricated using soft-lithography techniques obtaining cantilevers with different geometries. Particle size and distribution in the M-SSE have been studied using TEM. A homogenous distribution of the Fe_3O_4 nanoparticles is demonstrated even for the highest concentration of 24,6%. Furthermore, it has been shown that particle size distribution has a single Gaussian peak located at 8 nm ± 4 nm, which confirms no aggregates in the M-SSEs here presented. Additionally, particle size from this study is consistent with the superparamagnetic behavior for particle sizes around and below 10 nm. A decrease of the transmittance with the concentration of the FF is observed. For an optical path of 250 μm, the M-SSE with the highest concentration shows a transmittance close to 0% and can be considered as totally opaque. The magnetization as a function of the applied magnetic field for samples S_1 to S_6 shows neither coercivity nor remanence, in agreement with the superparamagnetic nature of the used FF. Finally, the experimental and the theoretical Y_{M-SSE} show a similar tendency with the FF concentration, except for the drastic decrease at concentrations beyond 20 %. Thus, the M-SSE presented in this work keeps the elastomeric mechanical properties of the polymer while providing a magnetic functionality by simply varying the FF concentration. These results prove that the proposed M-SSE are suitable in a large number of applications, ranging from magnetic valves to optical attenuators.

Acknowledgements

References

[1]   G. Pasparakis and M. Vamvakaki, "Multiresponsive polymers: nano-sized assemblies, stimuli-sensitive gels and smart surfaces," *Polym. Chem.*, vol. 2, no. 6, p. 1234, May 2011.

[2]   D. Kuckling and A. Wycisk, "Stimuli-responsive star polymers," *J. Polym. Sci. Part A Polym. Chem.*, vol. 51, no. 14, pp. 2980–2994, Jul. 2013.

[3]   S. Dai, P. Ravi, and K. C. Tam, "pH-Responsive polymers: synthesis, properties and applications," *Soft Matter*, vol. 4, no. 3, p. 435, Feb. 2008.

[4]   S. Dai, P. Ravi, and K. C. Tam, "Thermo- and photo-responsive polymeric systems," *Soft Matter*, vol. 5, no. 13, pp. 2513–2533, Jun. 2009.

[5]   R. Shankar, T. K. Ghosh, and R. J. Spontak, "Dielectric elastomers as next-generation polymeric actuators," *Soft Matter*, vol. 3, no. 9, p. 1116, Aug. 2007.

[6]   T. Kimura, Y. Umehara, and F. Kimura, "Magnetic field responsive silicone elastomer loaded with short steel wires having orientation distribution," *Soft Matter*, vol. 8, no. 23, p. 6206, May 2012.

[7]   M. Arruebo, R. Fernández-Pacheco, M. R. Ibarra, and J. Santamaría, "Magnetic nanoparticles for drug delivery," *Nano Today*, vol. 2, no. 3, pp. 22–32, Jun. 2007.

[8]   M. Joglekar and B. G. Trewyn, "Polymer-based stimuli-responsive nanosystems for biomedical applications.," *Biotechnol. J.*, vol. 8, no. 8, pp. 931–45, Aug. 2013.

[9]   G. Chan and D. J. Mooney, "New materials for tissue engineering: towards greater control over the biological response.," *Trends Biotechnol.*, vol. 26, no. 7, pp. 382–92, Jul. 2008.

[10]   D. Roy, J. N. Cambre, and B. S. Sumerlin, "Future perspectives and recent advances in stimuli-responsive materials," *Prog. Polym. Sci.*, vol. 35, no. 1–2, pp. 278–301, Jan. 2010.

[11]   E. Cabane, X. Zhang, K. Langowska, C. G. Palivan, and W. Meier, "Stimuli-responsive polymers and their applications in nanomedicine.," *Biointerphases*, vol. 7, no. 1–4, p. 9, Dec. 2012.

[12]   N. Hotz, L. Wilcke, and W. Weber, "Design, synthesis, and application of stimulus-sensing biohybrid hydrogels.," *Macromol. Rapid Commun.*, vol. 34, no. 20, pp. 1594–610, Oct. 2013.

[13]   F. Khademolhosseini and M. Chiao, "Fabrication and Patterning of Magnetic Polymer Micropillar Structures Using a Dry-Nanoparticle Embedding Technique," *J. Microelectromechanical Syst.*, vol. 22, no. 1, pp. 131–139, Feb. 2013.

[14]   M. A. Ward and T. K. Georgiou, "Thermoresponsive Polymers for Biomedical Applications," *Polymers (Basel).*, vol. 3, no. 4, pp. 1215–1242, Aug. 2011.

[15]   P. Schattling, F. D. Jochum, and P. Theato, "Multi-stimuli responsive polymers – the all-in-one talents," *Polym. Chem.*, vol. 5, no. 1, p. 25, 2014.

[16]   Y. Yu and T. Ikeda, "Photodeformable Polymers: A New Kind of Promising Smart Material for Micro- and Nano-Applications," *Macromol. Chem. Phys.*, vol. 206, no. 17, pp. 1705–1708, Sep. 2005.

[17]   "Magnetic field responsive smart polymer composites." [Online]. Available: http://www.pharmtech.sote.hu/pharma/sites/default/files/AdvPolymSci_07_206_137_review.pdf. [Accessed: 02-Aug-2013].

[18]   R. T. Olsson, M. A. S. Azizi Samir, G. Salazar-Alvarez, L. Belova, V. Ström, L. A. Berglund, O. Ikkala, J. Nogués, and U. W. Gedde, "Making flexible magnetic aerogels and stiff magnetic nanopaper using cellulose nanofibrils as templates.," *Nat. Nanotechnol.*, vol. 5, no. 8, pp. 584–8, Aug. 2010.

[19]   K. Mosbach and U. Schröder, "Preparation and application of magnetic polymers for targeting of drugs," *FEBS Lett.*, vol. 102, no. 1, pp. 112–116, Jun. 1979.

[20]   L. L. Lao and R. V Ramanujan, "Magnetic and hydrogel composite materials for hyperthermia applications.," *J. Mater. Sci. Mater. Med.*, vol. 15, no. 10, pp. 1061–4, Oct. 2004.

[21]   R. Langer, "Biomaterials in Drug Delivery and Tissue Engineering: One Laboratory's Experience," *Acc. Chem. Res.*, vol. 33, no. 2, pp. 94–101, Feb. 2000.

[22]   B. Ozkale, E. Pellicer, M. A. Zeeshan, J. F. López-Barberá, J. Nogués, J. Sort, B. J. Nelson, and S. Pané, "One-pot electrosynthesis of multi-layered magnetic metallopolymer nanocomposites.," *Nanoscale*, vol. 6, no. 9, pp. 4683–90, Apr. 2014.

[23]   M. Ionescu, B. Winton, D. Wexler, R. Siegele, A. Deslantes, E. Stelcer, A. Atanacio, and D. D. Cohen, "Enhanced biocompatibility of PDMS (polydimethylsiloxane) polymer films by ion irradiation," *Nucl. Instruments Methods Phys. Res. Sect. B Beam Interact. with Mater. Atoms*, vol. 273, no. null, pp. 161–163, Feb. 2012.

[24]   I. Yilgor and E. Yilgor, "Thermal stabilities of end groups in hydroxyalkyl terminated polydimethylsiloxane oligomers," *Polym. Bull.*, vol. 40, no. 4–5, pp. 525–532, Apr. 1998.

[25]   D. Kim and K.-S. Yun, "Patterning of carbon nanotube films on PDMS using SU-8 microstructures," *Microsyst. Technol.*, vol. 19, no. 5, pp. 743–748, Oct. 2012.

[26]   H. Makamba, J. H. Kim, K. Lim, N. Park, and J. H. Hahn, "Surface modification of poly(dimethylsiloxane) microchannels.," *Electrophoresis*, vol. 24, no. 21, pp. 3607–19, Nov. 2003.

[27]   V. J. Cadarso, J. A. Plaza, K. Zinoviev, C. Dominguez, S. de Pedro, S. Buttgenbach, and A. Llobera, "Cantilever-based poly(dimethylsiloxane) Microoptoelectromechanical Systems," in *2009 IEEE Sensors*, 2009, pp. 413–417.

[28]   A. Llobera, V. J. Cadarso, K. Zinoviev, C. Dominguez, S. Buttgenbach, J. Vila, J. A. Plaza, and S. Biittgenbach, "Poly(Dimethylsiloxane) Waveguide Cantilevers for Optomechanical Sensing," *IEEE Photonics Technol. Lett.*, vol. 21, no. 2, pp. 79–81, Jan. 2009.

[29]   A. Singh, M. Shirolkar, M. V. Limaye, S. Gokhale, C. Khan-Malek, and S. K. Kulkarni, "A magnetic nano-composite soft polymeric membrane," *Microsyst. Technol.*, vol. 19, no. 3, pp. 409–418, Aug. 2012.

[30]   D. Ivaneyko, V. Toshchevikov, M. Saphiannikova, and G. Heinrich, "Effects of particle distribution on mechanical properties of magneto-sensitive elastomers in a homogeneous magnetic field," Oct. 2012.

[31]   Q. A. Pankhurst, J. Connolly, S. K. Jones, and J. Dobson, "Applications of magnetic nanoparticles in biomedicine," *J. Phys. D. Appl. Phys.*, vol. 36, no. 13, pp. R167–R181, Jul. 2003.

[32]   A.-H. Lu, E. L. Salabas, and F. Schüth, "Magnetic nanoparticles: synthesis, protection, functionalization, and application.," *Angew. Chem. Int. Ed. Engl.*, vol. 46, no. 8, pp. 1222–44, Jan. 2007.

[33]   M. R. J. Gibbs, E. W. Hill, and P. J. Wright, "Magnetic materials for MEMS applications," *J. Phys. D. Appl. Phys.*, vol. 37, no. 22, pp. R237–R244, Nov. 2004.

[34]   R. P. Castillejos, J. E. i Tintó, and J. A. P. Plaza, *Study and applications of ferrofluids in microfluidics*. 2003.

[35]   A. K. Gupta and M. Gupta, "Synthesis and surface engineering of iron oxide nanoparticles for biomedical applications.," *Biomaterials*, vol. 26, no. 18, pp. 3995–4021, Jun. 2005.

[36]   S. Odenbach, "Ferrofluids—magnetically controlled suspensions," *Colloids Surfaces A Physicochem. Eng. Asp.*, vol. 217, no. 1–3, pp. 171–178, Apr. 2003.

[37]   Jasmin, A. L. M. Torres, L. Jelicks, A. C. C. de Carvalho, D. C. Spray, and R. Mendez-Otero, "Labeling stem cells with superparamagnetic iron oxide nanoparticles: analysis of the labeling efficacy by microscopy and magnetic resonance imaging.," *Methods Mol. Biol.*, vol. 906, pp. 239–52, Jan. 2012.

[38]   H. Ittrich, K. Peldschus, N. Raabe, M. Kaul, and G. Adam, "Superparamagnetic iron oxide nanoparticles in biomedicine: applications and developments in diagnostics and therapy.," *Rofo*, vol. 185, no. 12, pp. 1149–66, Dec. 2013.

[39]   M. Suresh, V. Sujatha, and S. Mahalaxmi, "The role of nanoparticles and nanodevices in nanomedicine," *Res. J. Pharm. Biol. Chem. Sci.*, vol. 5, no. 2, pp. 1869–1879, 2014.

[40]   V. Sundaresan, J. U. Menon, M. Rahimi, K. T. Nguyen, and A. S. Wadajkar, "Dual-responsive polymer-coated iron oxide nanoparticles for drug delivery and imaging applications.," *Int. J. Pharm.*, vol. 466, no. 1–2, pp. 1–7, Mar. 2014.

[41]   X. L. Liu and H. M. Fan, "Innovative magnetic nanoparticle platform for magnetic resonance imaging and magnetic fluid hyperthermia applications," *Curr. Opin. Chem. Eng.*, vol. 4, pp. 38–46, May 2014.

[42]   I. Hilger, "In vivo applications of magnetic nanoparticle hyperthermia.," *Int. J. Hyperthermia*, vol. 29, no. 8, pp. 828–34, Dec. 2013.

[43]   Y. Xia and G. M. Whitesides, "Soft Lithography," *Angew. Chemie Int. Ed.*, vol. 37, no. 5, pp. 550–575, Mar. 1998.

[44]   T. Mosmann, "Rapid colorimetric assay for cellular growth and survival: Application to proliferation and cytotoxicity assays," *J. Immunol. Methods*, vol. 65, no. 1–2, pp. 55–63, Dec. 1983.

[45]   A. Llobera, V. J. Cadarso, K. Zinoviev, C. Dominguez, S. Buttgenbach, J. Vila, J. A. Plaza, and S. Biittgenbach, "Poly(Dimethylsiloxane) Waveguide Cantilevers for Optomechanical Sensing," *IEEE Photonics Technol. Lett.*, vol. 21, no. 2, pp. 79–81, Jan. 2009.

[46] F. Pirmoradi, L. Cheng, and M. Chiao, "A magnetic poly(dimethylesiloxane) composite membrane incorporated with uniformly dispersed, coated iron oxide nanoparticles," *J. Micromechanics Microengineering*, vol. 20, no. 1, p. 015032, Jan. 2010.

[47] G. Filipcsei and M. Zrínyi, "Magnetodeformation effects and the swelling of ferrogels in a uniform magnetic field.," *J. Phys. Condens. Matter*, vol. 22, no. 27, p. 276001, Jul. 2010.

[48] D. K. Kim, Y. Zhang, W. Voit, K. V. Rao, and M. Muhammed, "Synthesis and characterization of surfactant-coated superparamagnetic monodispersed iron oxide nanoparticles," *J. Magn. Magn. Mater.*, vol. 225, no. 1–2, pp. 30–36, Jan. 2001.

[49] D. . Kim, Y. Zhang, W. Voit, K. . Rao, J. Kehr, B. Bjelke, and M. Muhammed, "Superparamagnetic iron oxide nanoparticles for bio-medical applications," *Scr. Mater.*, vol. 44, no. 8–9, pp. 1713–1717, May 2001.

[50] G. F. Goya, T. S. Berquó, F. C. Fonseca, and M. P. Morales, "Static and dynamic magnetic properties of spherical magnetite nanoparticles," *J. Appl. Phys.*, vol. 94, no. 5, p. 3520, Sep. 2003.

[51] R. Kaiser, "Magnetic Properties of Stable Dispersions of Subdomain Magnetite Particles," *J. Appl. Phys.*, vol. 41, no. 3, p. 1064, Mar. 1970.

[52] P. P. Castañeda, "A New Variational Principle and Its Application to Nonlinear Heterogeneous Systems," Jul. 2006.

[53] V. Q. Nguyen, A. S. Ahmed, and R. V Ramanujan, "Morphing soft magnetic composites.," *Adv. Mater.*, vol. 24, no. 30, pp. 4041–54, Aug. 2012.

[54] C. DeArmitt and R. Rothon, "Fillers and surface treatment," *Plast. Addit. Compd.*, vol. 4, no. 5, pp. 12–14, May 2002.

[55] J. Vila-Planas, E. Fernández-Rosas, B. Ibarlucea, S. Demming, C. Nogués, J. A. Plaza, C. Domínguez, S. Büttgenbach, and A. Llobera, "Cell analysis using a multiple internal reflection photonic lab-on-a-chip.," *Nat. Protoc.*, vol. 6, no. 10, pp. 1642–55, Oct. 2011.

ALL-PHOTONIC SU-8 VARIABLE OPTICAL ATTENUATOR

S. de Pedro[1], T. N. Ackermann[1], J.A. Plaza[1], Thomas[2], Erica Alvarez[1], Anke, S. Büttgenbach[3], V. J. Cadarso[4] and A. Llobera[1,3]

[1]Instituto de Microelectrónica de Barcelona, IMB-CNM (CSIC), Esfera UAB, Campus UAB, 08193 Bellaterra, Spain
[2]

[3]Institut für Mikrotechnik, Technische Universität Braunschweig, 38106 Braunschweig, Germany.

[4]Laboratory for Micro- and Nanotechnology, Paul Scherrer Institut (PSI), 5234 Villigen, Switzerland.

Abstract

This paper presents a combination between SU-8 and color dye-doped SU-8 which are implemented on a Micro-optoelectromechanical system (MOEMS) Variable Optical Attenuator (VOA). It design consists of an SU-8 quad-beam structure and a suspended waveguide forming a seismic mass aligned to input/output lignemnt elements for fiber optics positioning. Opto-thermal actuation is achieved by adding color dyes on the SU8-8 polymeric matrix. Those doped SU-8 define the actuation elements on the mechanical beams. Opto-thermal actuation is performed by focusing specific wavelengths on such structures. The result is a strong absorption with an increase in the heating and, straightforwardly, an expansion of the color dye-doped SU-8. This entails a displacement of the seismic mass causing a misalignment (i.e. an increase of the optical losses) between the waveguide and the input/output fiber optics as a function of the power actutaion. Experimental results have validated this approach, by showing the effect of the pumping power on the optical losses, with a slope of 0.17 dB/mW. Those experimental results are compared with simulations obtaining….

1. Introduction

Micro-opto-electro-mechanical systems (MOEMS) appear at the end of 1990s as a mergence of the micro-optics and micro-electro-mechanical systems (MEMS) because of the necessity of miniaturization and development/demand of integrated optical systems in one single device [1]. The development of MOEMS as light sensors/actuators results as the large expansion of the telecommunications, started in early 2000s, which demands the implementation of more robust, simpler and less power-consuming systems [].

Comparing MOEMS to their electrical counterparts MEMS, they present some outstanding advantages allowing its use in situations which their electrical counterparts (MEMS) may not be used. Some of these includes: i) immunity to electromagnetic interferences (EMI), ii) absence of shortcuts or spikes [2] and iii) the required electronics is reduced to a cheap light source and a photodetector. Additionally, they may be placed far from the measurement zone and being connected to the MOEMS by using fiber optics. Moreover MOEMS can be based on light properties like changes in intensity [3], wavelength [] and phase change [] for its use as sensing element. Furthermore, characteristics which have to be also highlighted are their high sensitivity and thermal stability [ref].

Systems such as optical switches [4], filters [], spectrometers [], tunable laser [] and variable optical attenuators (VOAs) [5] are included in MOEMS. Between them, VOAs allow

the active control of optical power coupled in a wavelength-division-multiplexed (WDM) network, being therefore of key importance in telecommunication applications. Nowadays, two main types of VOAs have been reported namely VOA-MOEMS and photonic lightwave circuits (VOA-PLCs).

In the first case, VOA-MOEMS are mainly fabricated using silicon surface (defining features on the surface of the substrate) or bulk (etched features into the bulk of materials) micromachining. Their actuation principle is electrostatics, either with comb-drive electrodes [5] or piezoelectrics [6]. Using this approach, previous works have shown a large dynamic range (> 35 dB) and a response time of tenths of milliseconds. Drawbacks on such approach consists of i) the required voltages (tenths of volts), ii) complex and expensive technology to passivate the electrical connexions for its application in possible water environments and iii) high cross sensitivity to EMIs. This prevents their massive implementation. To overcome these limitations, the actuation mechanism can be shifted from electrostatic to thermal actuation, which can be achieved by polymer technology. Hence, the use of polymers present some advantages in the cost, mechanical properties and ease processing leading to a production cost reduction in its application in MOEMS. For example, polymer-based VOA-PLCs have shown a slightly minor dynamic range, but with significantly lower operating voltages [Y.O.Noh, M. S. Yang et al, "PLC-type variable optical attenuator operated at low electrical power" *Electron. Lett.* 36 (2000), pp. 2032-2033].

Electrostatic and thermal actuation principles can be combined, but this mergence requires the use of highly specific polymers. Mechanically, they must provide outstanding aspect ratios; Young's modulus has to be in the order of GPa to assure a high flexibility (as compared to an identical silicon counterpart) and the coefficient of thermal expansion (CTE) must be significantly high so as to have an efficient energy transference. Moreover, from an optical point of view, it has to be transparent in the working wavelength. A polymer that matches such requirements is the epoxy-based negative-tone polymer SU-8 [H. Lorenz, M. Laudon and P. Renaud, "Mechanical characterization of a new high-aspect-ratio near UV-photoresist" Microelectron. Eng., 42 (1998), pp. 371-374]. This polymer has already used to developed microoptics [polymeric MOEMS VOA ref 6] and waveguides [polymeric MOEMS VOA ref 7] with attenuation close to 1 dB/cm. Furthermore, due to its excellent mechanical properties such as a Young's modulus ranging from 4.25 GPa to 4.95 GPa and its high coefficient of thermal expansion (CTE 52 ppm/ºC) SU-8 has been applied into VOAs systems which require electro-thermal actuation. An example of such structures has already been published by our group [7], where some aluminium stripes have been defined on top of an SU-8 MOEMS. Although effective, the response time was of some hundreds of milliseconds, and therefore unsuitable for telecommunication applications. In addition, the aluminium stripes may detach from the SU-8 after several duty cycles, compromising the applicability.

To address and solve this issue a possible solution is modifying the energy transfer mechanism which is directly related to the use of the material on the system. Previously, it has been proposed the use of SU-8 as base material for MOEMS because of its excellent mechanical and optical properties. Therefore, SU-8 can be transform to a material which can keep its polymeric characteristics but with new implemented properties by adding selected filler (bulk functionalization) depending on the actuation principle. The resulting polymer is called sensitive stimuli material (SSM) [] which is formed by a SU-8 host matrix with color dye-doped embedded in the polymeric matrix. Generally, such materials are capable to respond to an external stimuli, i.e. actuation principle, like a change in temperature, pH, solvent, electric or/and magnetic field []. One of the most common stimuli which can control the mechanical response is the change in temperature which can be achieved by exposing the SSM to a light of

a specific wavelength []. Among the other stimuli, it has been attractive because of its non-invasive and reversibly perform to induce a responsive behavior [8], it can be localized (in time and space) and its remote activation [9]. Thus, if the filler is sensitive for absorbing light at a given wavelength [10][**] it can increase the total temperature of the polymer obtained a mechanical response (expansion/contraction) as a response of the opto-thermal stimuli applied on the SSM. Some reported examples of possible applications those SSMs can be the description of Wang et al [], where a deformation of epoxy containing polymer colloids is performed when a light at specific wavelength irradiates it. The deformation consists on a shift shape from spheres to rods. In another published work, Akashi [], presents a light modulator consisting on……..

Considering the opto-thermal properties of both SU-8 and color dye-doped SU-8, a combination of those SU-8 which are implemented in a VOA MOEMS based on an opto-thermal actuation is here presented. The proposed configuration is basically compound of two main parts: the first consists on a SU-8 waveguide which is connected to the second: the color dye-doped SU-8 actation element. Waveguide confines the light coming from an input optical fiber to an output optical fiber. Moreover, when the light coming from a laser, i.e. the opto-thermal actuation, is focused on the actuation element, a change on its dimensions due to the absorption of the dye-doped SU-8 is achieved. Thus, a misalignment between the input/output optic fibers and the SU-8 waveguide is induced, obtaining a power modulation as a function of the opto-thermo stimuli on the actuation element.

2. Materials and Methods

2.1. Reagents

The negative-tone epoxy-based polymer SU-8 50 and its developer propylene glycol methyl ether acetate (PGMEA), both from MicroChem, Corp., USA were used following known recipes [11]. PDMS (Sylgard base Elastomer and curing agent) were acquired at Dow Corning Corp., USA. FF was purchased from Liquids Research Limited, North Wales, UK. Color dyes are

2.2. Design and simulation

Mechanically, as shown in Figure 1a), it consists of four mechanical beams that clamp the seismic mass to the frame, preventing angular misalignment. The seismic mass itself has been reduced to the minimum so as to enhance the response time, comprising only hinges between the waveguides that provides it with the required robustness.

Optically, the MOEMS VOA with general dimensions 9100 µm x 1300 µm x 125µm (width x lenght x thickness) consist on three fish-bone shaped structures (self-alignment systems) on each side of the MOEMS assure clamp and precise alignment between the input/output fiber optics (with a core diameter of 105 µm) and the waveguide included in the seismic mass. Considering refractive indices of SU-8 and air (n_{SU-8} = and n_{AIR} = 1.00)light coupled into SU-8 waveguide remains confined on it grounded on Total Internal Reflection (TIR) condition. Additional, those three waveguides with widths of 30 µm (for which are located at the outer part of the seismic mass) and 50 µm (for which is located at the central part of the seismic mass) and 10600 µm length and 100 µm thickness are attached to the mechanical structure by seven hinges. Here, mass displacements result in a misalignment between the waveguide and the input/output fiber optics and therefore losses are modulated as a function of the opto-thermal actuation. To this effect, four round shape actuation points have been defined on each VOA-MOEMS (1500 µm and 125 µ corresponding to the diameter and the thickness, respectively), Figure 1b). It consists on structured, colour dye-doped SU-8 with high absorbance at specific wavelengths. Absorbed light causes localized heating and expansion of the dye-doped polymer, which affects the adjacent undoped SU-8 mechanical beam. This result in an overall displacement of the quad beam structure and, as previously mentioned, with a misalignment between waveguides and the input/output fiber optics resulting on a modulation of the coupling losses as a function of the actuation (i.e. light focused on the actuation elements).
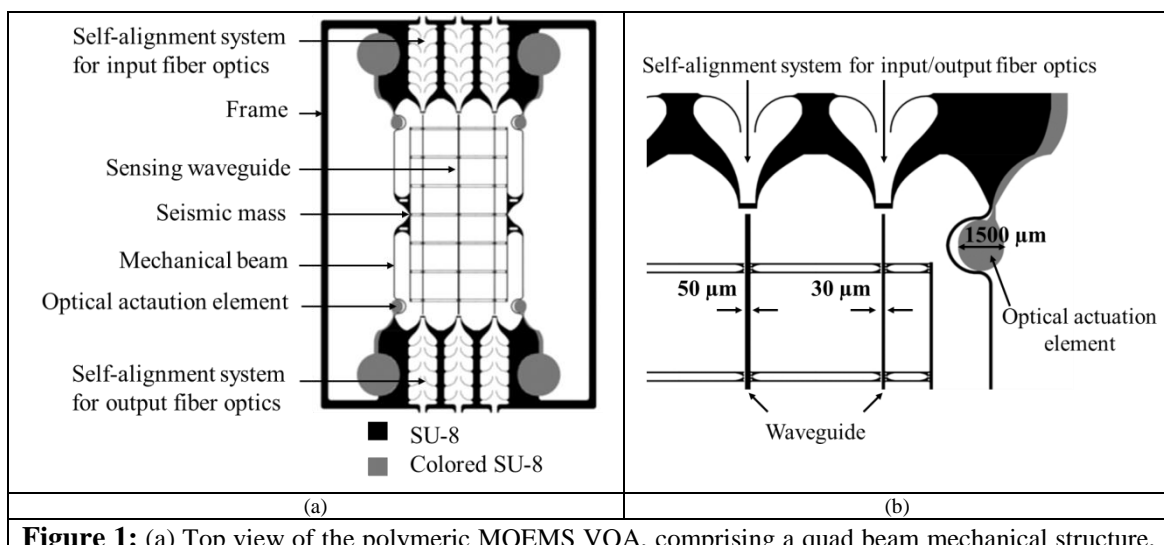

Figure 1: (a) Top view of the polymeric MOEMS VOA, comprising a quad beam mechanical structure,

three different waveguides, self-alignment system for input/output fiber optics clamping defined with SU-8 (black color) and actuation elements defined with dye-doped SU-8 (grey color).(b) Detailed image of the region where the dye-doped SU-8 is implemented, self-alignment system for input/output fiber optics and waveguides widths (50 µm and 30 µm).

Optical simulations of the proposed MOEMS VOA were done using the Trace Pro software (Lambda Research, Littleton, MA, USA). Figure 2 shows ray-tracing
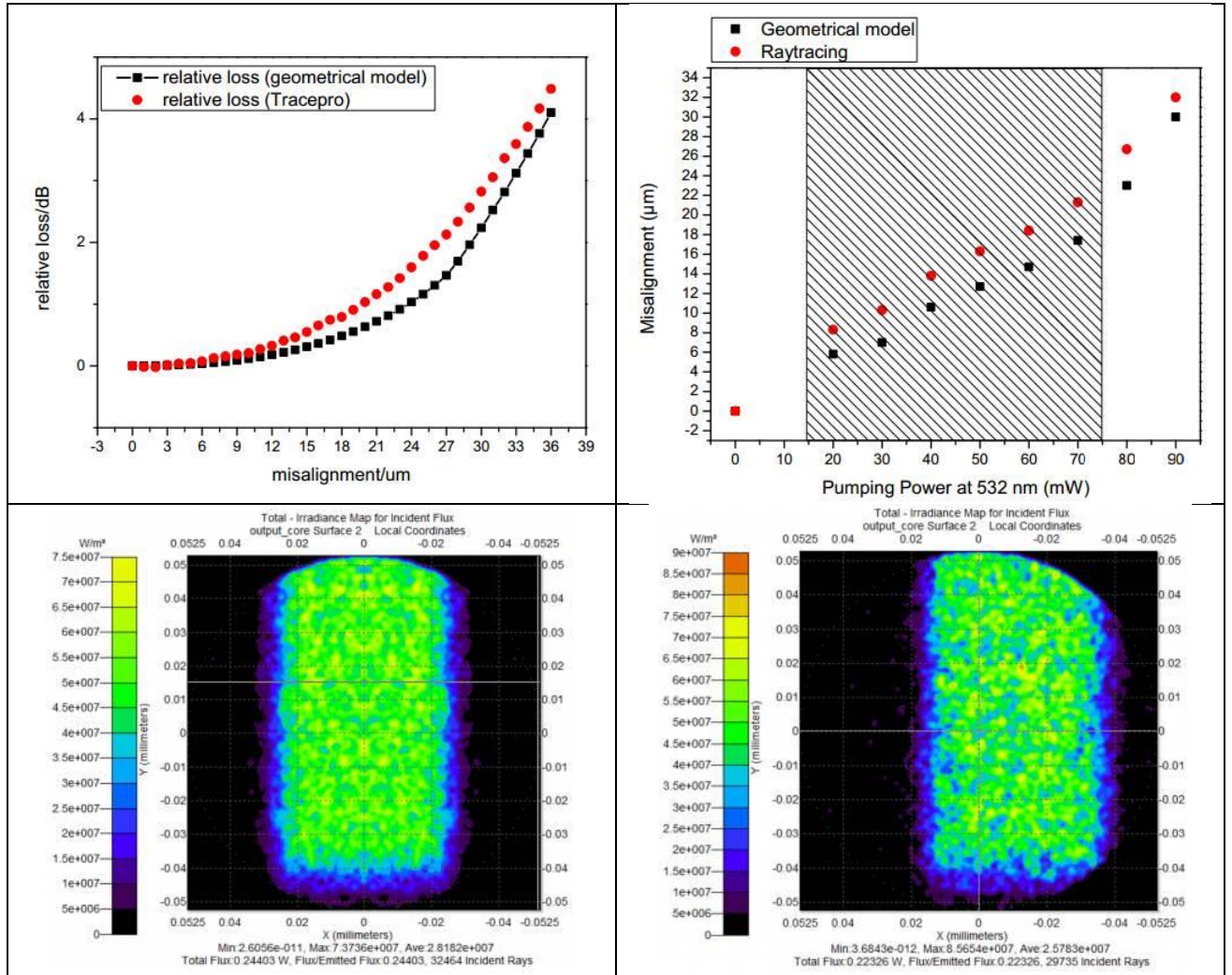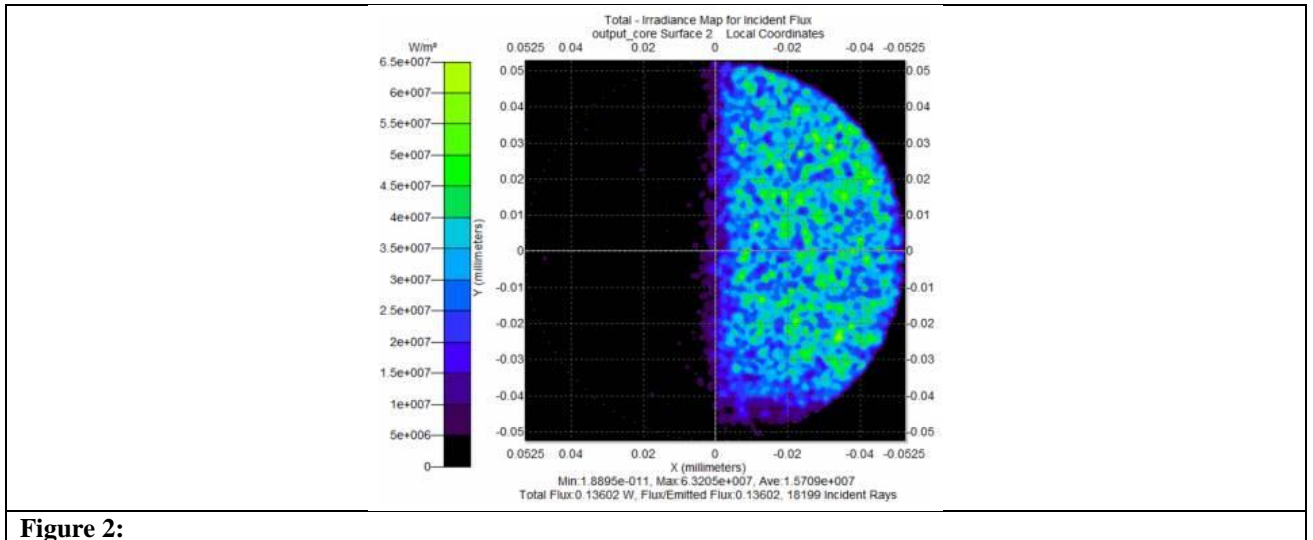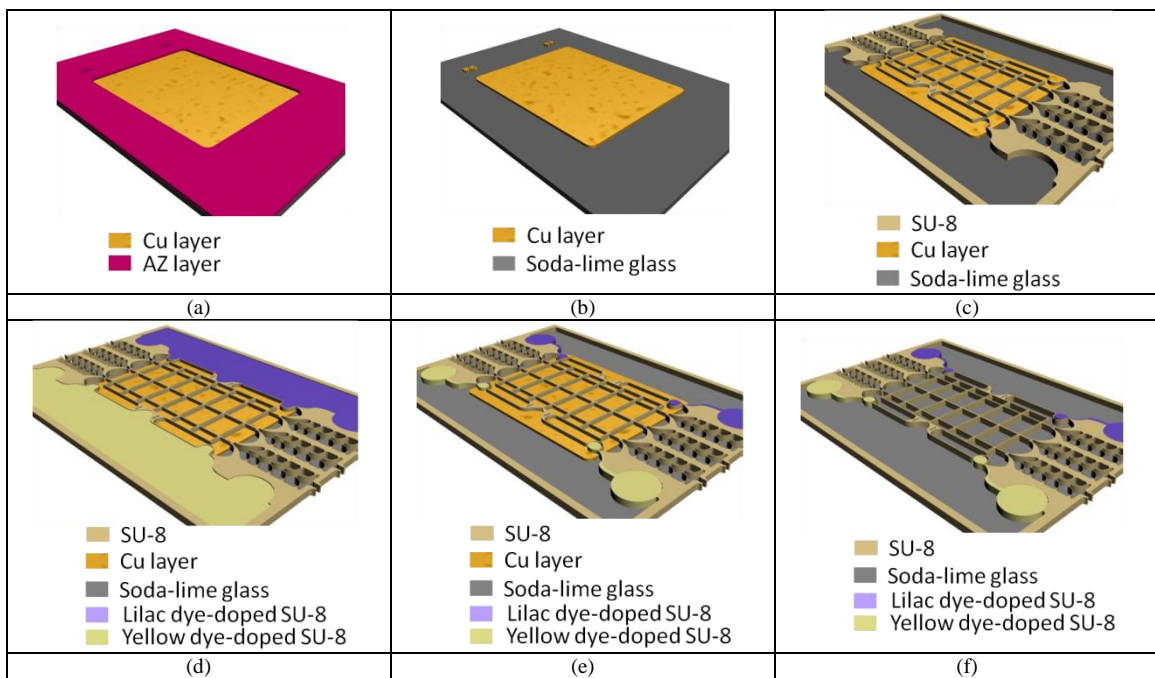
Figure 2:

2.3. Fabrication

Figure 3: Scheme of the fabrication process starting with (a) AZ9260 photoresist and the first mask the area to obtain a 20µm-thick Cu electroplating layer is defined. (b)After that the photoresist is removed by acetone. Here, (c) 125 µm of SU-8 is spun on the wafer where after using the second mask and the corresponding development the optomechanical parts of the VOA (self-alignment system for input/output fiber optics, sensing waveguide, mechanical beams, seismic mass and the frame) are defined. (d) The red-dye doped SU-8 is poured on the regions that have been defined between the frame and the mechanical beam. (e) Then, after using a third mask and the development of the doped SU-8 the definition of the actuation points are achieved. Finally, (f) after an etching of the sacrificial layer the MOEMS VOA is completely finished. (g) Image of the completely fabricated VOA with the mechanical and the actuation points.

The fabrication process starts on a 700 μm thick soda-lime glass, which is used as a substrate. A 20 nm Cr layer and 200 nm Cu seed layer are evaporated on the substrate. Then, a photoresist (AZ9260, MicroChemicals Gmbh. Ulm, Germany) is spun obtaining a thickness of 25 μm. After that, a first photolithographic mask defines the regions where the Cu seed layer will be electroplated obtaining a 20 μm-thick Cu layer, Figure 3a), following by rinsing in acetone to remove the photoresist. A short dip in Cu etches for removing the Cu seed layer is done, Figure 3b). To define VOA MOEMS a layer of SU-8 is spun (SU-8 2050, MicroChem Corporation, Newton, MA) for obtaining a thickness of 125 μm. After relaxation time of 20 minutes, wafers are soft baked (SB) for 2h at 95 °C on a hotplate. Then, the wafer is exposed to UV light using a second photolithographic mask required for defining the optomechanical parts of the VOA MOEMS (self-alignment system for input/output fiber optics, sensing waveguide, mechanical beams, seismic mass and the frame) followed by a post exposure bake (PEB) for 20 minutes at 95 °C. After that the first development step is carried out by immersing the wafers in propylene glycol methyl ether acetate (PGMEA, MicroChem Corporation, Newton, MA), Figure 3c). For further mechanical stabilization and cross-linking enhancement a hard bake (HB) for 2 h at 120 °C under nitrogen atmosphere is done. At this point the SU-8 dye-doped is poured on the regions that have been defined between the frame and the mechanical beam, Figure 3d), with a relaxation time of 20 minutes and a SB for 2h at 95 °C on a hotplate. Specifically, in this work 0.08 wt % of red dye has been mixed with the SU-8 obtaining a SU-8 red dye-doped. Here a second exposition to UV light is required by using a third photolithographic mask for defining the optical actuation elements followed by a PEB for 20 minutes at 95 °C. A second development step followed by a HB for 2 h at 120 °C under nitrogen atmosphere is done, Figure 3 e), too. The final part consists of an etching of the sacrificial layer, Figure 3f). At this point, the MOEMS VOAs structures are released, Figure 3g), finishes the fabrication process.

2.5. Characterization

2.5.1. Optical Properties

The optical losses as a function of time when the pumping light power (at a wavelength of 532 nm) was focused at the actuation points with different power. Thus, the setup inlcudes a 635 nm diode laser (Laser source, 635 nm, 2.5 mW, Model S1FC, Thorlabs GmbH, USA) which couples the light into a multimode fiber optic with a core diameter of 200 μm input fiber optics (Thorlabs GmbH, USA), which is placed on the fishbone-shape input self-alignment structure and it is used as sensing wavelength. The output fiber optic is identical and is placed at the output fishbone-shape, connected to a microspectromer (USB2000+, Ocean Optics). With no actuation, there is no misalignment between the waveguide and the collecting fiber optics, and therefore, the intrinsic optical losses can be measured. As the actuation is applied by pumping a green diode laser Nano 532 (Laser Nano 532, Qioptiq,) diode laser on the actuation element, since this wavelength presents the highest absorption using red dye (Proquimac, SPAIN).

3. Results and Discussion

3.1. Optical Properies

The intrinsic optical losses have been measured with no actuation on the MOEMS VOA…..

After intrinsic optical losses have been determined, the optical losses as a function of the time for different power pumpings diode laser are measured. Results are shown in Figure 4a) with an increase on the optical losses as the optothermal actuation is varied between 0 mW and 90 mW. Moreover, the relative losses present a very high repeatability as a function of the power of the pumping diode laser along the measurement time.

as well as a response time faster than the minimum available acquisition time of the microspectrometer (1ms).

Finally the dependence of the relative losses and the pumping power is studied. Figure 4b) shows this linear dependence with a slope of 0.17 dB/mW.
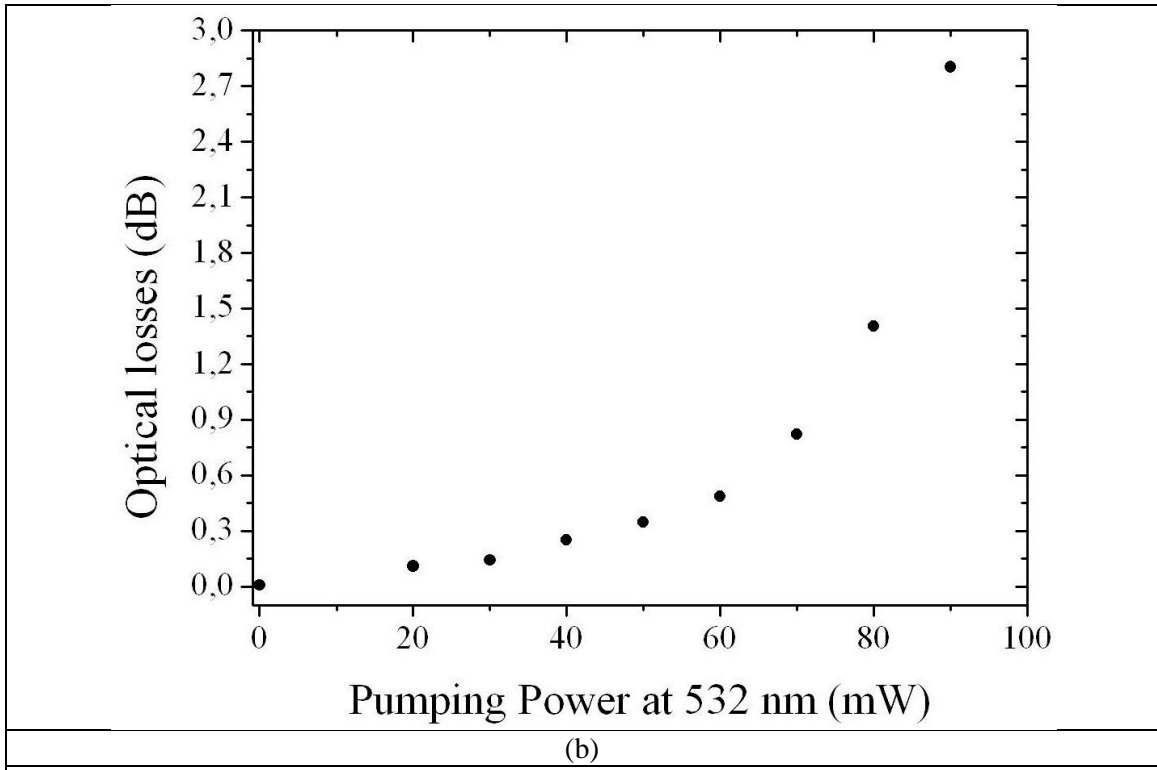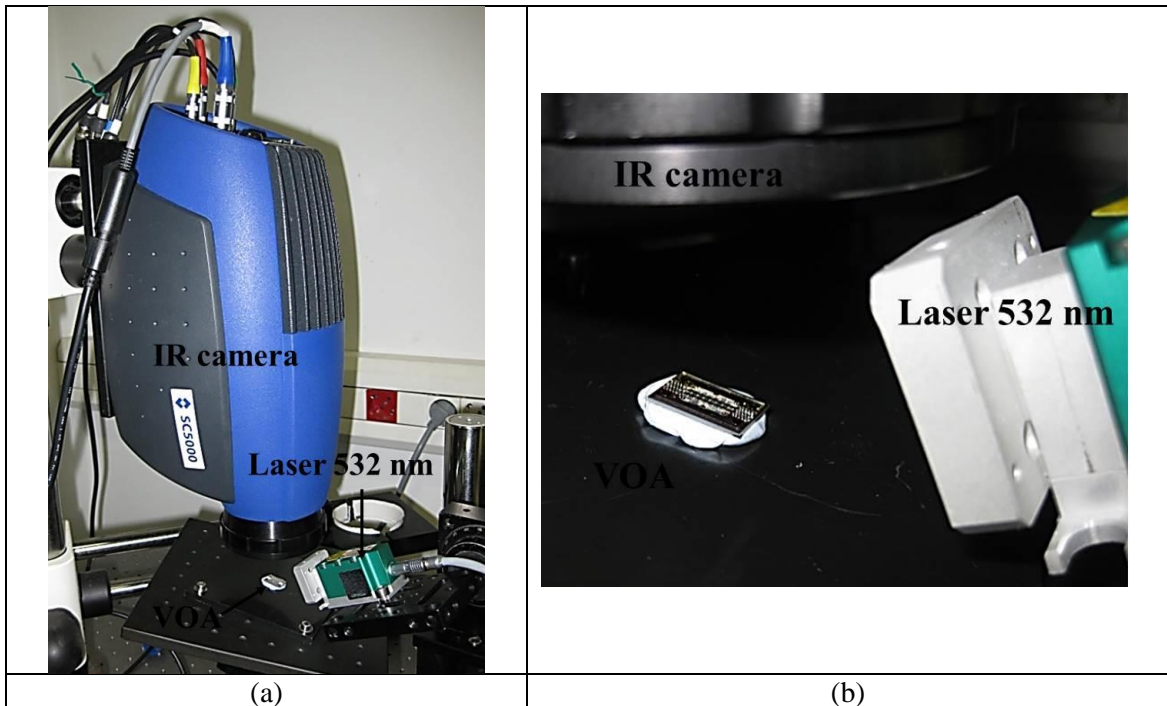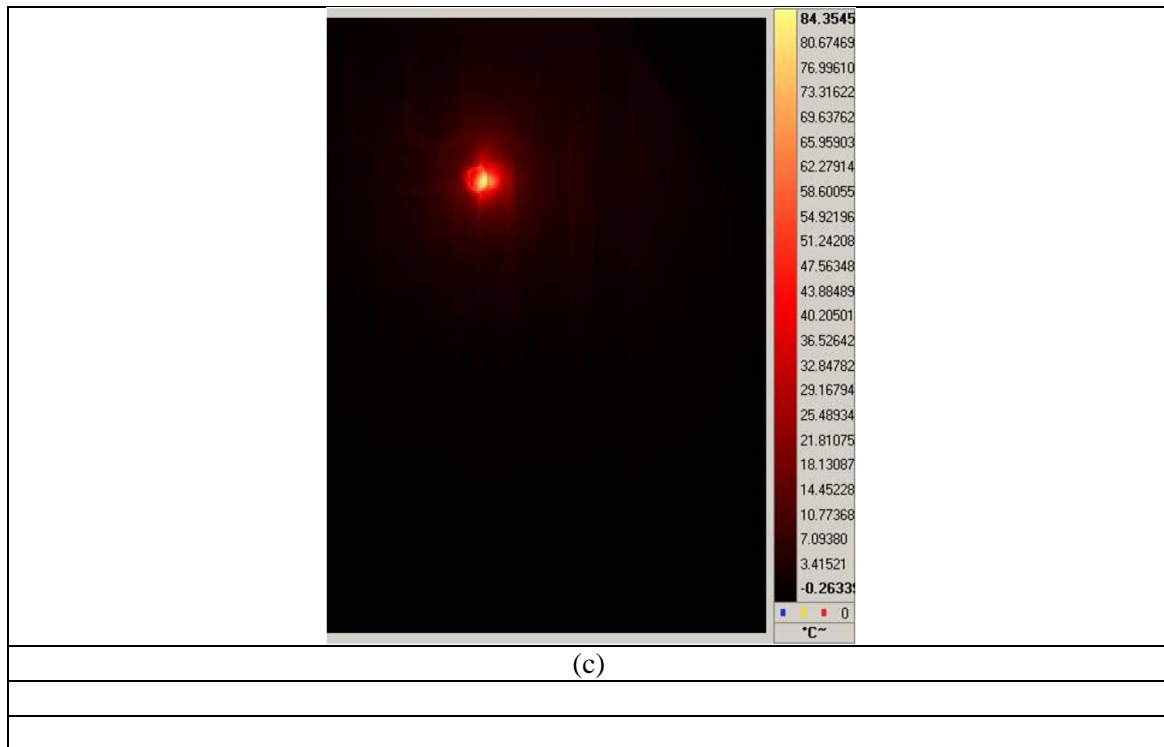

(a)

(b)
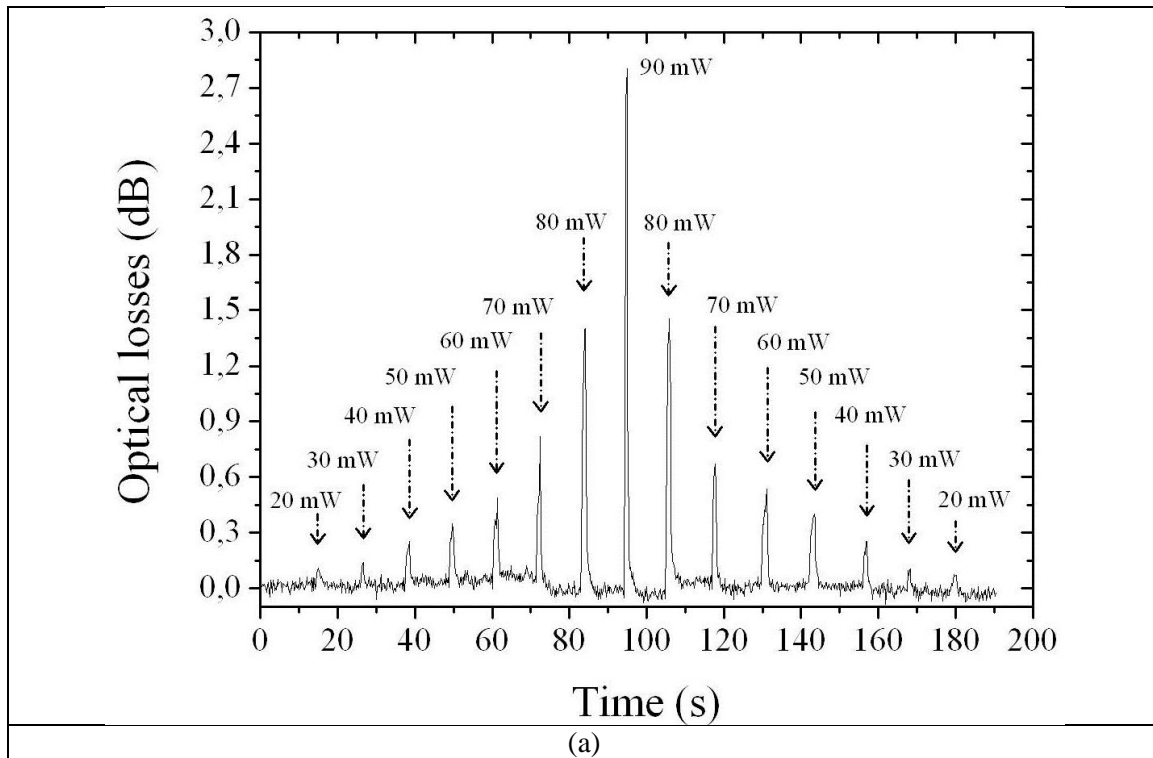
Figure 4: (a) Optical losses for MOEM VOA as a function of the time when the pumping light power (at λ = 532 nm) was focused at the actuation point for different pumping power. (b) Optical losses as a function of the pumping light power.

Thermal Characterization:

| (a) | (b) |

(c)

$$\Delta T_1 = 84\ \text{°C};\ \Delta T_2 = 114\ \text{°C};\ \Delta T_3 = 105\ \text{°C};\ \Delta T_4 = 33\ \text{°C}$$

$$\langle \Delta T \rangle = 84\text{°C}$$

$$\sigma_{\Delta T} = 18.12$$

$$\Delta T = (84 \pm 18)\ \text{°C}$$

References

[1]   M. E. Motamedi, *MOEMS: Micro-Opto-Electro-Mechanical Systems (SPIE Press Monograph Vol. PM126)*. SPIE Publications, 2005, p. 636.

[2]   A. Llobera, V. Seidemann, J. A. Plaza, V. J. Cadarso, and S. Buttgenbach, "SU-8 Optical Accelerometers," *J. Microelectromechanical Syst.*, vol. 16, no. 1, pp. 111–121, Feb. 2007.

[3]   S. J. Lee and D.-W. Cho, "Development of a micro-opto-mechanical accelerometer based on intensity modulation," *Microsyst. Technol.*, vol. 10, no. 2, pp. 147–154, Jan. 2004.

[4]   C. Marxer, C. Thio, M.-A. Gretillat, N. F. de Rooij, R. Battig, O. Anthamatten, B. Valk, and P. Vogel, "Vertical mirrors fabricated by deep reactive ion etching for fiber-optic switching applications," *J. Microelectromechanical Syst.*, vol. 6, no. 3, pp. 277–285, 1997.

[5]   C. Marxer, P. Griss, and N. F. de Rooij, "A variable optical attenuator based on silicon micromechanics," *IEEE Photonics Technol. Lett.*, vol. 11, no. 2, pp. 233–235, Feb. 1999.

[6]   K. H. Koh, C. Lee, and T. Kobayashi, "A Piezoelectric-Driven Three-Dimensional MEMS VOA Using Attenuation Mechanism With Combination of Rotational and Translational Effects," *J. Microelectromechanical Syst.*, vol. 19, no. 6, pp. 1370–1379, Dec. 2010.

[7]   A. Llobera, G. Villanueva, V. J. Cadarso, S. Battgenbach, and J. A. Plaza, "Polymeric MOEMS Variable Optical Attenuator," *IEEE Photonics Technol. Lett.*, vol. 18, no. 22, pp. 2425–2427, Nov. 2006.

[8]   M. W. Urban, D. Roy, J. N. Cambre, and B. S. Sumerlin, "Future perspectives and recent advances in stimuli-responsive materials," *Prog. Polym. Sci.*, vol. 35, no. 1, pp. 278–301, 2010.

[9]   S. Dai, P. Ravi, and K. C. Tam, "Thermo- and photo-responsive polymeric systems," *Soft Matter*, vol. 5, no. 13, pp. 2513–2533, Jun. 2009.

[10]   H. Meng, "A Brief Review of Stimulus-active Polymers Responsive to Thermal, Light, Magnetic, Electric, and Water/Solvent Stimuli," *J. Intell. Mater. Syst. Struct.*, vol. 21, no. 9, pp. 859–885, May 2010.

[11]   J. Vila-Planas, E. Fernández-Rosas, B. Ibarlucea, S. Demming, C. Nogués, J. A. Plaza, C. Domínguez, S. Büttgenbach, and A. Llobera, "Cell analysis using a multiple internal reflection photonic lab-on-a-chip.," *Nat. Protoc.*, vol. 6, no. 10, pp. 1642–55, Oct. 2011.

* future perspectives and recent asvances in stimuli-responsive materials

** a brief review of stimulus-active polymers responsive to thermal, light, magnetic electric, and water/solvent stimuli

*** thermo and photo responsive polymeric systems

4. Conclusions

In this thesis two new stimulus-sensitive materials (SSM) have been developed for its further implementation in micro-opto-electro-mechanical systems (MOEMS). Firstly, a magnetically-actuated SSM (M-SSM) composed by PDMS and FF (in different wt%) has been studied and applied to a magnetic variable optical attenuator (VOA). Secondly, a light-actuated SSM (L-SSM) based on SU-8 and color dyes has been characterized and implemented in a light actuated VOA.

Related to M-SSM, six samples with different concentration of ferrofluid (FF) based on Fe_3O_4 nanoparticles ($S_0=0$, $S_1=4.6$, $S_2=6.5$, $S_3=14.9$, $S_4=22.8$, $S_5=29.9$ and $S_6=35.8$ in wt% FF) into the PDMS matrix have been obtained.

The polymerization time for non-doped PDMS has been around 20 minutes at 80ºC. Even with the addition of FF, samples S_0 to S_3 have the same polymerization time, indicating that the addition of the doping agent did not affect the cross-linking time. For samples S_4 and S_5 the polymerization has been reached at 25 minutes and for S_6 up to 35 minutes. Such increase of time is already significant and variations on the polymer structural properties are hypothesized.

From a material point of view, the M-SSM, samples S_2 and S_6 have been studied by TEM. A homogenous distribution of the Fe_3O_4 nanoparticles even for the highest concentration of FF has been observed. Moreover, the particle size distribution confirms no aggregates in the M-SSM with a particle size (D_{TEM}) of 8 nm ± 4 nm. T

The magnetization as a function of the applied magnetic field for samples S_1 to S_6 has not shown either coercivity or remanence at room temperature indicating a typical superparamagnetic behavior of M-SSM, as expected.

4. Conclusions

Moreover, from the magnetic study the magnetic particle average size has been also calculated obtaining values (D_L) which are smaller than D_{TEM}. We realize that the magnetic measurements do not take into account the presence of the surfactant layer at the surface of the MNPs. For this reason the particle size has been recalculated including the thickness of a unit cell (D'_L). Thereby, it can be confirmed that no aggregates has been formed in the M-SSM, even with the samples with the highest FF concentration. Thus, it is expected a homogeneous response to an external magnetic stimuli.

The Young's modulus (Y_{M-SSM}) of the M-SSM has been studied both experimental and theoretical, showing a similar tendency with the FF concentration; except for an abrupt experimentally decrease close to 30% for a concentration of 35.8 wt% FF. This can be associated to the incomplete polymerization due to incomplete polymerization.

Optically, the transmittance as a function of the FF concentration has been studied. The effect of the FF concentration on the M-SSM has been shown on the spectral response of the M-SSM which varies from 50 % of transmittance (for S_1 and S_2) to a value of 73 % (for S_3 to S_6). A possibility to take advantage of such optically property has been the development of MOEMS: i) in which the M-SSM can be implemented obtaining a magnetically-actuable system which are sensitive to external magnetic stimulus and ii) for maintaining the transmittance properties the use of a non-doped PDMS.

The cell viability of the M-SSM has been studied in order to determine whether if the inclusion of FF on the PDMS matrix causes PDMS to become toxic. For samples from S_0 to S_5 a low toxicity has been obtained (considering volumes a_1, a_2 and a_3). In contrast, for samples corresponding to the highest FF concentration (S_6) and for the volume a_3, the toxicity drastically increased as compared to the rest of the samples. Thus, M-SSM presents low toxicity.

Thus, the M-SSM presented in this work keeps the elastomeric mechanical properties of the polymer while providing a magnetic functionality by simply varying the FF concentration. Moreover, the presented M-SSM has been implemented on

magnetic MOEMS-VOA by using two different techniques: soft lithography (SLT) and ink-jet printing (IJP) obtaining what has been called VOA_{SLT} and VOA_{IJP}.

Both configurations have a common geometry consisting on a waveguide-cantilever and two alignment channels for positioning both the input and the output fiber optics. For SLT, different weight fractions of FF (14.9 wt %, 22.8 wt % and 29.9 wt %) have been incorporated into the PDMS obtaining the M-SSM. It has been used for defining magnetic stripes on the bottom side of the waveguide-cantilever included in the VOA_{SLT}. By using IJP, a total amount of FF corresponding to 14.8 wt %, 20.4 wt % and 22.3 wt % of FF has been entrapped between two non-doped PDMS layers at the waveguide-cantilever tip (outside the optical path), resulting in the VOA_{IJP}.

In both strategies, deflection increases with B_{app} until a quasi-saturation regime is reached (0.29-0.57 kG). When comparing VOAs with similar wt % of FF, larger deflections and higher actuation losses are always obtained for VOA_{IJP} than for VOA_{SLT}. Furthermore, without actuation, the intrinsic optical losses (i.e. the losses due to the imperfections of the material or geometries of the device indicating the guiding quality of the optical system) have been measured to be between 9.0±0.1 dB and 9.8 ± 0.1 dB for the VOA_{SLT} and, whereas for the VOA_{IJP} these values are between 5.1 ± 0.1 dB and 5.4 ± 0.1 dB. Comparing both technologies, the IJP has been demonstrated to be a valid technique for improving the performance, not only with the VOAs here presented, but in general for MOEMS (or even MEMS) using M-SSMs.

Secondly, two different photoresist (Epocore and SU-8) have been used in combination with non-polar dyes obtaining $L\text{-}SSM_{Epo}$ (lilac, red and yellow) and $L\text{-}SSM_{SU-8}$ (lilac, red, yellow, orange, blue and green). While the resolution decreases (with a minimum resolution of 7μm) with the dose, the structurability of the $L\text{-}SSM_{Epo}$ remains unaltered when compared to the non-doped case. Moreover, no dye bleaching is observed.

The spectral response of both L-SSMs reveals a theoretical behavior which is expectable in absorbance filters (allowing to block specific wavelengths), as opposite to the more common cases in absorbance filters, where either high-passband or low-passband filters are obtained. Comparing transmittance values (for an optical path length of 1500 μm and 50 mg of red dye-doped) for both L-SSMs and according to the

4. Conclusions

available tools in the laboratory the red dye L-SSMSU-8has been chosen to its implementation in a micro-opto-electro-mechanical system variable optical attenuator (VOA-MOEMS). These systems have been designed and fabricated for its further characterization. Mechanically, the proposed VOA-MOEMS consists of four mechanical beams that clamp the seismic mass to the frame, preventing angular misalignment. Optically, three waveguides are defined at the mechanical structure, whereas fish-bone elements align and clamp the input and output fiber optics in the same optical axis as the waveguide. Actuation is achieved by defining four actuation points on each VOA-MOEMS which are anchored at the mechanical beams close to the frame. These actuation points consist on structured red dye $L-SSM_{SU-8}$. In such elements a driving wavelength of 532 nm is absorbed resulting in a thermal expansion of the L-SSM, leading to a displacement of the seismic mass. In turn, this causes a misalignment between the waveguide and the fiber optics. Thus, in the proposed VOA-MOEMS, the actuation losses are modulated as a function of the actuation principle. From the thermal characterization an increase of the temperature of the red $L-SSM_{SU-8}$ when the green light is actuating on such regions is observed. Optical simulations predict a displacement of the waveguides in function of the external actuation. Moreover, experimental results show a response time, i.e. the rise time (1.7 s) and fall time (3.5 s), is 5.2 s. This may be due to a degradation of the material caused by a possible bleaching effect on the $L-SSM_{SU-8}$ located at the actuation point. An excellent reversibility and repeatability as a function of the actuation power, reaching values close to 3dB for 90 mW has been observed.

5. Appendixes

Appendixes include a glossary of acronyms

a_0: thickness of a unit cell

AFM: atomic force microscopy

AR: attenuation range

B_{app}: magnetic field applied

cm: centimeter

ºC: Celsius temperature scale

C: volume fraction of the fillers in the PDMS

CNM: Centro Nacional de Microelectrónica

CSIC: Centro superior de Investigaciones Científicas

CTE: coefficient of thermal expansion

coth: hyperbolic tangent

Cu: coppper

Δx: lateral misalignment

Δy: variation of the deflection

ΔT: variation of temperature corresponds

dB: decibels

DC: direct current

DIW: deionized water

D_L: magnetic particle size

5. Appendixes

D'$_L$: particle size considering both the magnetic particle size (D$_L$) and the unit cell correction

DRIE: Deep Reactive Ion Etching

D$_{TEM}$: TEM image analysis the nanoparticle size distribution obtained from Gaussian fitting

EMIs: electromagnetic interferences

emu: electromagnetic units

FF: ferrofluid

G: Gauss

g: gravity acceleration / gravitational field (9.8 m/s^2)

Gpa: giga pascals

h: hour

h: height

h: thickness

H: magnetic field

HB: hard bake

i.e.: means

IJP: inkjet printing technique

IL: insertion loss

IMB: Instituto Microelectrónica Barcelona

IR: infrared

K: kelvin

k$_B$: Boltzmann constan

kHz: kilohertz

kG: kiloGauss

kPa: kiloPascal

λ: wavelength

l: length

LED: light emitting diode

L-SSM: light SSM

L-SSM$_{Epo}$: light sensitive stimuli material based on Epocore

L-SSM$_{SU-8}$: light sensitive stimuli material based on SU-8

μ: true magnetic moment

μm: micromilimiter

μT: microtesla

M: molar

MB: methylene blue

MEMS: micro-electromechanical systems

mg: miligrams

mJ: milijoules

ml: mililiter

mm: milimeter

MNPs: magnetic nanoparticles

MOEMS: micro-opto-electromechanical systems

M-SSM: magnetic sensitive stimuli material

ms: milisecond

m$_s$: saturation magnetization

mT: militesla

mW: miliwatt

NEMS: nano- -electro-mechanical systems

n$_{FF}$: real part of the refractive index of the ferrofluid

NIR: near infrared

nm: nanomilimiter

π: number pi

PANI-EB: polyaniline emeraldine

5. Appendixes

PDL: polarization dependence loss

PDMS: Polydimethylsiloxane

PEB: post exposure bake

pL: pico liter

PLC: planar lightwave circuits

PMMA: Poly(Methyl Methacrylate)

ppm: parts per milion

Q*: quality factor

ρ: density

PS: polystytrene,

RI: refractive index

RS: response speed

s: seconds

SB: soft baked

SB: spectral bandwidth

SEM: scanning electron microscope

Si: silicon

SLT: soft lithography

SNR: higher signal-to-noise ratio

SSMs: sensitive stimuli materials

T: is the absolute temperature

T': the temperature after applying the the actuation

T: transmittance

TEM: transmission electron microscopy

TIR: Total Internal Reflection

V: volts

VCSELS: vertical-cavity surface emitting lasers

VSM: vibrating sample magnetometer

VSMC: vascular smooth muscle cells

VOAs: variable optical attenuators

VOA$_{SLT}$: variable optical attenuator defined using soft lithography technique

VOA$_{IJP}$: variable optical attenuator defined using inkjet printing technique

v:v: volume:volume

ω: resonant frequency

w: width

W: watts

WDM: wavelength division multiplexing

WSSs: wavelength-selective switches

wt%: weight per cent

Y: Young's modulus

y$_{max}$: maximum cantilever deflection under the action of the gravitational field

Y$_{M-SSM}$: Young's modulus of the M-SSM